Spectroscopy and manipulation of positronium in excited states

Alberto M. Alonso

A dissertation submitted in partial fulfillment

of the requirements for the degree of

Doctor of Philosophy

of

University College London.

Department of Physics and Astronomy

University College London

2018

I, Alberto M. Alonso, confirm that the work presented in this thesis is my own. Where information has been derived from other sources, I confirm that this has been indicated in the work.

Acknowledgements

First and foremost I would like to thank my supervisor David Cassidy for his unwavering support and relentlessly efficient work ethics. I have been able to learn much from him, and the importance he has had on my education cannot be overstated. I would also like to thank Stephen Hogan for his continued collaboration with our group in general, and with me in particular. I have had the opportunity to continuously learn from him throughout the course of this project, and for this I am grateful.

I would also like to thank the other members of our group, past and present: Ben Cooper, Lokesh Gurung, Benedict Sukra, and Thomas Wall, with a special mention to Adam Deller who also took much of his time to train me in various necessary aspects of laboratory work. Thank you to John Dumper and Rafid Jawad for their technical assistance regarding the mechanical and electronic workshop. To all my office workmates that made our working environment lively yet efficient: Andrea Loreti, Rina Kadokura, Simon Brawley, and the rest of the students from the positron group at UCL, thank you for an amazing time.

Last, but certainly not least; I would like to thank my family and loved ones, beginning with my late father Andrés, who believed in me until his very last moments, my sister Dulce, who has always been a balancing force in my life, and my mom Ángeles, whose love and patience for me have no observable bounds. She is my biggest role model, and the single most influential person in my life. Finally, I would like to thank Hannah Ross for her tremendous support and companionship during all these years, she is a pillar of inspiration and I am lucky to consider her my best friend and partner.

Abstract

A Surko-type positron trap has been used to produce intense positron pulses, and thus a dilute positronium (Ps) gas in vacuum with an initial density of 10^7 cm^{-3}. This gas was excited with lasers for a variety of experiments. $n = 2$ atoms were prepared using a single-photon excitation scheme ($1\,^3\mathrm{S} \rightarrow 2\,^3\mathrm{P}$) in controlled electric and magnetic fields for studies of Stark and Zeeman effects, measurements of Ps cooling via Doppler spectroscopy, and for the produciton of ensembles of atoms in pure $2\,^3\mathrm{S}_1$ states. The first measurements of Ps excitation to specific Rydberg-Stark states were performed via a two-color two-photon excitation scheme ($1\,^3\mathrm{S} \rightarrow 2\,^3\mathrm{P} \rightarrow n\,^3\mathrm{S}/n\,^3\mathrm{D}$). Ps atoms in low-field–seeking Rydberg Stark states were prepared at the entrance of an electrostatic quadrupole guide which was used to control the trajectories and velocity distributions of the Ps atoms. These advances, together with the results from numerical simulations, suggest that these methods could be used in to perform Stark deceleration and trapping of Rydberg Ps, high-precision Ps spectroscopy, and to create positron-atom bound states.

Contents

Chapter 1

Introduction

1.1 Motivation

In this thesis I describe recent advances in the fields of positronium (Ps) laser spectroscopy and the manipulation of excited Ps atoms by inhomogeneous electric fields. Experiments were performed using an intense pulsed positron beam (typically $\sim 10^6$ particles in a 3 ns pulse) generated with a Surko-type buffer gas trap [Danielson *et al.* 2015]. This beam was implanted into porous silica targets [Liszkay *et al.* 2008] which generate a thermal Ps "gas" in vacuum that can be probed with pulsed laser systems ($\sim$ 6 ns). Standard pulsed dye lasers can generate beam intensities on the order MW/cm^2, which enables efficient Ps excitation, generally limited only by the spectral overlap of the laser light and the Doppler broadened optical transition; our experiments all begin by driving $1S-2P$ transitions using UV light (243 nm), and in some cases a second IR laser (750 nm) is also used to produce highly excited Rydberg states, including selected Rydberg-Stark states [Wall *et al.* 2015, Deller *et al.* 2016b]. Stark states with positive energy shifts have large electric dipole moments and experience forces towards electric field minima. We have made use of these properties to manipulate atoms with inhomogeneous electric fields [Deller *et al.* 2016a, Alonso *et al.* 2017a], resulting in radial confinement in an electrostatic quadrupole guide.

This technique and other forms of atom optics, such as deceleration and trapping [Lancuba & Hogan 2014, Hogan *et al.* 2013], may make it possible

to perform a Rydberg Ps free-fall measurement [Mills & Leventhal 2002] to test for anomalous gravitational interactions of systems containing antimatter [Goldman & Nieto 1982]. However, because stray electric fields can never be completely eliminated, free-fall experiments performed using Rydberg atoms require Stark states that are not sensitive to electric fields (i.e., states with no dipole moment), which is incompatible with Stark manipulation methods. An alternative approach to performing a gravity measurement of Ps could be to use metastable 2^3S_1 states [Alonso *et al.* 2017b, Alonso *et al.* 2016b, Alonso *et al.* 2015], for interferometry measurements [Oberthaler 2002, Sala *et al.* 2015], which may be sensitive enough to measure gravitational effects [Biedermann *et al.* 2015].

The availability of a slow and focussed Ps beam would enable improved precision in Ps spectroscopy. A sufficiently precise measurement of the Rydberg constant (R_∞) using Ps could eventually contribute towards the "proton radius puzzle" [Pohl *et al.* 2010, Pohl *et al.* 2013]. This is a discrepancy in the proton radius as measured in precision hydrogen spectroscopy and in experiments using muonic hydrogen [Mohr *et al.* 2016]. The origin of this discrepancy remains unexplained; some new measurements of the 2s-4p transition frequency in hydrogen that take into account quantum interference phenomena have been performed. These measurements find a smaller value for the Rydberg constant than previous experiments [Beyer *et al.* 2017], and agree with the muonic hydrogem measurements. This indicates that inaccuracies in our knowledge of R_∞ could be the root cause of the discrepancy. The situation is not resolved by one single new measurement, and new data are warranted. It would be valuable therefore to measure this constant also in Ps, since it does not contain any proton related complications.

1.2 Antimatter and discovery of positronium

Antimatter has been a subject of theoretical and experimental study for over 80 years since its existence in the form of the positron was predicted by Dirac [Dirac 1927, Dirac 1928a, Dirac 1928b, Dirac 1931], and subsequently confirmed by Anderson in cloud chamber experiments [Anderson 1933]. Shortly after this discovery,

it was postulated by Wheeler [Wheeler 1946] (and earlier also by Mohorovičić [Mohorovičić 1934], but with a much less rigorous mathematical treatment) that it should be possible for a positron and an electron to form a bound metastable system which would have similar properties to that of hydrogen, i.e, a negative charge orbiting a positive charge, but with a correspondingly small reduced mass. Mohorovičić named this new element *electrum*, although today it is more commonly known as *positronium* [Ruark 1945].

Positronium can be described by the Bohr model as a hydrogenic system with a reduced mass of approximately half that of hydrogen ($\mu_{\mathrm{Ps}} \simeq \mu_{\mathrm{H}}/1.9989$), meaning that, compared to hydrogen, the Bohr radius for Ps is twice as large, its Rydberg constant is reduced by a factor of $\sim$2, and the gross energy levels quantified by the principal quantum number n are separated by half the energy compared to hydrogen, i.e., the binding energy of Ps is 6.8 eV instead of 13.6 eV.

However, there are many more differences and interesting properties that distinguish Ps from hydrogen other than a factor of two. For example, the spin-orbit coupling "fine structure" corrections and the spin-spin interactions (sometimes incorrectly labeled as "hyper-fine") have similar magnitudes, thus rendering the distinction between the terms *fine* and *hyper-fine* somewhat meaningless when referring to Ps.

Perhaps the most notable difference between Ps and any other conventional atom is its self-annihilating nature. Being composed of a particle-antiparticle pair, the annihilation probability is proportional to the overlap of the electron and positron wavefunctions [Dirac 1930], such an overlap is non-zero for S ($\ell = 0$) states (although this overlap scales as n^{-3} [Ore & Powell 1949, Dirac 1930]), this leads to the singlet ($1\,^1\mathrm{S}_0$) and triplet ($1\,^3\mathrm{S}_1$) ground states of Ps (often referred to as p-Ps and o-Ps) having lifetimes of 125 ps and 142 ns respectively, however, for states where $\ell > 0$, the overlap is almost completely suppressed and the annihilation rate becomes much larger than the fluorescence rates, as shown in table 1.1.

Positronium was first observed by M. Deutsch in 1951 [Deutsch 1951a] in an experiment which made use of a ^{22}Na radioactive source to produce a steady stream

of positrons which then collided with various different gases to form Ps, he measured the lifetime of triplet ground state Ps and the energy difference between o-Ps and p-Ps [Deutsch 1951b, Deutsch & Brown 1952]. These measurements were in agreement with bound state QED and were the first experimental evidence for the existence of Ps.

1.3 Positronium spectroscopy, early history

The field of atomic physics saw great change after the invention of the laser in 1960 [Maiman 1960], enabling the measurement of atomic lines with precision [Hänsch *et al.* 1971]. However, even though Ps was created in a controlled lab environment some years before the advent of the laser, it did not take part in this initial revolution, instead it was not until 1982 that Ps laser spectroscopy was made plausible in a comparable way to regular atoms [Chu & Mills 1982]. The main limitations that held back the initial Ps experiments were to do with the DC positron beams that were used at the time which did not have large enough intensities [Canter *et al.* 1972] to perform optical spectroscopy experiments efficiently with continuous wave (CW) lasers.

Another major complication when it comes to performing spectroscopy with Ps is its remarkably short self-annihilation lifetimes. For the triplet ground state the annihilation lifetime is 142 ns if unperturbed, it is therefore not possible to store Ps atoms for a long period of time and build up a "Ps reservoir" with which experiments may be performed. This is a major disadvantage since many spectroscopic experiments depend on readily available dense atomic gases. Since ground state Ps could only be stored for up to 142 ns, then the most efficient way to spectroscopically study it is to produce it in a pulsed fashion and address it with a high power pulsed laser as soon as it is produced, before any significant portion of it self-annihilates. It is possible to design an experiment where a CW laser is used for laser excitation of Ps [Fee *et al.* 1993], however, such arrangements tend to have very low count rates, they are contingent on not needing to change laser wavelength by a large amount, and usually need major modifications if a different measurement

is to be taken.

The first experiments that succeed in photoexciting Ps used pulsed positron beams and took place between 1982 and 1992. An experiment performed by S. Chu and A. P. Mills [Chu & Mills 1982], and made use of a ^{58}Co β^+ radioactive source and a magnetic bottle buncher to produce small positron pulses containing $\sim$ 20 positrons in 10 ns FWHM pulses, which were implanted in a solid Cu(111) target to produce approximately 4 Ps atoms per pulse that could then be addressed by the laser pulses. Regardless of the extremely low count rate, this experiment yielded a measurement of the $1\,^3S_1 \rightarrow 2\,^3S_1$ two-photon Doppler-free transition linewidth agreeing with theory to within 0.5 GHz. This same experiment was improved upon in 1984, using an Al(111) solid target and a slightly more intense positron beam ($\sim$ 80 positrons per pulse) to yield an extremely precise measurement (to within 12 ppb) of the $1\,^3S_1 \rightarrow 2\,^3S_1$ transition interval which agreed to within 1 % with QED predictions [Chu *et al.* 1984].

A similar experiment was then performed making use of a pulsed positron beam generated from an accelerator, and a CW laser [Fee *et al.* 1993], which managed to increase the precision of the measurement by approximately a factor of 3. The only other example of Ps laser spectroscopy up until 2010 was done by K. P. Ziock et.al. [Ziock *et al.* 1990a, Ziock *et al.* 1990b]. They made use of an intense positron pulse (approximately 10^5 positrons per 15 ns pulse) generated from the linear accelerator at the Lawrence Livermore National Laboratory; at the time, this was the most intense positron beam in the world [Howell *et al.* 1982, Howell *et al.* 1985]. They used pulsed lasers to excite Ps to high Rydberg states with a principal quantum number n between 13 and 15. However, after both of these experiments concluded, the field of Ps spectroscopy did not advance at all for $\sim$17 years. This was partly because in order to perform some of these experiments, accelerators were needed, which are not common enough to drive such experiments into the laser physics mainstream, and even though appropriate radioactive sources were relatively easy to obtain (compared to accelerators), they offered extremely low count rates, and the experiments that made use of them

were notoriously difficult to perform.

It was not until C. M. Surko and co-workers designed a Penning buffer gas trap with an asymmetric electric potential structure (commonly known as a Surko trap) that it was feasible to consider building a University-scale Ps laser spectroscopy lab without the need for accelerators [Surko *et al.* 1989, Murphy & Surko 1992, Danielson *et al.* 2015].

The use of Surko traps enabled new Ps spectroscopic measurements that did not require large-scale facilities or relied on low count-rates, bringing Ps spectroscopy much closer to the level that the rest of the atomic laser spectroscopy community had been at for decades. Even though these new positron trapping techniques meant that $\sim$ 5 ns pulses of over 10^6 positrons could be produced without the need for an accelerator, the amount of Ps atoms created was still not enough to perform efficient absorption or emission spectroscopy, since the Ps atoms are typically produced with large energy spreads, and in comparatively low numbers. However it is worth noting that the first observation of $n = 2$ Ps was indeed performed [Canter *et al.* 1975] by measuring the emitted photons from the excited state to the ground state, but modern detection techniques [Cassidy *et al.* 2006b] that detect the gamma rays produced after Ps annihilates are far more efficient and are the norm today. Gamma ray photons are easy to detect, and in each Ps pulse containing up to 10^5 Ps atoms, it is possible to measure of the order of 10^4 photons, meaning that experiments can be performed with much better signal to noise ratios.

Before 2006, Ps spectroscopy experiments were usually performed by counting a single gamma ray photon per positron pulse, it was not until a new detection scheme was devised [Cassidy *et al.* 2006b] that it was possible to extract more accurate information from single positron pulses recording a full waveform from a scintillator material into a fast oscilloscope due to a short positron pulse being implanted into a solid Ps production target. This means that all events caused by the positron pulse (accounting for solid angle and detection efficiency) can contribute towards the timing spectrum being measured, as opposed to just one (as it is the case with Positron annihilation lifetime spectroscopy (PALS) techniques),

thus vastly decreasing the amount of acquisition time needed for each spectrum [Cassidy *et al.* 2006b].

Positron trapping techniques were combined with the newest detection methods in a series of experiments in UCR (University of California Riverside) by D. B. Cassidy, A. P. Mills and co-workers, where the first optical spectroscopy measurements of Ps in 17 years were performed. These include, amongst many others; the first measurement of the Ps $1^3S_1 \rightarrow 2^3P_J$ transition lineshape [Cassidy *et al.* 2010a], narrowing and cavity shift effects [Cassidy *et al.* 2011b], new measurements of the energy difference between the Ps singlet (1^1S_0) and triplet (1^3S_1) ground state [Cassidy *et al.* 2012c], many advances towards the formation of a Ps BEC, such as demonstrating interactions between Ps atoms in porous targets [Cassidy & Mills 2011], production of a fully spin-polarized Ps ensemble [Cassidy *et al.* 2010b], the remarkable production of the Ps molecule (Ps_2) [Cassidy & Mills 2007] and optical spectroscopy of its first excited state [Cassidy *et al.* 2012b], and finally, measurements of Ps excited to a high Rydberg state [Cassidy *et al.* 2012a, Jones *et al.* 2014] with greatly improved signal to noise ratios compared to the measurements made by K. P. Ziock *et. al* [Ziock *et al.* 1990b].

1.4 Properties of positronium

Positronium can be described in simple terms as a hydrogenic system. Since it is composed of only two oppositely charged particles bound by the Coulomb interaction, its energy levels can be described by [Foot 2005]

$$E_n = \frac{-\alpha^2 \mu_{\mathrm{Ps}} c^2}{2n^2} = \frac{-\alpha^2 m_e c^2}{4n^2} \simeq \frac{-6.8\ \mathrm{eV}}{n^2}, \tag{1.1}$$

where n represents the principal quantum number, c is the speed of light in vacuum, α is the fine structure constant, μ_{Ps} is the reduced mass for Ps, and m_e is the mass of the electron. The fundamental difference between hydrogen and positronium is that the reduced mass is approximately half compared to hydrogen (i.e., $\mu_{Ps} = m_e/2$, $\mu_H \simeq 0.9995 m_e$) and therefore the gross energy levels that yield from equation 1.1

Level	$\tau_{\text{ann.}}$(ns)	Ref.	$\tau_{\text{fl.}}$(ns)	Ref.
$1\,^1S_0$	0.125	[Dirac 1930]	N/A	N/A
$1\,^3S_1$	142	[Ore & Powell 1949]	$\gtrsim 10^{16}$	[Wallyn *et al.* 1996]
$2\,^1S_0$	1	[Dirac 1930]	$\simeq$243 100 000	[Shapiro & Breit 1959]
$2\,^3P_0$	100 000	[Alekseev 1958]	3.19	[Bethe & Salpeter 1957]
$2\,^3P_1$	$\simeq\infty$	[Alekseev 1958]	3.19	[Bethe & Salpeter 1957]
$2\,^1P_1$	3 330 000	[Alekseev 1959]	3.19	[Bethe & Salpeter 1957]
$2\,^3P_2$	384 000	[Alekseev 1958]	3.19	[Bethe & Salpeter 1957]
$2\,^3S_1$	1 136	[Ore & Powell 1949]	$\simeq$243 100 000	[Shapiro & Breit 1959]

Table 1.1: Annihilation ($\tau_{\text{ann.}}$) and fluorescence ($\tau_{\text{fl.}}$) lifetimes for the $n=1$ and $n=2$ Ps. From [Alonso *et al.* 2016b].

are approximately scaled by a factor of $1/2$ accordingly.

However, the fine (and so-called hyperfine) structure of Ps is remarkably different from that of hydrogen. Positronium atoms are subject to virtual annihilation processes [Rich 1981] that result in large shifts in the energy levels, and the spin-spin interaction between the positron and the electron is far larger than the spin-spin interaction of the electron with the proton in hydrogen since the nuclear magneton is so much smaller than the Bohr magneton [Mohr *et al.* 2016]. Because of historical reasons the energy splitting between the two $n=1$ spin states of Ps ($1\,^3S_1$ and $1\,^1S_0$) has been referred to as the *hyperfine splitting* due to its analogy with the hydrogen hyperfine splitting, however this is quite misleading since this splitting arises in part due to a mechanism that is not present in hydrogen. Virtual annihilation processes coupling to the vacuum, a process unique only to Ps and other particle-antiparticle systems. However, regardless of nomenclature, the energy splitting between the two spin states in ground state Ps is much larger than it is in hydrogen ($\sim$203 GHz [Pirenne 1944] for Ps and $\sim$1.4 GHz [Hellwig *et al.* 1970] for hydrogen). The fine structure corrections up to α^4 order are given by [Ferrell 1951] with respect to the gross energy levels given by equation 1.1 as

$$\Delta E_{n,\ell,S,J} = \frac{\alpha^4 m_e c^2}{n^3}\left[\frac{11}{64n} - \frac{(1+\varepsilon_{\ell,J}/2)}{2(2\ell+1)}\right], \tag{1.2}$$

where $\varepsilon_{\ell,J} = 0$ for $S = 0$ and for $S = 1$,

$$\varepsilon_{\ell,J} = -\frac{7}{3}\delta_{\ell,0} + (1-\delta_{\ell,0}) \begin{pmatrix} \frac{-(3\ell+4)}{(\ell+1)(2\ell+3)}, & J = \ell+1 \\ \frac{1}{\ell(\ell+1)}, & J = \ell \\ \frac{(3\ell-1)}{\ell(2\ell-1)}, & J = \ell-1 \end{pmatrix}, \tag{1.3}$$

where $\delta_{\ell,0}$ is the Kronecker delta function. It is worth noting that equations 1.3 and 1.2 are re-arranged versions of the equations given in [Ferrell 1951] for added clarity. However, the equation given by Ferrell contains a mistake, in the form of a missing multiplicative factor of $\frac{7}{12}$ to the first Kronecker delta function in his expression. Without this factor, his expression fails for triplet S states ($S = 1, \ell = 0$). The version given in equation 1.3 accounts for this error. The corresponding energy level structure for the ground state and the first excites state of positronium is thus given in figure 1.1 with modern values.

The very notion of an atom decaying when it is already in the ground state may seem rather bizarre to the large majority of the atomic physics community which routinely deals with matter systems. However, once the self annihilation nature is formalized as another decay channel that leads to a ground state from which the atom cannot be recovered (i.e., the vacuum) then it may be simply combined with regular fluorescence annihilation to characterize the decay rate of a certain state. In practice, the self-annihilation channel in Ps is effectively closed once n is increased above $n = 2$ (and $\ell > 0$). This is due to the fact that this annihilation rate scales with the amount of overlap between the positron and the electron [Alekseev 1958, Alekseev 1959], and thus it is greatly reduced as the separation between the positron and the electron is increased, by increasing ℓ or n. Table 1.1 shows how the fluorescence and the self-annihilation lifetimes and illustrates how the annihilation decay rates scale as n^{-3} [Dirac 1930] and how they quickly become irrelevant even for $\ell = 1$ when compared to the fluorescence lifetimes which dominate at higher levels.

The number of gamma ray photons produced when Ps in a specific $|\ell S>$ state annihilates is [Wolfenstein & Ravenhall 1952]

$$(-1)^N = (-1)^{\ell+S}, \tag{1.4}$$

where N is the number of photons produced. This is a result of charge conjugation invariance, and it indicates that, in the ground state, triplet states must annihilate into an odd number of photons, and singlet states must annihilate into an even number. For both cases, single-photon and zero-photon radiation is forbidden by momentum and energy conservation, and the higher order channels (such as a triplet state decaying into 5 photons instead of 3, and a singlet state decaying into 4 photons instead

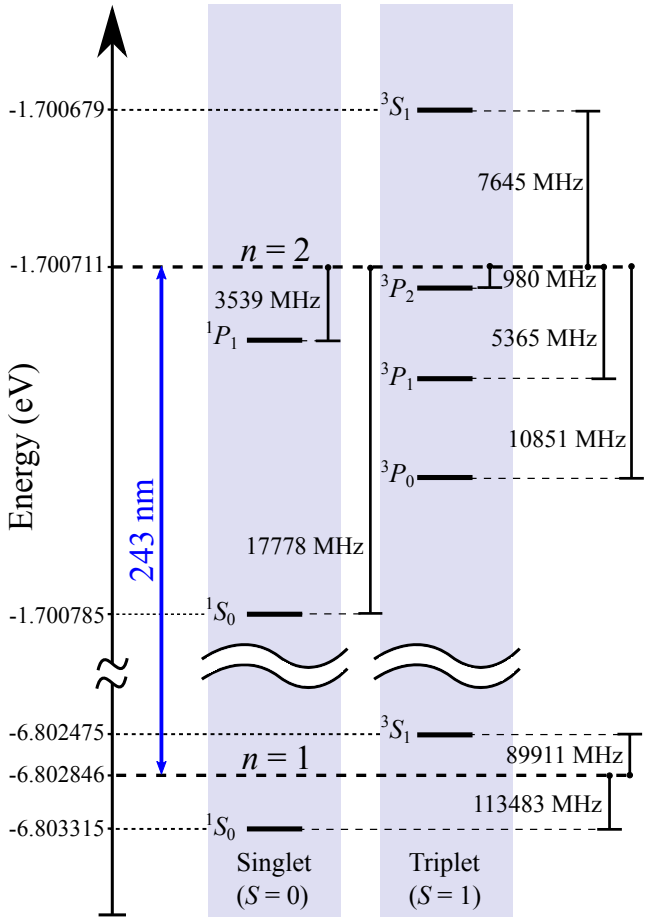

Figure 1.1: Ps energy level diagram indicating the fine structure of states with $n = 1$ and $n = 2$. The intervals between each level are denoted by their relative frequency with respect to the energies given by the Rydberg formula $E(n) = -6.8\,\mathrm{eV}/n^2$. From [Alonso *et al.* 2016b].

of 2) are heavily suppressed (at least by a factor of α, plus additional contributions due to the density of final states of photons [Ore & Powell 1949]). This means that the annihilation gamma rays from singlet states is likely to be two 511 keV photons (since $m_e c^2 = 511$ keV), however, for triplet states there can be a range of gamma ray energies since the 3 photons must add to the total rest mass energy of Ps and there are many combinations that can satisfy this and maintain momentum conservation at the same time.

Chapter 2

Apparatus and techniques

Details on the instrumentation and apparatus described in this chapter have been previously published in several articles, and as such, much of the content and figures used here were taken from these publications. Contents from Section 2.1 describing the apparatus used to produce a pulsed positron beam were published in the following articles:

- B. S. Cooper, A. M. Alonso, A. Deller, T. E. Wall, and D. B. Cassidy. *A trap-based pulsed positron beam optimised for positronium laser spectroscopy.* Rev. Sci. Instrum., **86**, 103101 (2015). doi: 10.1063/1.4931690.

- A. M. Alonso, B. S. Cooper, A. Deller, S. D. Hogan and D. B. Cassidy. *Positronium decay from $n = 2$ states in electric and magnetic fields.* Phys. Rev. A, **93**, 012506 (2016). doi: 10.1103/PhysRevA.93.012506.

While contents from Section 2.3.2 describing detection techniques and the comparison of LYSO scintillators against PWO scintillators were published in:

- A. M. Alonso, B. S. Cooper, A. Deller and D. B. Cassidy. *Single-shot positron annihilation lifetime spectroscopy with LYSO scintillators*. NIMA, **828**, 163 (2016). doi: 10.1016/j.nima.2016.05.049.

And the contents from Section 2.4 describing the counting algorithms used when making time of flight measurements were published in:

- A. Deller, A. M. Alonso, B. S. Cooper, S. D. Hogan, and D. B. Cassidy. *Measurement of Rydberg positronium fluorescence lifetimes*. Phys. Rev. A, **93**, 062513 (2016). doi: 10.1103/PhysRevA.93.062513.

2.1 Positron beamline

2.1.1 Solid neon moderator

The system described here contains a DC positron beam derived from a 1 GBq ^{22}Na source mounted behind a conical aperture [Khatri *et al.* 1990] that is thermally coupled to, but electrically isolated from, a 5 K closed cycle helium cryostat. A mono-energetic positron beam (approximately 1.5 eV spread) was achieved from the wide energy spread of the radioactive source via a process known as moderation [Canter *et al.* 1972, Cherry 1958] by freezing neon gas in front of the source [Mills & Gullikson 1986]. The positrons lose some of their kinetic energy via collisions with the solid neon, the moderator is grown by admitting neon gas directly in front of the cone via a thin tube for around 8 minutes; the pressure measured in the source chamber is $\sim 1 \times 10^{-3}$ mbar during the moderator growth. An example of a typical moderator growth sequence is shown in figure 2.1. A new moderator typically produces a DC beam of $\sim 6 \times 10^{6}$ $e^{+}s^{-1}$ from a radioactive source with an activity of $\sim 10^{9}$ $e^{+}s^{-1}$ which indicates a moderator efficiency of ~0.6%.

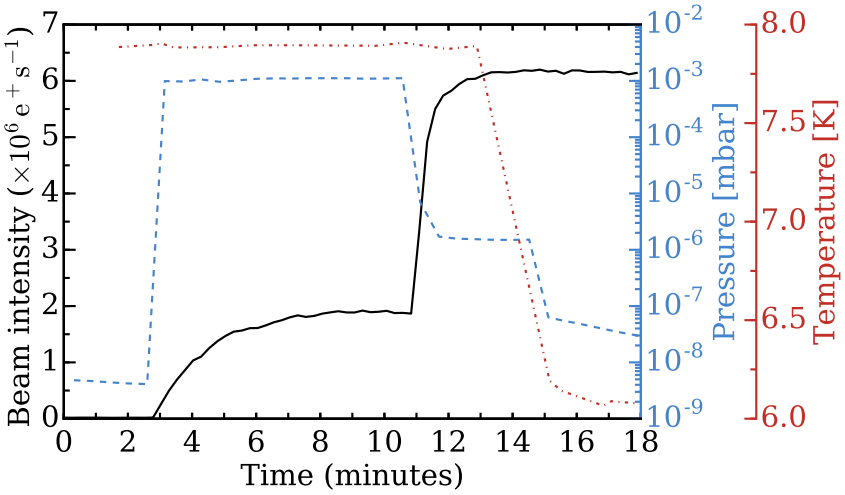

Figure 2.1: (a) A typical moderator growth sequence showing a steady increase in count rate (solid line) when the neon is introduced at a constant temperature and pressure (dots and dashes). The gas inlet is closed when the count rate levels off, causing a drop in the pressure and a corresponding increase in the count rate. The temperature (dotted line) is held above the cold head base temperature (5 K) during the growth to anneal the neon deposit.

The beam is monitored by a NaI scintillator attached to a photomultiplier tube (PMT). This is done by counting positron annihilation events that occur at the gate valve just before the next section of the beamline.

2.1.2 Buffer Gas trap

The moderated positron beam is guided to a two-stage Surko-type buffer-gas trap [Surko *et al.* 1989, Danielson *et al.* 2015] designed to capture a DC beam and emit positrons at 1 Hz. The system typically operates with a N_2 and a CF_4 mixture for positron capture and cooling [Murphy & Surko 1992, Natisin *et al.* 2014]. Positrons lose energy through inelastic collisions with N_2 molecules in the trap. This causes axial confinement within the static potential structure applied to the trap electrodes. A diagram of the beamline can be seen in figure 2.2. The potential structure and approximate pressures in the trap are shown in figure 2.3. Radial confinement is induced by the approximately flat magnetic field ($\sim$ 500 G) produced by the large solenoid surrounding the trap.

The device differs from the standard Surko arrangement [Murphy & Surko 1992] insofar as it has a larger pressure in the final stage and hence a relatively short positron lifetime. Radial compression of the trapped positrons is achieved

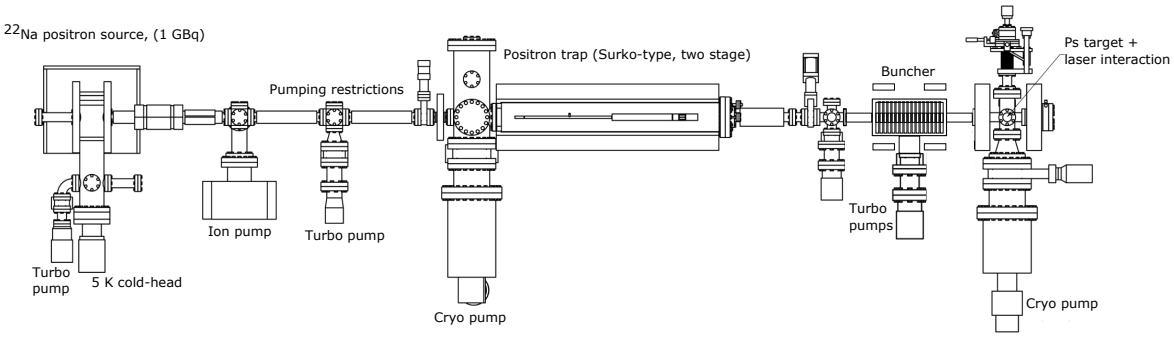

Figure 2.2: Schematic of the positron beam used in the experiments. From left to right; a ^{22}Na β^+ radioactive source is held in a 5 K coldhead where a solid neon moderator is "grown". A series of coils an solenoids then lead the DC positron beam to a Surko-type buffer gas trap, where positrons are accumulated and eventually ejected into a parabolic ring buncher which produces pulses of $\sim$3 ns, which are then guided and implanted into a porous silica target in the Ps-laser interaction region. Also shown below the positron trap is the electrode potential arrangement and approximate nitrogen pressures used to capture and cool positrons. Adapted from [Marjanovi *et al.* 2016].

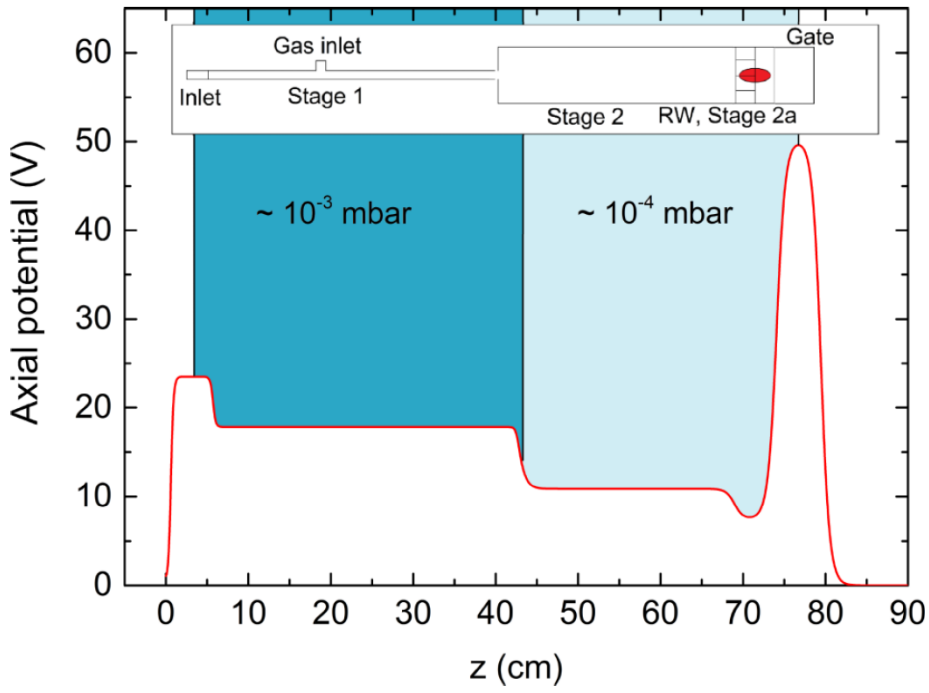

Figure 2.3: Axial electric potential in the trap during loading phase. The reduction in gas pressure from stage one to two increases the lifetime against annihilation in the second stage. The lifetime is increased further with the application of rotating wall compression. From [Cooper *et al.* 2015]

with a rotating wall quadrupole electric field, operating in a non-plasma regime [Cassidy *et al.* 2006a, Greaves & Moxom 2008, Isaac *et al.* 2011]. The rotating wall field induces inward radial transport of the positrons, which reduces collisions with the chamber walls. This is achieved by applying a sinusoidal signal to a segmented electrode (8 segments) in the final stage of the trap, each segment has its signal phase-shifted by $\pi/2$ from the adjacent electrode. Typical sinusoidal frequencies and amplitudes for the rotating wall are of the order of ~ 4.5 MHz and $\sim$500 mV respectively. This increases the lifetime of the stored positrons which is then determined only by annihilation with the N_2 and CF_4 molecules.

The positron beam spot size is reduced via this process, which is a form of loss-free re-moderation [Mills 1980a] (i.e., phase space compression). The Ps-laser interaction region is approximately 1 - 2 m from the trap (depending on experimental setup) and contains a micro-channel plate (MCP) and phosphor screen assembly which are viewed with a CCD camera. These are used to align the positrons to a

well-defined spatial location which is then overlapped by the lasers used for optical excitation. Images of the DC beam and the pulsed trap output are shown in figure 2.4. The annular profile of the DC beam is due to the conical nature of the moderator. The design of the source [Greaves & Moxom 2003] is such that the capsule is not thermally connected to the moderator cone and therefore does not get cold enough for neon gas to freeze onto its window.

The increase in the positron lifetime when the rotating wall field is applied can be seen in figure 2.5, which shows the annihilation signal of the trap output pulse as a function of fill time. The signal is proportional to the number of positrons in the pulse. These data are fitted with

$$N_{e^+} = A(1 - e^{-t/\tau}) \tag{2.1}$$

where τ is the positron lifetime in the second stage of the trap, $A = R\tau$, and R is the positron capture rate. The lifetime in the trap is measured as 1.72±0.07 s and 0.13±0.09 s with the rotating wall on and off, respectively. When the rotating wall field is applied, the measured lifetime is almost entirely due to interactions with gas molecules. Without the rotating wall field, positron diffusion to the electrodes leads to an increased annihilation rate [Deller *et al.* 2014].

The lifetime in the trap is an important factor in determining the repetition rate at which the system is most efficient. This is also informed by other factors; in the case of spectroscopy with pulsed lasers, for example, it is necessary to match the trap and laser repetition rates.

Figure 2.5 shows that the number of trapped positrons begins to saturate above a 2 s fill time, and this sets the lower limit for the trap cycle rate of 0.5 Hz. It would be possible to run at lower repetition rates, but since the number of trapped positrons is not yet saturated, it would be less efficient. The apparatus we describe here cannot produce high positron densities as in [Cassidy *et al.* 2006a], but is suitable for performing optical measurements using a low-density Ps ensemble. The optical excitation is based on a pulsed laser system that can operate at rates between 1 and 10 Hz, and so we use a 1 Hz repetition rate on the positron trap (during the linear

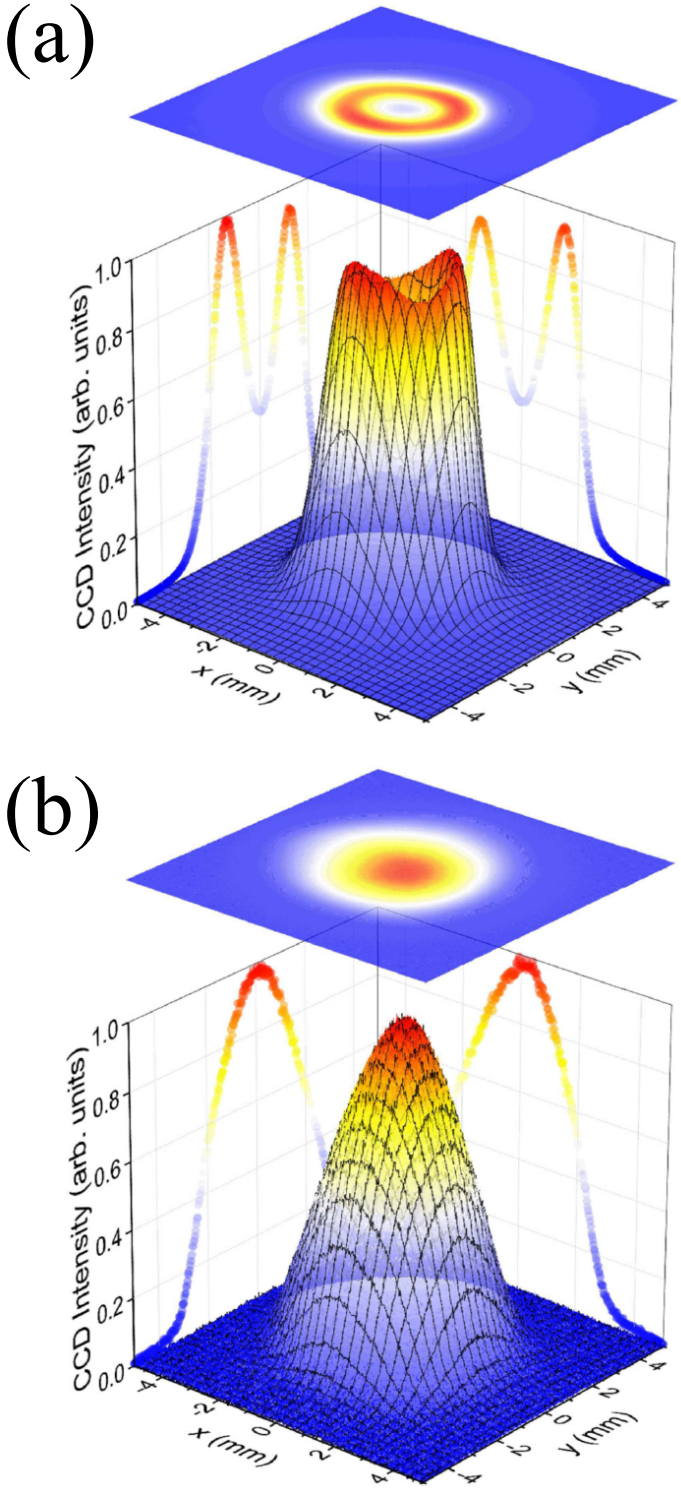

Figure 2.4: (a) DC beam imaged on multichannel plate, phosphor screen assembly with a three dimensional representation and orthogonal line profiles projected onto the axes. The hole in the middle of the beam is due to the conical moderator substrate geometry. (b) Trap output pulse imaged on the same detector. Fitting of the line profiles gives a spatial pulse width of 3.33±0.01 mm FWHM in the wider direction (x-axis). The observed beam size depends on the magnetic field in the target region (130 G). Both (a) and (b) have been normalized to the peak amplitudes. From [Cooper *et al.* 2015]

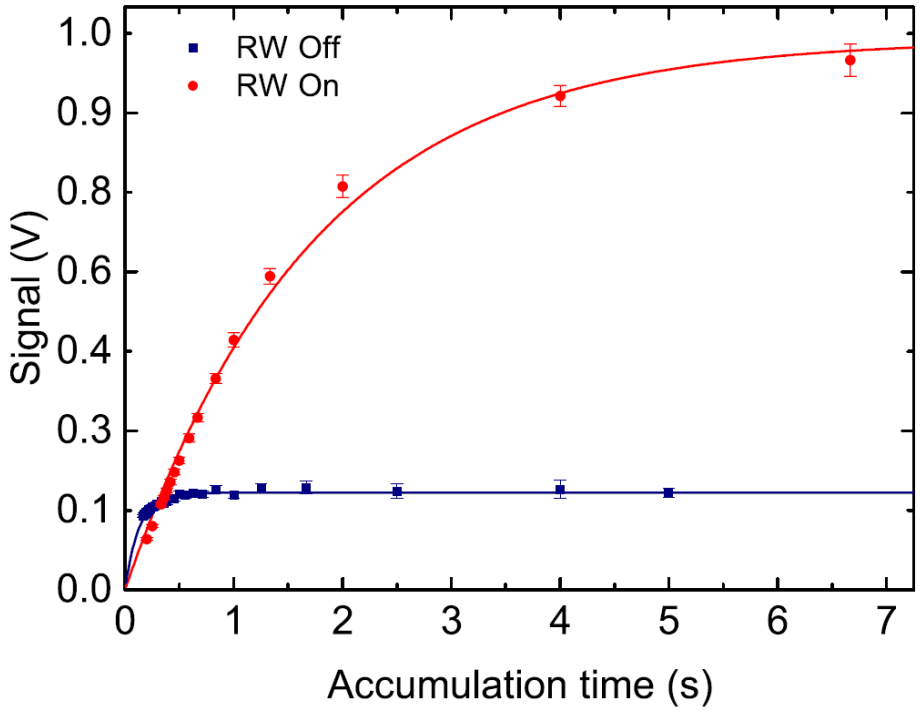

Figure 2.5: Annihilation gamma ray signal of measured from the trap output as a function of positron accumulation time. The lifetime against annihilation within the trap (τ) is estimated by fitting equation 2.1 to the measured data and has a value of 1.72±0.07 s when the rotating wall is being driven at 4 MHz and 4 V. The lifetime reduces to 0.13±0.09 s in the absence of a rotating electric field. From [Cooper *et al.* 2015]

gain in positrons trapped) matched to our laser system also operating at 1 Hz, this would be equivalent to operating at larger repetition rates, such as 10 Hz, however the laser system (including the lifetime of the laser dye) and the electronics pulsing the trap are more stable when pulsing at slower repetition rates, the corresponding signal-to-noise ratios are larger, and thus 1 Hz is more convenient for our apparatus.

We make use of a parabolic harmonic potential buncher (as described in [Mills 1980b] and similar to the one used in [Cassidy *et al.* 2006a]) to maintain the time width of the positrons coming out of our Surko Trap for longer distances, figure 2.6 shows that using this technique we can achieve positron widths of approximately 3 ns approximately 2 m away from the trap, which are ideal for our laser excitation system which has laser pulses of $\sim$ 5 ns.

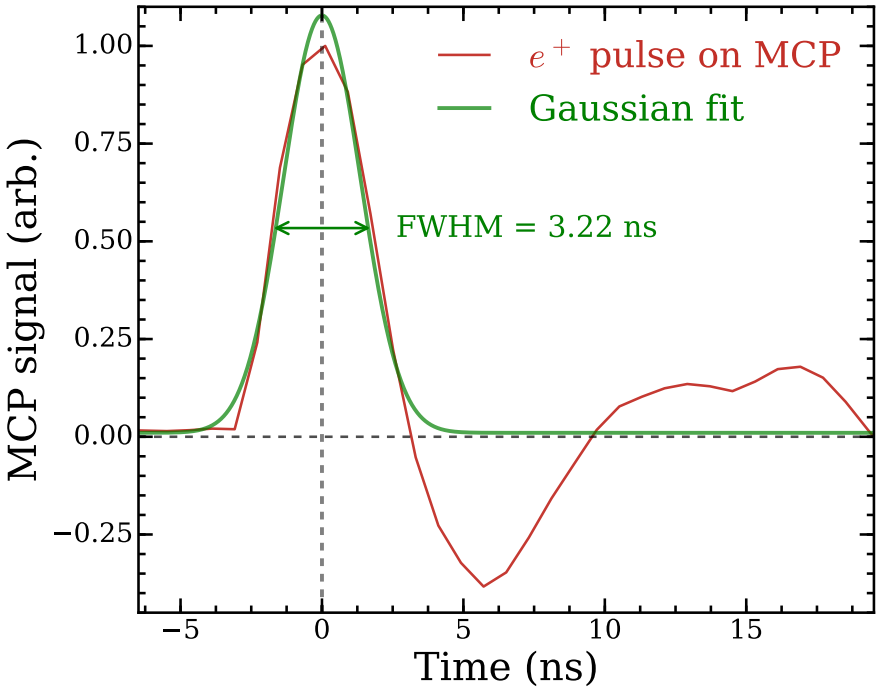

Figure 2.6: Positron signal measured on a double stack Multi-Channel Plate (MCP) at the end of the beamline. The buncher present after the Surko trap enables us to achieve positron pulse widths of ∼3 ns. The amplitude of the signal has been normalized to 1. The negative values of the MCP signal are cable reflections.

2.1.3 Positronium formation

Positron pulses from the buffer gas trap are magnetically guided to an appropriate positron-Ps converter target, for all of the experiments described here, this converter was a porous silica (SiO_2) film [Liszkay *et al.* 2008]. These targets are robust, easy to use, and their Ps production is generally very stable over long periods of time.

Perhaps the most useful feature of these porous silica targets is the fact that the Ps formation mechanism allows for significant cooling [Cassidy *et al.* 2010a] to take place if there are enough collisions of the Ps atoms with the porous network. When the porous silica target is bombarded with positrons that are energetic enough, they penetrate deep into the bulk material, where they capture an electron and become bound, forming ground-state Ps. The newly formed Ps atoms then diffuse through the bulk towards regions of lower potential energy i.e., the pores. While inside the pores the Ps atoms have numerous inelastic collisions with the

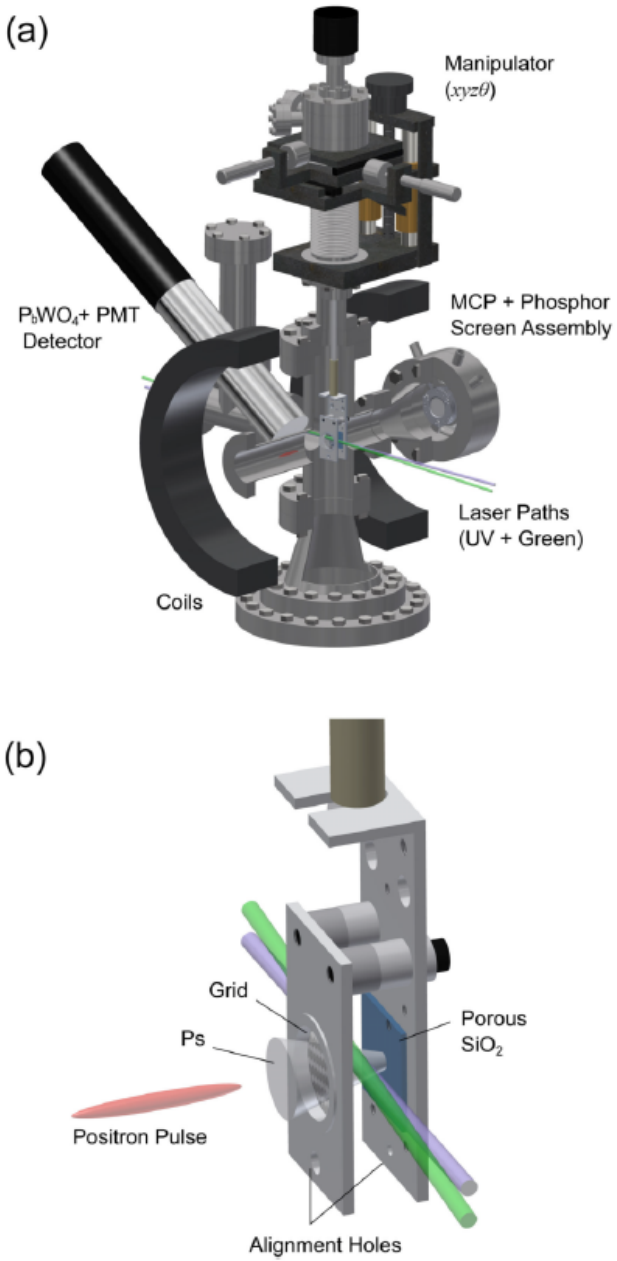

Figure 2.7: (a) Positronium-laser interaction chamber. Two coils surround the chamber producing a magnetic field of ∼130 G. The target may be raised out of view of the positron beam for performing trap diagnostics using the MCP. (b) Zoomed SiO_2 porous silica target mount. The target is mounted behind a tungsten grid which is 90% transmissive. Ps atoms are made within the bulk of the material and emitted into vacuum. A 2 mm diameter alignment hole at the bottom of the mount allows calibration of the CCD camera in order to determine the positron beam size at the target. The hole is also used to match the position of the lasers with the emitted Ps. From [Cooper *et al.* 2015]

internal surfaces, causing them to eventually lose energy to come near to thermalization with the temperature of the target. Positronium atoms eventually diffuse out of the target and are emitted into the vacuum chamber forming a dilute atomic gas. It is worth noting that regardless of the positron beam polarization and efficiency, roughly 25 % of the Ps atoms that are produced as soon as the positrons are implanted, will be in the lowest energy ground state, with a singlet configuration, ($1\,^1S_0$) [Wolfenstein & Ravenhall 1952, Adkins 1983]. Ps atoms in this state have a characteristically short lifetime of 125 ps [Dirac 1930], meaning that annihilations events due to decay of Ps from this state occur so quickly that they are indistinguishable by our timing detection techniques [Cassidy *et al.* 2006b] from direct positron-electron annihilation when the positrons are implanted into the sample. The Ps formation process on a typical porous silica sample is approximately 30 % efficient (i.e., about 30 % of the positrons implanted in the target become o-Ps). The geometry of the interaction region is shown in Figure 2.7.

2.2 Laser setup

All spectroscopic measurements performed in this project excited ground state Ps to the first excited state, $n = 2$, via optical electric dipole transitions, i.e. $1\,^3S_1 \rightarrow 2\,^3P_J$. Radiation of 243 nm is required to drive this transition. Such radiation was achieved by first producing short ($\sim$ 5 ns) pulses of 1064 nm radiation from a solid-state Q-switched neodymium-doped yttrium aluminum garnet (Nd:YAG) laser, yielding pulses of up to 700 mJ of energy per pulse. This radiation is then passed through a nonlinear doubling crystal made of potassium dihydrogen phosphate (KDP). This crystal is used to double the frequency of the incoming light and produces laser pulses with wavelength 532 nm of up to 220 mJ per pulse. The residual 1064 nm laser radiation is then mixed in with the 532 nm light in another KDP non-linear crystal, thereby generating the third harmonic with wavelength of 355 nm, and pulses of up to 130 mJ.

The 355 nm third harmonic is then used to pump a pulsed dye laser (Sirah Cobra Stretch). The lasing medium is Coumarin 102 and it was used to produce

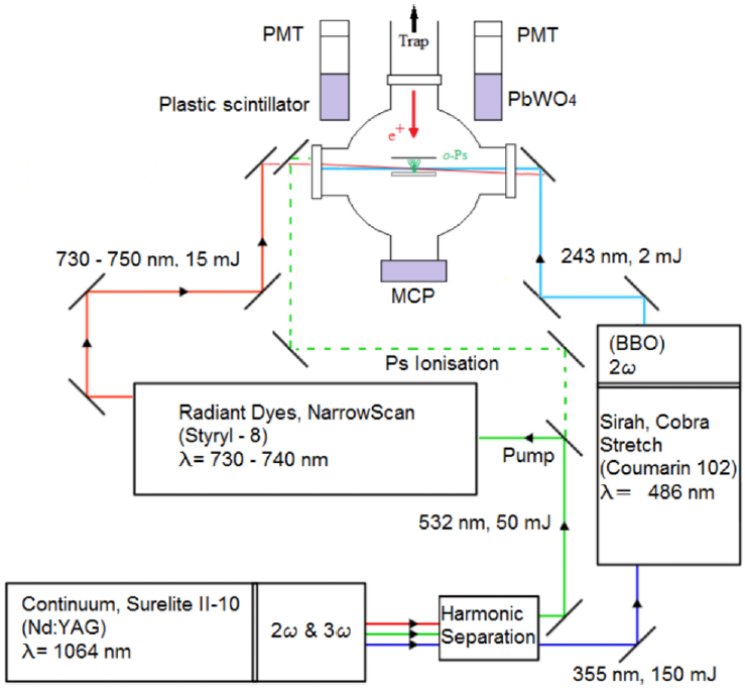

Figure 2.8: Laser system schematic. The system can be modified for either 730-750 nm (IR) Rydberg state production or photoionisation of 2P state Ps with residual 532 nm (green) light. From [Cooper *et al.* 2015]

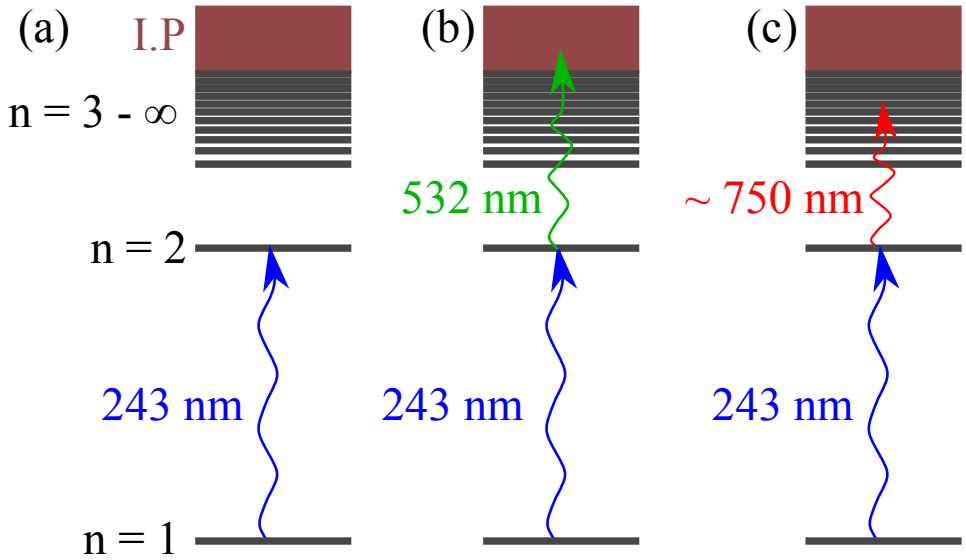

Figure 2.9: Three different excitation schemes described in figure 2.8. Single-photon excitation $1\,^3S_1 \rightarrow 2\,^3P$ with 243 nm UV radiation (a). Two-photon photoionization using additional 532 nm light to excite beyond the ionization potential (I.P) (b). Two-photon excitation ($1\,^3S_1 \rightarrow 2\,^3P \rightarrow n\,^3S/^3D$) to an arbitrary Rydberg state ranging $n = 9 - \infty$ using tunable IR laser (c).

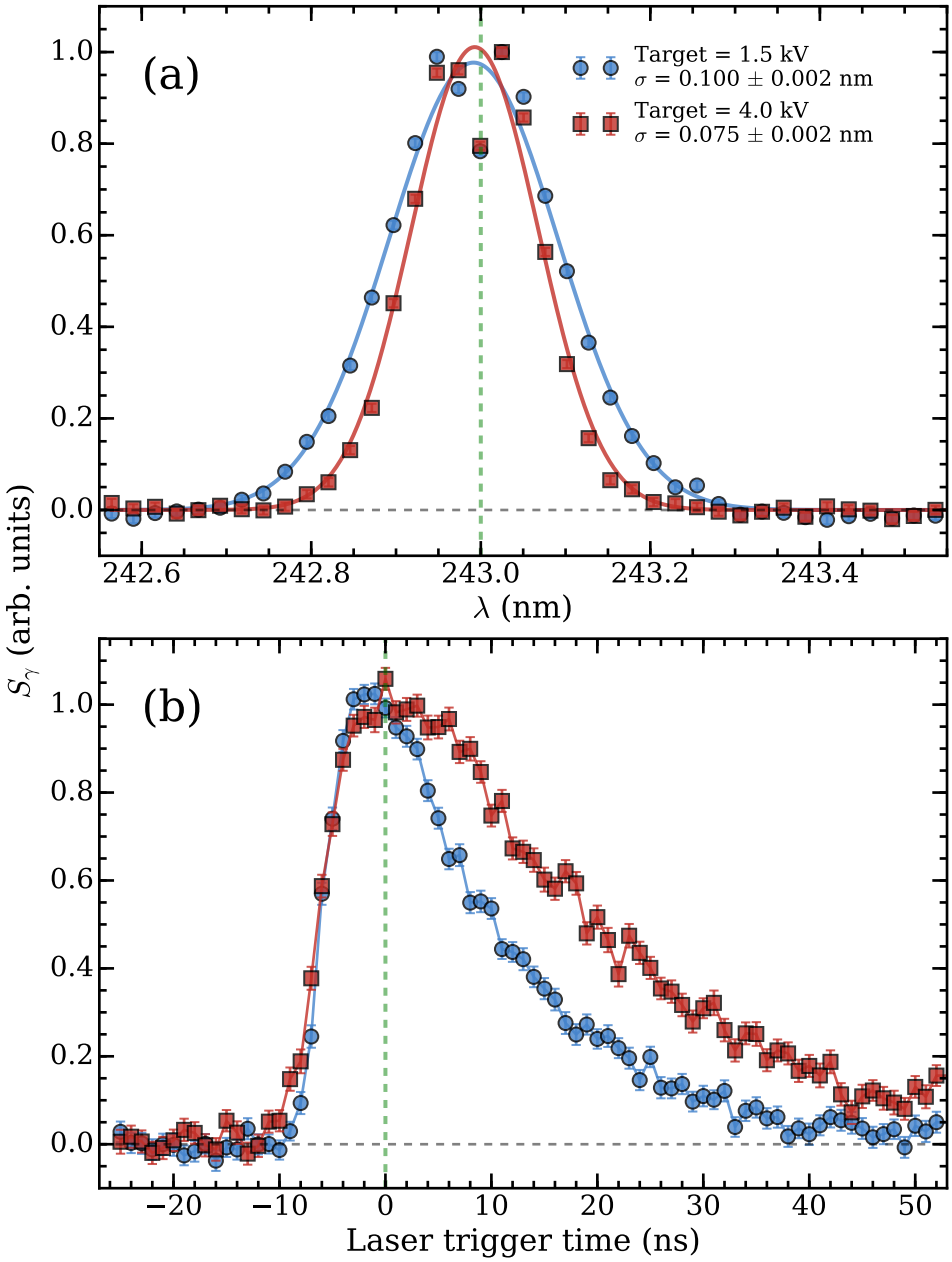

Figure 2.10: Spectrum of $n = 1 \rightarrow n = 2$ lineshape transition (a). This excitation was performed by exciting Ps from $n = 1$ to $n = 2$ with the 243 nm UV laser, and subsequently ionizing the $n = 2$ states with the 729 nm IR laser. The excitation was done for a target implantation energy of 1.5 kV (blue circles) and 4 kV (red squares), higher implantation energy leads to more collisional cooling in the SiO_2 porous structure and thus the Doppler width (σ) is reduced. The Lamb dip visible for both cases in the center of the lineshape is caused by reflected UV light from the vacuum windows. (b) Is a generic laser trigger delay scan. The Laser trigger time is the trigger for both the UV and IR lasers. It can be seen that the Ps beam and the lasers do overlap in time for ∼40 ns and ∼50 ns for 1.5 kV and 4 kV implantation energy respectively since the atoms produced by 1.5 kV implantation are on average faster than the 4 kV, then the interaction time with the laser beams is reduced. The data shown in (a) was taken in both cases for the trigger time = 0.

radiation of wavelength 486 nm, in pulses of up to 30 mJ, this laser light is then doubled in a beta barium borate (BBO) crystal to produce pulses of up to 4 mJ of laser radiation of wavelength 243 nm and bandwidth of 85 GHz (such large bandwidth was achieved by forming a cavity with a set of prisms instead of a grating), this is the beam that is used in all of our experiments to excite Ps from $1\,^3S_1$ to $2\,^3P_J$ [figure 2.9(a)].

After the 1064 nm radiation is doubled into 532 nm, and these two are mixed to produce the third harmonic 355 nm, there is still some leftover 532 nm light that could then be used to simultaneously pump a second dye laser (Radiant Narrowscan) with a lasing medium (Styryl 8) that was used to produce radiation of wavelength between 729 nm and 770 nm. This light was used to either directly ionize Ps once it had been excited to $n = 2$, or to further excite it to a Rydberg state via a $2\,^3P_J \rightarrow n\,^3S/^3D$ transition [figure 2.9(c)]. Sometimes, instead of infra-red (IR) light of wavelength 729 nm and bandwidth of 5 GHz, the residual 532 nm beam was used to ionize Ps [figure 2.9(b)], this is shown by the dashed green line in figure 2.8. The three possible excitation schemes are depicted in figure 2.9. It is worth noting that for the case of the IR and UV lasers, we were able to control the polarization of the laser pulse by passing the beams through wavelength-appropriate half-waveplates and Glan-Taylor polarizer beamcubes, thus producing linear polarizations with purities of $> 95\%$.

Figure 2.10(a) shows a Doppler spectrum of Ps being excited from $n = 1$ to $n = 2$ by the 243 nm UV laser, and subsequently ionized by the IR laser. The width of the Doppler lineshape is affected by the implantation energy of the positrons (1.5 kV and 4 kV respectively for the two sets of data) since the higher the implantation energy, the more collisions the Ps atoms will have with the porous network walls and will therefore cool down further. Before interacting with the lasers. Figure 2.10(b) also shows a typical laser excitation delay scan which is performed to optimize the laser excitation before every measurement. The time at which both lasers are fired is scanned with a delay generator, in this case we are able to identify the optimum laser trigger time (shown at 0 in figure 2.10(b), this corresponds to $\sim$450 ns after the

Surko trap voltages are lowered). It can be seen from the width of the laser delay curves, that the faster atoms (corresponding to the 1.5 kV implantation energy, blue circles) have less interaction time with the lasers than the slower atoms, as is to be expected.

2.2.1 Applying parallel electric and magnetic fields

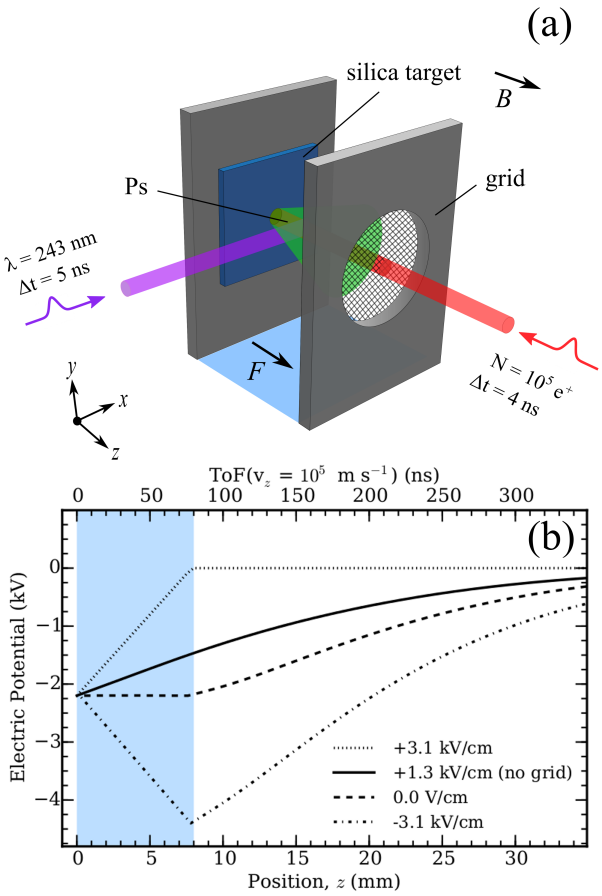

Figure 2.11: (a) Schematic diagram of the Ps formation and laser interaction region. The green cone emanating from the porous silica represents Ps formed by implanting positrons into the film. (b) Calculated electric potential in the target region, the legend indicates the magnitude and direction of the electric field in the area between the target and the grid indicated by the (blue) shaded strip. The flight time for Ps with a velocity of $v_z = 10^5$ ms^{-1} is shown on the top axis. From [Alonso *et al.* 2016b]

For all of the experiments described in this project, the applied electric field in the laser excitation region must be controlled independently of the other experimental parameters. This is achieved by placing a transmissive (∼90 %) tungsten mesh in front of the porous silica target. This is shown in figure 2.11(a), the voltage

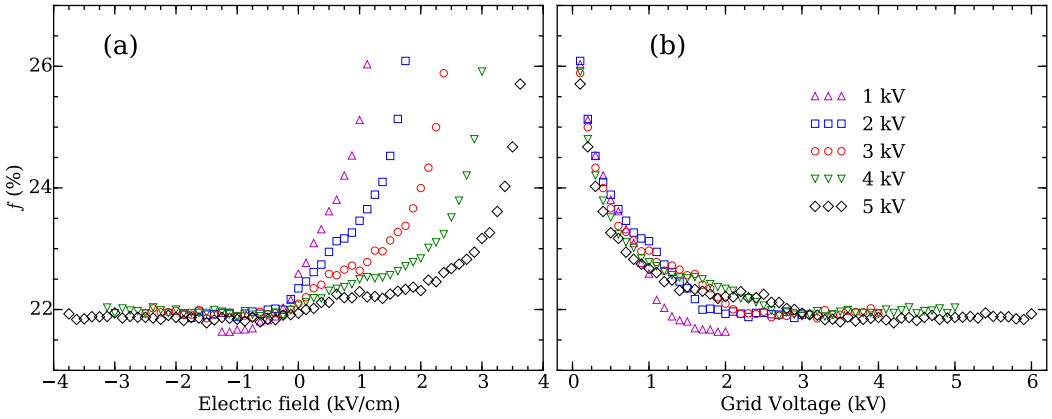

Figure 2.12: (a) Measurements of f (see equation 2.2) as a function of the electric field in the interaction region. The measurements were performed for five different target voltages (which define the positron pulse implantation energy) and the field was modified by changing the voltage applied to the grid [see figure 2.11(a)]). (b) as (a) but displayed as a function of the applied grid voltage, showing that the increase in f for high positive electric fields is due to grid-formed Ps alone. The error bars are smaller than the symbols in both plots. From [Alonso *et al.* 2016b]

applied to the mesh can be controlled independently of the voltage applied to the target holder. Therefore, adjusting the grid voltage allows us to change the electric field in the laser excitation region [the region shaded in blue in figure 2.11(a) and (b)] without changing the implantation energy of the positrons onto the silica sample, which is solely controlled by the voltage applied to the target holder.

Figure 2.11(b) shows the electric potential (and the electric field in the excitation region, displayed in the legend) for various different grid biases (and the case with no grid). As it can be seen, the electric field in the excitation can be controlled, while the final electric potential (i.e, implantation energy) remains the same.

Even though this tungsten grid allows us to easily control the electric field, it does add one complication; it can lead to undesired Ps formation on the surface of the grid. However, this can be avoided by increasing the voltage of the grid beyond ~ 2 kV. At these energies the positrons do not interact significantly with the surface of the grid, and the amount of undesirable "grid Ps" is suppressed. This effect can be seen in figure 2.12 where the ammount of grid Ps was shown to be reduced as a function of the grid voltage, for a range of different target implantation energies.

2.3 Detection techniques

2.3.1 Positronium fraction and signal parameter S_γ

The main detection technique used in the experiments reported here makes use of the annihilation gamma-rays that are produced when Ps self-annihilates, when Ps is ionized and the released positron directly annihilates when it comes into contact with a solid surface or when Ps hits a wall directly and the positron annihilates. We employ single-shot positron annihilation lifetime spectroscopy (SSPALS) [Cassidy *et al.* 2006b]. A fast detector is coupled to an oscilloscope, and the time-dependent detector anode voltage $V(t)$ is measured directly. This signal is proportional to the amount of annihilation radiation, and the resulting waveform constitutes a lifetime spectrum. Examples of such spectra are shown in figure 2.13. In the present work on the order of 10^6 gamma-rays result from each positron pulse, approximately 5 % of which are subsequently detected, depending on the detector solid angle described for each measurement. The most common detector used for these kind of experiments has been for a long time a lead tungstate (PWO) scintillator, optically coupled to a photo-multiplier tube [Cassidy & Mills 2007] (although it will be explained in Section 2.3.2 that LYSO scintillators are being used now as well, yielding signal to noise ratios approximately $\times 3$ higher). The SSPALS time resolution is determined primarily by the $\sim$ 12 ns PWO scintillator decay time, which is sufficient to study processes that occur on the $\sim$ 100 ns time-scale of triplet Ps decay.

The SSPALS signal is parametrized by f, the fraction of the lifetime spectrum in a selected time region, where

$$f = \int_B^C V(t)\, dt \Big/ \int_A^C V(t)\, dt \; . \tag{2.2}$$

The time windows are selected depending on the experimental parameters and detectors being used; when we wish to study laser-induced changes in Ps lifetimes that occur on a short time scales relative to the typical decay rate of the $1\,^3S_1$ ground-state, the time windows used were approximately A = -3 ns, B = 35 ns and C = 450

ns (for a PWO scintillator, where B = $3 \times \tau_{PWO} \simeq 35$ ns, where τ_{PWO} is the mean relaxation time for PWO). However, if we wished to study long-lived states such as Rydberg states, these time windows would have to be changed. Note that while the value of f depends on the choice of the time windows (A, B, and C), and is therefore arbitrary; for certain configurations it depends almost linearly on the positronium formation fraction, as discussed in [Cassidy *et al.* 2011a].

We characterize laser-induced effects on Ps decay rates using the parameter

$$S_\gamma = \frac{(f_{\text{Back}} - f_{\text{Sig}})}{f_{\text{Back}}}, \tag{2.3}$$

where $f_{\text{Back.}}$ refers to background measurements with no lasers present, and $f_{\text{Sig.}}$ refers to the signal when the laser is on, as shown in figure 2.13. When there is a

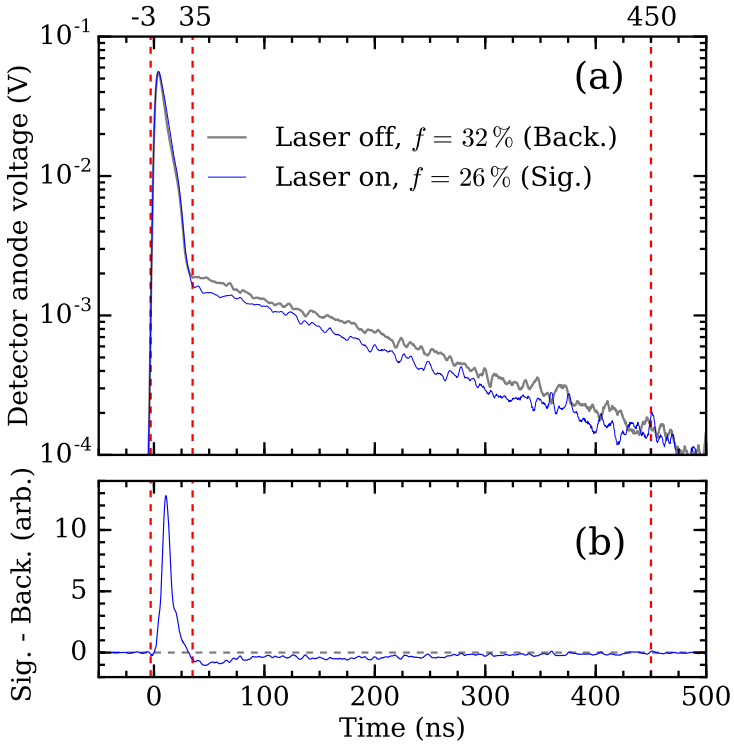

Figure 2.13: (a) Example of SSPALS lifetime spectra for a PWO scintillator recorded with the lasers off resonance (continuous gray line) and on resonance (continuous blue line). (b) Subtraction of background data from signal. These spectra were recorded at a magnetic field of B = 130 G and an electric field of $F = 1330$ V/cm. Each set of data is the average of 40 pulses. Shown as vertical red dashed lines are the positions of the time windows A (-3 ns), B (35 ns), and C (450 ns).

magnetic field present ($\sim$ 100 G), if Ps atoms are excited to 2^3P_J levels in zero-field, and subsequently return to the 1^3S_1 level (either via spontaneous or stimulated emission) we would measure $S_\gamma \simeq 0$, because the lifetime spectra are not significantly altered by the small decrease in the total Ps decay rate. However, if annihilation occurs as a result of excitation, then we would measure positive values for S_γ, and conversely, if atoms are excited to states with a longer lifetime than the background (such as Rydberg states), we would observe negative S_γ values, assuming the applied fields are the same.

2.3.2 SSPALS optimization and use of LYSO vs PWO

A lot of the results presented in this thesis were focused on the production and study of Rydberg Ps atoms using low-intensity, low-density, positron pulses [Cassidy *et al.* 2012a, Jones *et al.* 2014, Wall *et al.* 2015]. Since these atoms are generally long lived [Gallagher 1994], the timing constraints on an appropriate SSPALS detector may be relaxed for Rydberg studies. The $\sim$ 12 ns decay time of PWO is well-suited for the study of short-lived effects since it allows one to integrate lifetime spectra almost from the moment of Ps atom creation. With long-lived Rydberg states, however, the annihilation events of interest may occur on completely different time-scales, and the regions of interest in the corresponding lifetime spectra will change accordingly [Cooper *et al.* 2015, Alonso *et al.* 2016a]. Therefore, for measurements of this kind it can be advantageous to use a slower scintillator with a higher light output. We have tested this using Cerium doped lutetium yttrium oxyorthosilicate, ($Lu_{2(1-x)}Y_{2x}SiO_5$:Ce), or, LYSO. LYSO [Cooke *et al.* 2000] has a useful combination of properties, namely its short radiation length ($\sim$ 1 cm), high density (8 g cm^{-3}), high light output ($\sim$75% of NaI), and relatively fast decay time (40 ns).

In order to directly compare the performance of PWO and LYSO, we performed a series of measurements where both detectors were used to record data simultaneously, in a symmetric arrangement at the same distance from the Ps excitation region. This is indicated in figure 2.14, the solid angles subtended by each detector relative to the Ps production region were approximately equal. The PMT's

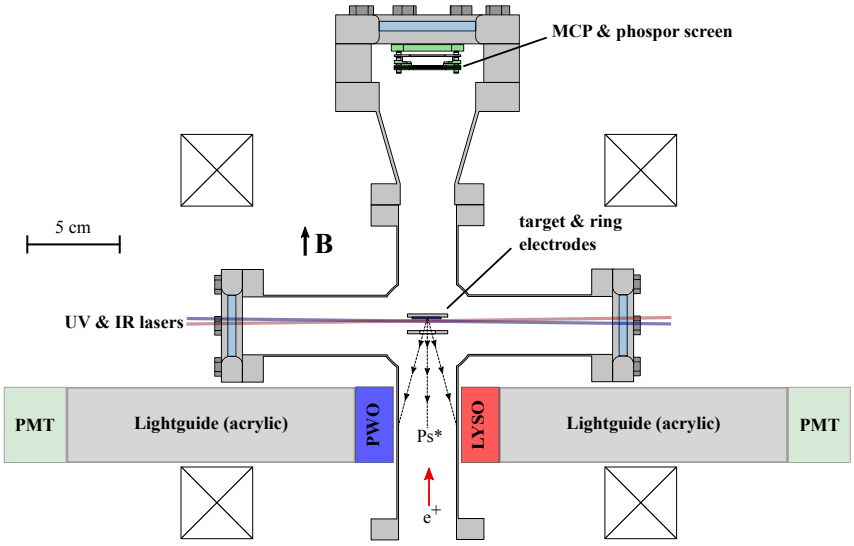

Figure 2.14: Schematic layout of the target chamber and gamma-ray detectors used to compare PWO and LYSO detectors. From [Alonso *et al.* 2016a].

used in each case were different. The LYSO detector was attached to an EMI type 9954KA PMT operated with a supply voltage of -0.9 kV. The PWO was attached to a Hamamatsu H10570 PMT, operated with a supply voltage of -1.4 kV. These supply voltages were chosen to avoid PMT saturation and resulted in similar pulse amplitudes.

The output obtained using LYSO and PWO detectors are shown in figure 2.15. The integration regions given by A, B and C are selected according to the type of detector used, and also the processes to be studied. The amount of Ps formed is related to f (see [Cassidy *et al.* 2011a]) but numerous factors must be accounted for before a direct conversion to the actual Ps fraction can be extracted. The spectra in figure 2.15 have been analyzed using $B = 3 \times \tau$, where τ is the scintillator decay constant (see f values in figure 2.15). This makes it likely that a significant fraction of the integrated spectrum will be due to photons originating from long-lived Ps annihilation, as opposed to light from the prompt peak delayed by the scintillator decay.

Figure 2.16 shows f obtained from the data of figure 2.15 using different values of of B. These data indicate that if B is too close to the prompt peak events that are not related to Ps formation are included in the signal, giving a higher f. Conversely,

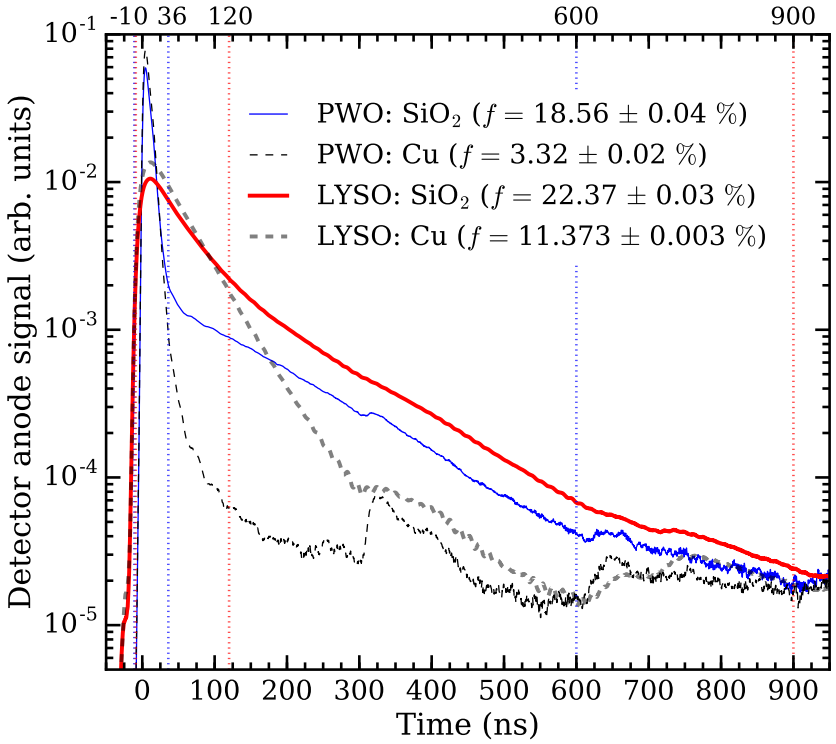

Figure 2.15: SSPALS lifetime spectra recorded with PWO and LYSO detectors, with positrons implanted into a SiO_2 or a piece of untreated Cu, as indicated in the legend. These spectra are the average of 860 individual shots and were acquired in approximately 15 minutes. The quoted f values were calculated using the indicated time windows as described in the text and represented by the color-coded vertical dashed lines and the corresponding labels above, (i.e., for PWO the boundaries A, B and C were -10, 36, and 600 ns respectively and for LYSO the boundaries A, B and C were -10, 120, and 900 ns respectively). From [Alonso *et al.* 2016a].

if B is too far away from the peak the signal will miss events that are caused by Ps annihilation, giving a lower f. For PWO there is a clear increase in the smoothly varying f when B is less than around 30 ns, indicating that this is the point at which peak events start to be included.

For LYSO the time at which the faster f increase occurs is less obvious, but is in the region of $B \sim 150$ ns. Thus, the optimal region of integration for this detector excludes the signal due to Ps decay for around one lifetime, which is the primary reason why PWO was initially selected for SSPALS experiments [Cassidy & Mills 2007]. These data demonstrate that f cannot be interpreted directly as the Ps fraction, since one can never integrate all the way to zero time.

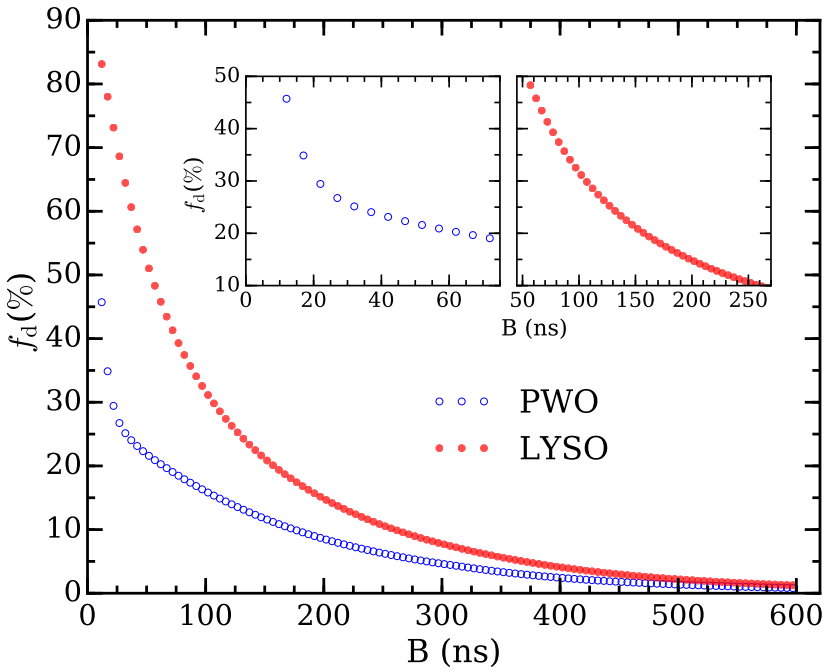

Figure 2.16: f obtained using different values of B for LYSO and PWO detectors. The values of A and C were -10 ns and 600 ns respectively for PWO, and -10 ns and 900 ns for the LYSO detector. The two insets show the region where peak events stop being included in f as explained in the text. From [Alonso *et al.* 2016a].

Moreover, there are other factors that must be included, such as background signals and the efficiency with different photon energies are detected [Cassidy *et al.* 2011a].

There are several processes that may increase or decrease Ps decay rates, when studying such effects using S_γ as the metric it is necessary to adjust the integration parameters (*cf* equation 2.2) according to the relevant time scales. That is, the optimal analysis will differ depending on whether the Ps atoms are being made to annihilate at a rate that is faster or slower than the unperturbed vacuum rate.

Figure 2.17 shows lifetime spectra measured with both a LYSO and a PWO detector, obtained with the IR laser tuned to excite $n = 2$ atoms to the $n = 45$ level. These atoms (which we cannot resolve spectroscopically [Wall *et al.* 2015]) are field ionized in an electric field of ~ 100 V cm^{-1}. The increased annihilation due to this ionization can be observed most clearly in the difference spectra, shown for both detectors in figure 2.17 (b). The initial signal (observed for times ≤ 50 ns) is due to laser induced annihilation events, while the later negative dip peaking

at around 400 ns is due to the absence of annihilation events. Similar profiles are obtained if the $n = 2$ Ps atoms are directly ionized using IR light at 729 nm.

The two peaks (also seen with direct ionization) are due to positrons that do not immediately return to the target and annihilate. These cannot be directly resolved with the LYSO detector, although there is a visible shoulder in the difference curve. This illustrates the fact that there may be some measurements for which the superior time resolution of PWO might make it a better choice, despite the reduced efficiency.

Data of the type shown in figure 2.17 can be analyzed to obtain S_γ values by selecting the most appropriate values of the time windows used to generate the

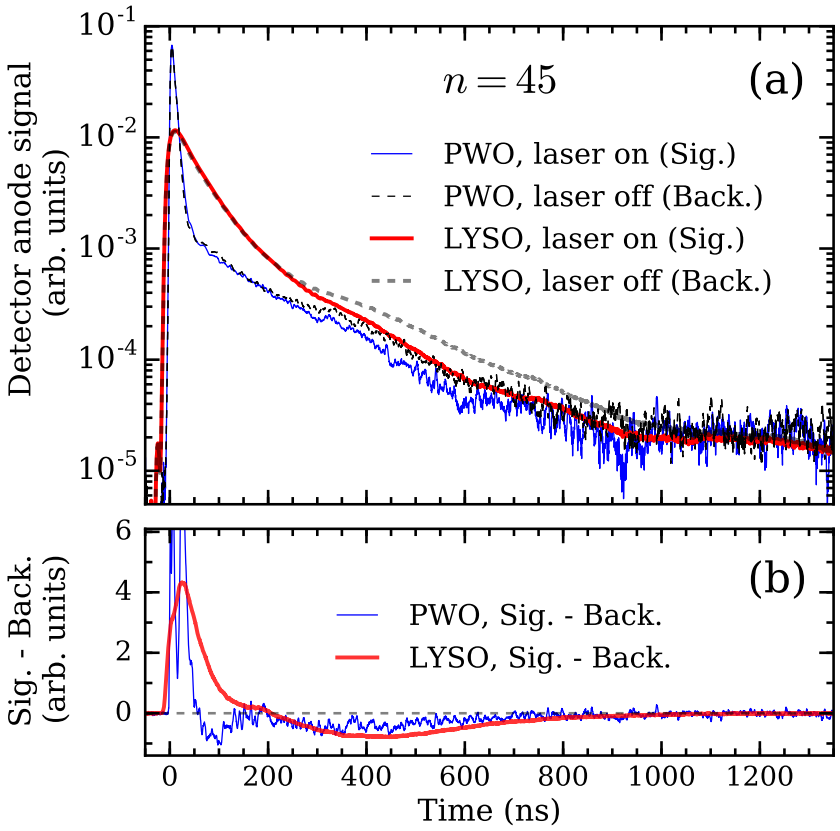

Figure 2.17: (a) Single-shot lifetime spectra from LYSO and PWO detectors with the IR laser tuned to excite $n = 2$ Ps to $n = 45$ ($\lambda = 730.45$ nm) and (b) the difference between the laser on and off spectra shown in (a). The spectra are averages of 275 individual shots and are all normalized to the area between -10 ns and 1200 ns. Note that in (b) the PWO early peaks are truncated to better illustrate the difference in the statistics between the two data sets. The amplitudes of the first and second peaks are 6 and 10 respectively. From [Alonso *et al.* 2016a].

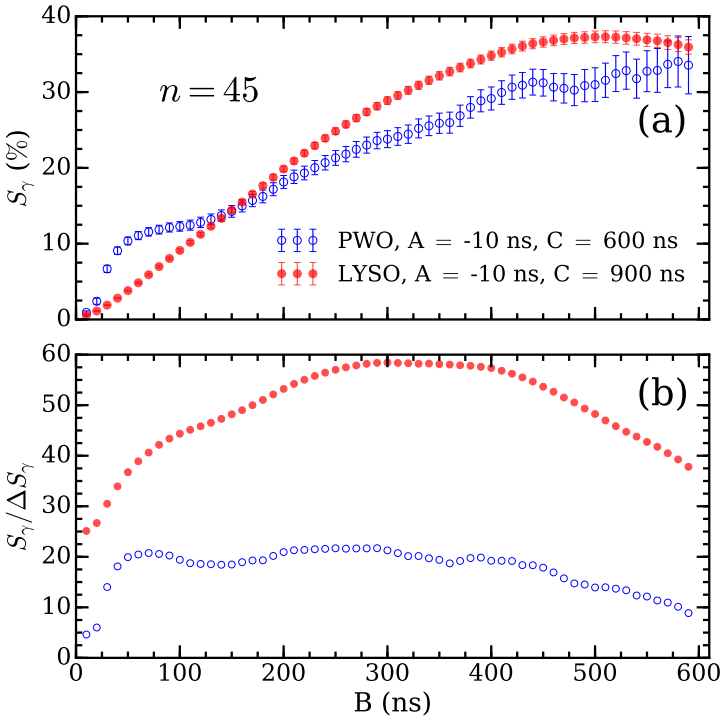

Figure 2.18: (a) The signal S_γ and the SNR (b) obtained from the data shown in figure 2.17 as a function of the integration bound B. From [Alonso *et al.* 2016a].

f values (see equation 2.3). That is, just as the measurement of the amount of ground-state Ps present (i.e., f) can be optimized by choosing B appropriately (see figure 2.16), so too is S_γ highly dependent on the choice of B. In this case, however, one has to select B based on the specific process being measured. In general the values for A and C are fixed by the interval over which annihilation radiation can be detected, although one can partially reduce the amount of noise in the signal by restricting C.

Figure 2.18 shows S_γ and the signal-to-noise ratio (SNR) obtained from the data shown in figure 2.17 as a function of B, in this case, the "noise" is defined as the uncertainty in the signal parameter S_γ. It is evident from these data that there is an optimal integration region that enhances not only the magnitude of the signal but, more importantly, the SNR. It can also be seen from figure 2.19 that the C boundary does not usually need too much optimization, besides simply checking if it is too small to include all the features in the spectrum, and not long enough to include electronic noise and/or ion after-pulses.

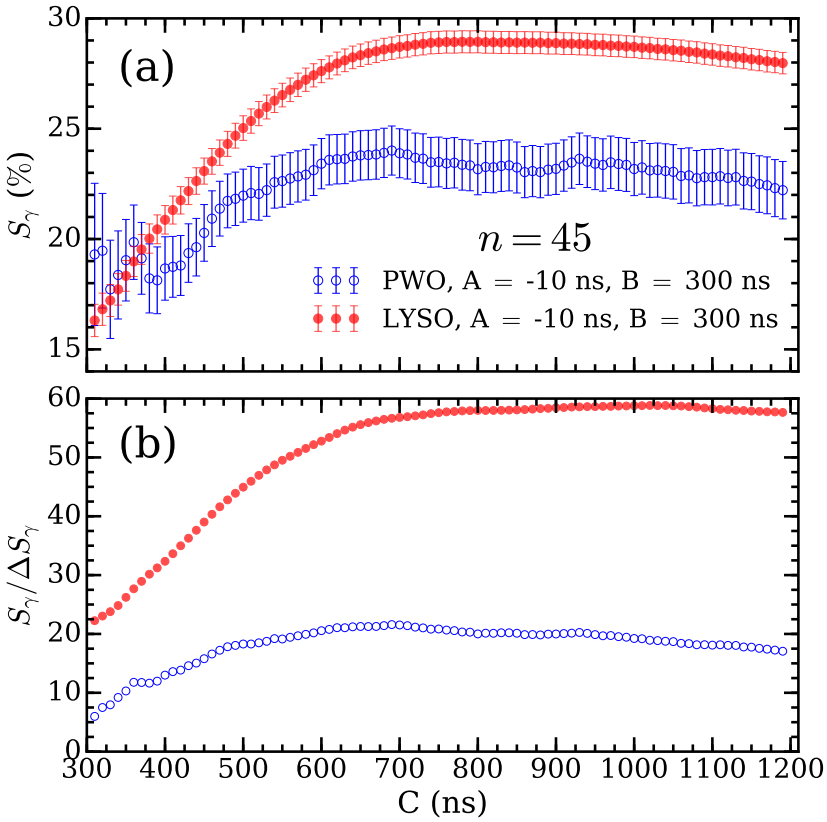

Figure 2.19: (a) The signal S_γ and the SNR (b) obtained from the data shown in figure 2.17 as a function of the integration bound C.

The data shown in figure 2.20 are significantly different to those of figure 2.17. When longer-lived atoms are generated, the laser-on curves exhibit an increase in the gamma-ray signal at later times rather than a deficit. Accordingly, the difference curves are inverted, with a dip at early times indicating fewer annihilations, and a peak at later times due to increased annihilations following wall collisions. There is also a small peak evident at around 100 ns, which is due to Ps atoms annihilating on the grid electrode located around 8 mm from the Ps target (see figure 2.14). The apparent shift in time of the LYSO difference curve relative to the PWO is due to the different time response of the detector, and also the fact that the LYSO is able to detect later events more efficiently than the PWO.

Figure 2.21 shows S_γ and the SNR obtained from the data shown in figure 2.20 as a function of B. This is the same analysis used to generate figure 2.18 but in this case a negative signal is obtained, since the delayed annihilations are increased

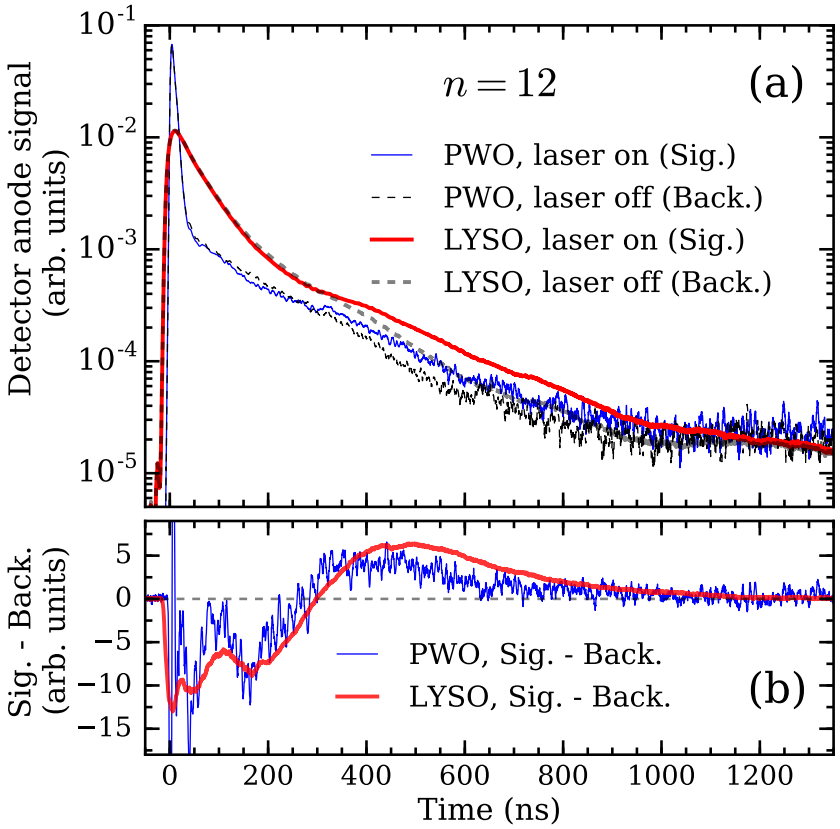

Figure 2.20: (a) Lifetime spectra recorded simultaneously with LYSO and PWO detectors with the IR laser tuned to excite $n = 2$ Ps to $n = 12$ (λ = 749.84 nm) and (b) the difference between the laser on and off spectra shown in (a). The spectra are averages of 400 individual shots and are all area normalized. From [Alonso *et al.* 2016a].

by the laser excitation. These data show that maximizing S_γ does not in general optimize the SNR.

The primary conclusion of these results [figures 2.21(b) and 2.18(b)] is that the high light output from LYSO offers a significant improvement over PWO in terms of the SNR, even when Ps is probed at early times. This is demonstrated explicitly in figure 2.22, which shows the SNR as a function of the data acquisition time. These data are obtained using optimal time windows. The LYSO SNR is around a factor of 3 higher than the PWO SNR, indicating that the data acquisition time could be reduced by almost an order of magnitude without degrading the statistics. The statistical limitations in any measurement will also be affected by other noise sources, such as electronic noise from the PMT, RF pick-up from the high voltage

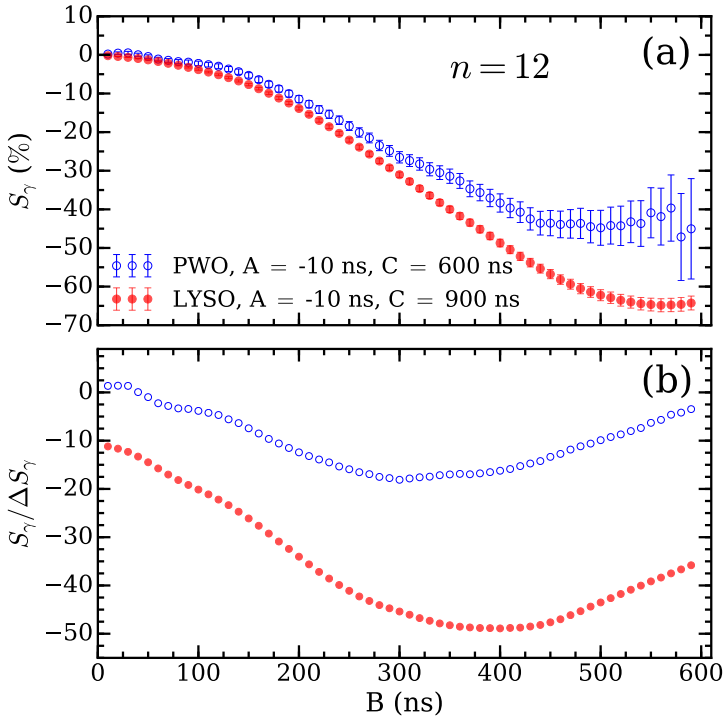

Figure 2.21: (a) The signal S_γ and the SNR (b) obtained from the data shown in figure 2.20 as a function of the integration bound B. From [Alonso *et al.* 2016a].

buncher, digitization noise from the oscilloscope, and so on. However, these will be mostly the same regardless of the type of scintillator used.

As may be seen in figure 2.18 and 2.21, the magnitude of the signal parameter S_γ depends on the time windows selected. It also differs in the two types of measurements performed ($n = 45$ and $n = 12$) because the solid angle subtended by the detectors are different, making them less sensitive to annihilations occurring at earlier times. Nevertheless, S_γ can be used to monitor relative changes in excited-state populations, such as may be obtained in laser spectroscopy.

2.4 Time-of-flight event counting algorithm

For some of the experiments described in this thesis Ps atoms traveled large distances (up to ~ 1.2m) before being detected [Deller *et al.* 2016b]. Such flight times can be on the order of tens of microseconds, and involve placing detectors (LYSO and NaI scintillators, as well as MCP stacks) far away from the Ps production region, where SSPALS methods would have been impractical, and thus we used a

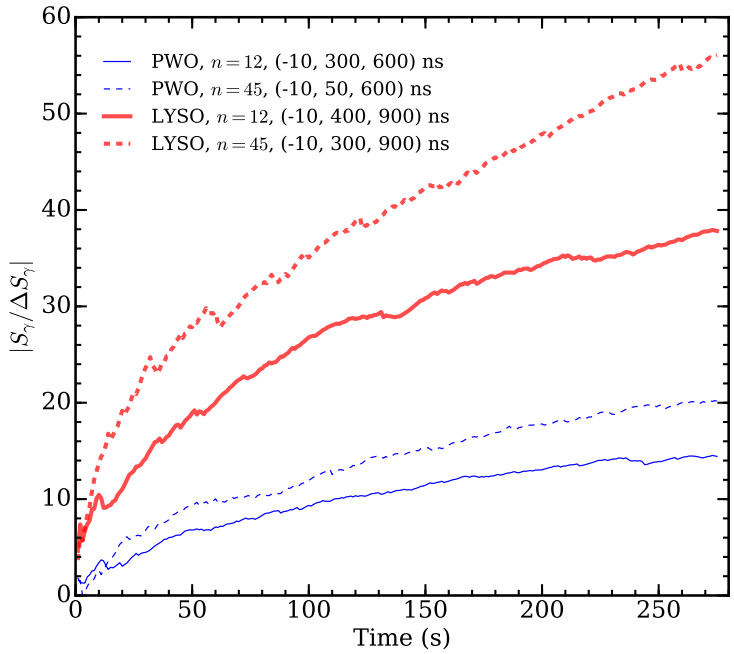

Figure 2.22: The SNR for LYSO and PWO detectors as a function of the data acquisition time. Data are shown for the two cases considered in the text, namely field ionization of $n = 45$ Ps, and delayed collisions of $n = 12$ Ps with the chamber wall. The acquisition rate was 1 Hz. The values of A, B and C used in the analysis are given in the legend for each case in the format (A, B, C). From [Alonso *et al.* 2016a].

standard single-event counting routine.

Figure 2.23 shows a waveform recorded by a NaI detector placed 1.2m away from the Ps formation region. The events being recorded are gamma rays generated by long-lived Rydberg Ps atoms traveling to the end of a long vacuum tube and annihilating. For different measurements we used also LYSO detectors in the same manner. By counting the arrival time of γ-rays registered at the end of the flight path relative to the positron implantation time, TOF spectra can be obtained.

The detector output was recorded with an oscilloscope, triggered by the trap dump sequence. The waveforms were recorded in 6 ns time bins for a period of 20 μs.

The occurrence of trigger events was determined by post-processing the recorded detector waveforms; a trigger was registered if the signal fell below a threshold of -1 mV for a period of at least 100 ns. The time of the leading edge, the amplitude, and the width of each trigger event were recorded (see figure 2.23).

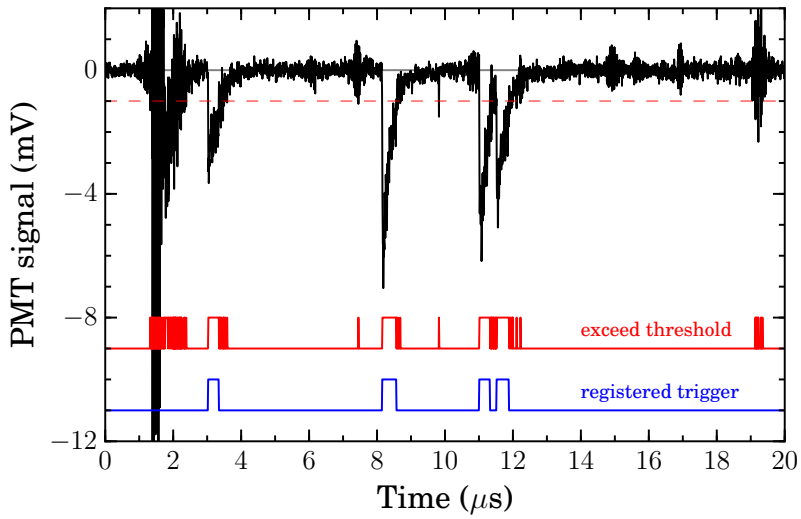

Figure 2.23: The PMT signal recorded for a single Rydberg-Ps-formation cycle (black). The sections where the signal exceeds a threshold of −1 mV (dashed line) are shown in red. The leading edges of above-threshold sections that are at least 100 ns wide are registered as trigger events (blue). From [Deller *et al.* 2016b].

Since this is leading edge counting, the timing resolution was determined primarily by the oscilloscope sample interval, rather than the long decay time of the NaI crystal. As the waveforms are recorded in their entirety, the threshold conditions can be adjusted after-the-fact to minimize true event rejection and reduce the rate for double-counting or false triggers. The absolute detection rate was usually between 1 and 4 events per shot, and trigger pile-up was therefore negligible. Additionally, when using this same technique but using different scintillators or making different measurements, the acceptance parameters of threshold amplitude and width were modified in each case to minimize the number of background events being registered.

2.5 High voltage switching

Some of the measurements described in following sections involved the rapid switching of high voltages, normally from either a high negative or positive voltage to ground, or vice versa depending on the application, for example, when maximizing a quadrupole guide efficiency (as described in chapter 6) switching from ground to a large voltage may be necessary, whereas when producing $2\,^3S_1$ states (as de-

scribed in section 4.2) it is necessary to switch from large voltages to ground. This was achieved by using solid state high-voltage switches. For most of these measurements we used used a Behlke GHTS 60. These allowed us to change between two voltages (adding up to 6 kV) with instantaneous currents of $\sim$ 15 A, meaning that we could switch such voltages in approximately 40 - 60 ns depending on the capacitance of the complete Resistor-Capacitor (RC) circuit. It is worth noting that failure to adhere to the maximum instantaneous current specification of 15 A can result in the high voltage switches being permanently damaged. In order to minimize this risk, one may add a resistive load (simply a resistor in series between the switch and the electrode being pulsed) which will change the decay constant of the RC circuit, and increase the switching time, thus reducing the maximum instantaneous current. For some experiments where switching time could be of the order of $\sim$200 ns, such precaution was taken to prevent damage.

We could measure the voltage being applied to electrodes by splitting the high-voltage switch output in a tee between a high-impedance (1 MΩ) oscilloscope and the electrode begin pulsed. The case where the grid and the target electrode voltages are being pulsed is shown in Figure 2.24(a) and the corresponding electric field (b) when the voltage applied to the grid and target electrodes is switched off simultaneously (see figure 2.7).

It should be noted that even though there is a small increase in switching speeds when turning off larger voltages, the main difference arises when switching the same voltage on different electrodes, such as the grid and target electrode. This is due to the target electrode possessing a larger capacitance than the grid electrode. It can be seen in figure 2.24, that if both voltages start off at the same value, and thus the electric field $\vec{E}$ is zero [blue and red line in (a), resulting in orange line in (b)], and they are then subsequently turned off by identical switches, the different switching time for each electrode will generate a non-zero field. This effect can be minimized by independently switching each electrode at different times to account for this delay, however, we found that for the relevant experiments experiments (discussed in section 4.2) this was unnecessary and therefore for most measure-

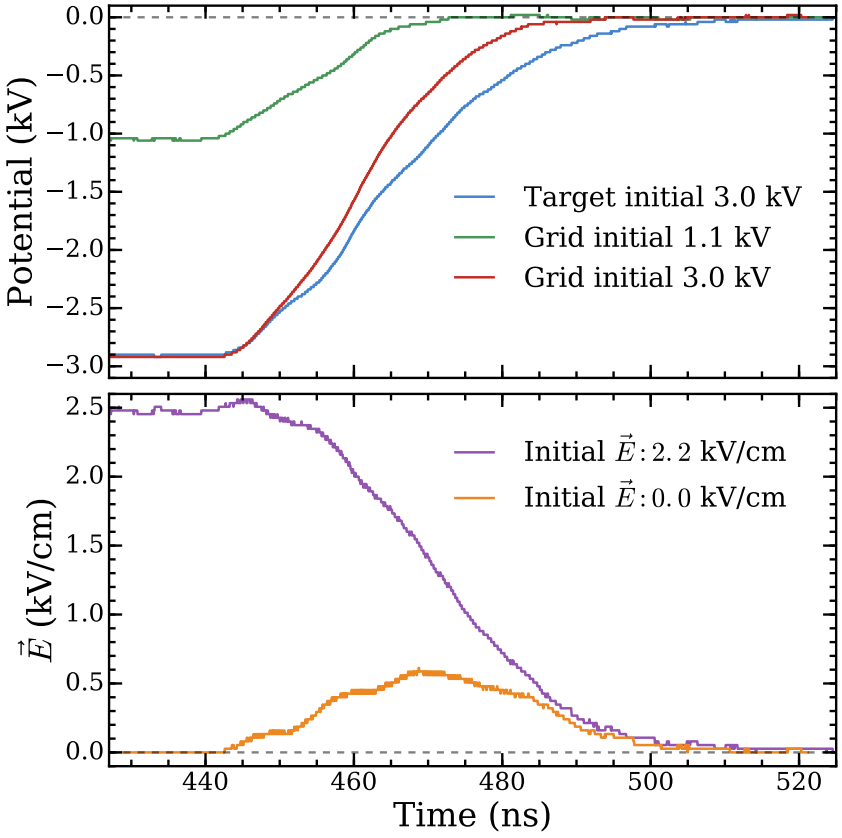

Figure 2.24: (a) Time-dependence of the electric potentials on the grid and target electrodes as they are switched off by a high voltage switch. (b) Electric field in the Ps excitation region, generated by switching off the target and grid electrode potentials.

ments the target and grid biases were switched off simultaneously, such as those described in section 4.2 [Alonso *et al.* 2017b]. This switching technique was also used for switching large biases on quadrupole electrode structures used for Ps Rydberg guiding [Deller *et al.* 2016a, Alonso *et al.* 2017a] as described in chapter 6.

Chapter 3

Theoretical background

Description of the theoretical background outlined in this chapter have been previously published in several articles, and as such, much of the content and figures used here were taken from these publications. Contents from section 3.1 describing the calculations performed to understand the Stark and Zeeman effects on $n = 2$ positronium were published in the following articles:

- A. M. Alonso, B. S. Cooper, A. Deller, S. D. Hogan and D. B. Cassidy. *Controlling Positronium Annihilation with Electric Fields* Phys. Rev. Lett., **15**, 183401 (2015). doi: 10.1103/PhysRevLett.115.183401.

- A. M. Alonso, B. S. Cooper, A. Deller, S. D. Hogan and D. B. Cassidy. *Positronium decay from $n = 2$ states in electric and magnetic fields* Phys. Rev. A, **93**, 012506 (2016). doi: 10.1103/PhysRevA.93.012506.

While contents from Section 3.2 describing the theoretical background needed to understand the basic principles of Rydberg-Stark states were published in:

- A. M. Alonso, B. S. Cooper, A. Deller, L. Gurung and D. B. Cassidy. *Velocity selection of Rydberg positronium using a curved electrostatic guide*. NIMA, **95**, 053409 (2017). doi: 10.1103/PhysRevA.95.053409.

3.1 Stark and Zeeman effects in $n = 2$

To quantify the effect that the electric and magnetic fields in the experiments had in the rates of Ps annihilation, the combined Stark and Zeeman effects for states with $n = 2$ were calculated. These calculations treated all singlet and triplet terms, and their associated fine structure, and were performed by determining the eigenvalues and eigenvectors of the complete Hamiltonian matrix in an $|nS\ell JM_J\rangle$ basis, following the convention of Bethe and Salpeter [Bethe & Salpeter 1957]. Here n is the principal quantum number, S is the total spin quantum number of the electron-positron pair, ℓ is the single particle orbital angular momentum quantum number, $J = |\vec{J}| = |\vec{\ell} + \vec{S}|$ is the total angular momentum quantum number, and M_J is the projection of $\vec{J}$ onto the z-axis with which the applied electric and magnetic fields are aligned. The approach used in these calculations is similar to that implemented previously by Curry [Curry 1973], and Dermer and Weisheit [Dermer & Weisheit 1989].

In the $n = 1$ ground-state of Ps, the energy interval between the singlet and triplet terms is $E_{\rm hfs}(n = 1)/h = 203.3942$ GHz [Kniehl & Penin 2000, Melnikov & Yelkhovsky 2001, Hill 2001, Ishida *et al.* 2014] (see figure 1.1). Because the magnitude of the spin-spin interactions depends on the overlap of the electron and positron wavefunctions, for values of $n > 1$ the energy splittings reduce, scaling with n^{-3} [Gallagher 1994]. For $n = 2$, the energy intervals between the singlet and triplet terms and the fine-structure splittings between each $2\,^3\mathrm{P}_J$ level are indicated in figure 1.1.

3.1.1 Calculation methods

In the presence of parallel electric and magnetic fields, the Hamiltonian, $\hat{H}$, for Ps atoms can be expressed in the form

$$\hat{H} = \hat{H}_0 + \hat{H}_{\rm Z} + \hat{H}_{\rm S}, \tag{3.1}$$

where $\hat{H}_0$ represents the unperturbed Hamiltonian including the fine-structure contributions; $\hat{H}_{\rm Z} = -\vec{\mu}_{\rm mag} \cdot \vec{B}$ is the Zeeman Hamiltonian arsising from the presence

of a magnetic field $\vec{B}$, where $\vec{\mu}_{\rm mag} = \vec{\mu}_{\rm e^-} + \vec{\mu}_{\rm e^+}$ is the combined magnetic moment of the electron-positron pair; and $\hat{H}_{\rm S} = -e\vec{F}\cdot\vec{r}$ is the Stark Hamiltonian resulting from the interaction with an external electric field $\vec{F}$, where e is the electron charge and $\vec{r}$ is the position vector.

To express $\hat{H}$ in matrix form for levels with $n = 2$, we consider the $|nS\ell JM_J\rangle$ basis which gives rise to a 16×16 matrix. Because of the comparatively weak fields used in the experiments, only $n = 2$ levels need be considered in this basis (since there will be no overlap with the neighboring $n = 1$ and $n = 3$ states). The 16 basis states therefore represent the individual M_J sublevels associated with each level in the upper part of figure 1.1. In this basis, $\hat{H}_0$ is a diagonal matrix and the energies of the diagonal elements are those in figure 1.1.

For a magnetic field $\vec{B} = (0,0,B)$ acting in the z-direction, the Zeeman Hamiltonian takes the form

$$\hat{H}_{\rm Z} \;=\; g_{\rm e}\mu_{\rm B}\hat{s}_{z_{e^-}}B - g_{\rm e}\mu_{\rm B}\hat{s}_{z_{e^+}}B, \tag{3.2}$$

where $\hat{s}_{z_{e^-}}$ ($\hat{s}_{z_{e^+}}$) is the projection operator of the electron (positron) spin onto the z-axis, $g_{\rm e}$ is the electron ($\equiv$ positron) spin g-factor, and $\mu_{\rm B}$ is the Bohr magneton. Because of the equal masses of the electron and the positron, the magnetic moment associated with the net orbital angular momentum in Ps is zero. Therefore the Zeeman interaction is independent of $\vec{\ell}$ [Curry 1973]. The matrix corresponding to equation 3.2 contains off-diagonal elements coupling sublevels with equal values of ℓ and M_J, and values of S that differ by ±1, i.e., the magnetic field couples singlet and triplet terms. The matrix elements between sublevels $|nS\ell JM_J\rangle$ and $|nS'\ell'J'M'_J\rangle$ can be expressed [Dermer & Weisheit 1989] as:

$$\langle nS'\ell'J'M'_J|\hat{H}_{\rm Z}|nS\ell JM_J\rangle = \mu_{\rm B}B\,\delta_{\ell',\ell}(-1)^{\ell+M_J}[(-1)^{S+S'}-1]\sqrt{3(2J'+1)(2J+1)} \times \begin{pmatrix} J' & 1 & J \\ -M'_J & 0 & M_J \end{pmatrix} \begin{Bmatrix} S' & \ell' & J' \\ J & 1 & S \end{Bmatrix}, \tag{3.3}$$

where $\delta_{x,x'}$ is the Dirac delta function, and the term in curved (curly) brackets is a

Wigner 3J (6J) symbol.

In an electric field $\vec{F} = (0,0,F)$ aligned parallel to the magnetic field, the Stark Hamiltonian contains off-diagonal elements coupling sublevels with equal values of S and M_J, and values of ℓ that differ by ± 1. The matrix elements between pairs of sublevels take the form [Dermer & Weisheit 1989]

$$\begin{aligned}\langle nS'\ell'J'M'_J|\hat{H}_S|nS\ell JM_J\rangle &= eF\,\delta_{S',S}(-1)^{S+1+M'_J}\sqrt{\ell_{\max}(2J'+1)(2J+1)} \\ &\times \begin{pmatrix} J' & 1 & J \\ -M'_J & 0 & M_J \end{pmatrix} \begin{Bmatrix} S' & \ell' & J' \\ 1 & J & \ell \end{Bmatrix} \langle n'\ell'|r|n\ell\rangle, \end{aligned} \quad (3.4)$$

where $\ell_{\max} = \max(\ell',\ell)$, and $\langle n'\ell'|r|n\ell\rangle$ is a radial integral. For $n = 2$ and $|\ell' - \ell| = 1$, $|\langle n'\ell'|r|n\ell\rangle| = 3\sqrt{3}a_{\rm Ps}$, where $a_{\rm Ps} = 2a_0$ is the Ps Bohr radius.

Combining the Zeeman and Stark matrices with the diagonal zero-field matrix allows the $n = 2$ energy level structure to be determined in parallel fields of all magnitudes relevant to the experiments. This is achieved by calculating the set of eigenvalues, E_i, labelled with the index i, of the complete Hamiltonian matrix for each field strength of interest. Spectral intensities and decay rates can then be obtained from the coefficients, $C_{i,j}$, of the corresponding eigenvectors, where j is an index denoting each $|nS\ell JM_J\rangle$ basis state.

Under the electric dipole selection rules, optical transitions from the $1\,^3S_1$ and $1\,^1S_0$ levels of the ground-state, to excited $n = 2$ states only occur if $\Delta S = 0$, $\Delta\ell = \pm 1$ and $\Delta J = 0, \pm 1$ ($0 \nleftrightarrow 0$) [Bethe & Salpeter 1957]. In photoexcitation the values of M_J of the excited sublevels can be controlled by adjusting the polarisation of the laser radiation with respect to the electric and magnetic fields. For laser radiation propagating perpendicular to both fields, if it is linearly polarized parallel to the axis defined by the fields (z-axis) $\Delta M_J = 0$ transitions will result [see, e.g., figure 3.1(a)], while if it is linearly polarized perpendicular to this axis $\Delta M_J = \pm 1$ transitions will result [see, e.g., figure 3.1(b)]. The resulting transitions between states $|nS\ell JM_J\rangle$

and $|n'S'\ell'J'M'_J\rangle$ have transition dipole moments, $M_{n'S'\ell'J'M'_J,nS\ell JM_J}$, such that

$$M_{n'S'\ell'J'M'_J,nS\ell JM_J} = (-1)^{J-M_J}\sqrt{(2J+1)(2J'+1)} \times \begin{pmatrix} J & 1 & J' \\ -M_J & \Delta M_J & M'_J \end{pmatrix} \times \begin{Bmatrix} \ell & J & S' \\ J' & \ell' & 1 \end{Bmatrix} \langle 2\ell'|er|1s\rangle. \quad (3.5)$$

3.1.2 Calculated $n = 2$ energy-level structure

A Stark energy level diagram, calculated for the $n = 2$ states of Ps in electric fields up to 3 kV/cm when $B = 0$ G, is displayed in figure 3.2(a). In fields below 1 kV/cm in this figure, the S and P terms of each spin multiplicity exhibit quadratic Stark energy shifts as they gradually mix with each other. In higher fields, linear Stark shifts dominate when the interaction with the electric field becomes greater than the spin-spin and spin-orbit interactions. The effect of a small magnetic field oriented parallel to the electric field on the $n = 2$ Stark energy-level structure can be seen in figure 3.2(b).

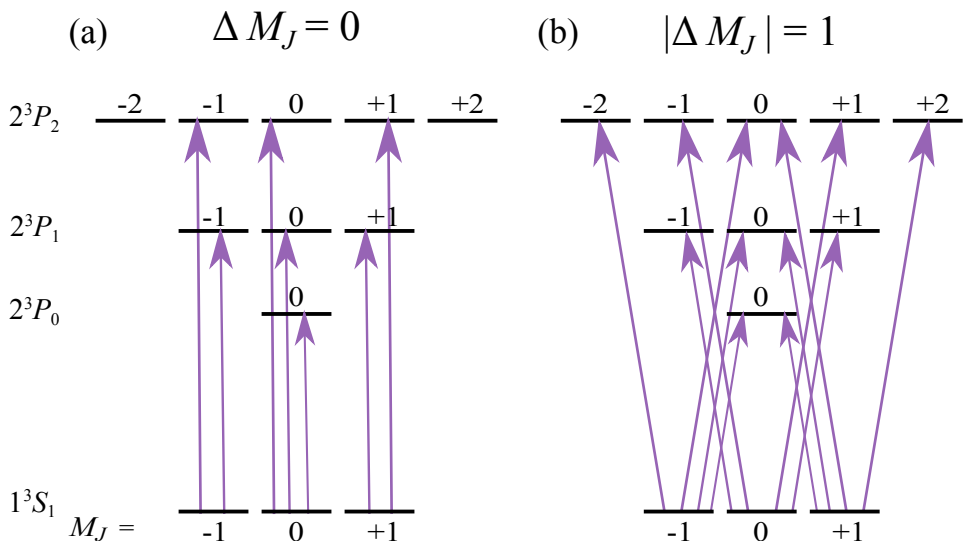

Figure 3.1: Allowed electric dipole transitions from each 1^3S_1 sublevel of Ps to all 2^3P_J sublevels, for laser radiation linearly polarized (a) parallel ($\Delta M_J = 0$), and (b) perpendicular ($|\Delta M_J| = 1$) to the laboratory-fixed quantization axis. From [Alonso *et al.* 2016b].

Comparing figure 3.2(a) and (b) shows that the weak magnetic field of 130 G does not significantly affect the overall Stark structure.

3.1.3 Excited-state decay rates

To obtain more detailed information on the rates of decay of the excited $n = 2$ eigenstates in the presence of the combined electric and magnetic fields, the fluorescence and annihilation rates of Ps atoms initially prepared in the $1\,^3\mathrm{S}_1$ level and subsequently photoexcited via electric dipole allowed $1\,^3\mathrm{S}_1 \rightarrow 2\,^3\mathrm{P}_J$ single-photon transitions were calculated. This was done by first determining the rates for fluorescence, Γ_{fl}, and direct annihilation, Γ_{ann}, of each $n = 2$ sublevel in the presence of the fields, using the data in table 1.1, together with the coefficients of the eigenvectors,

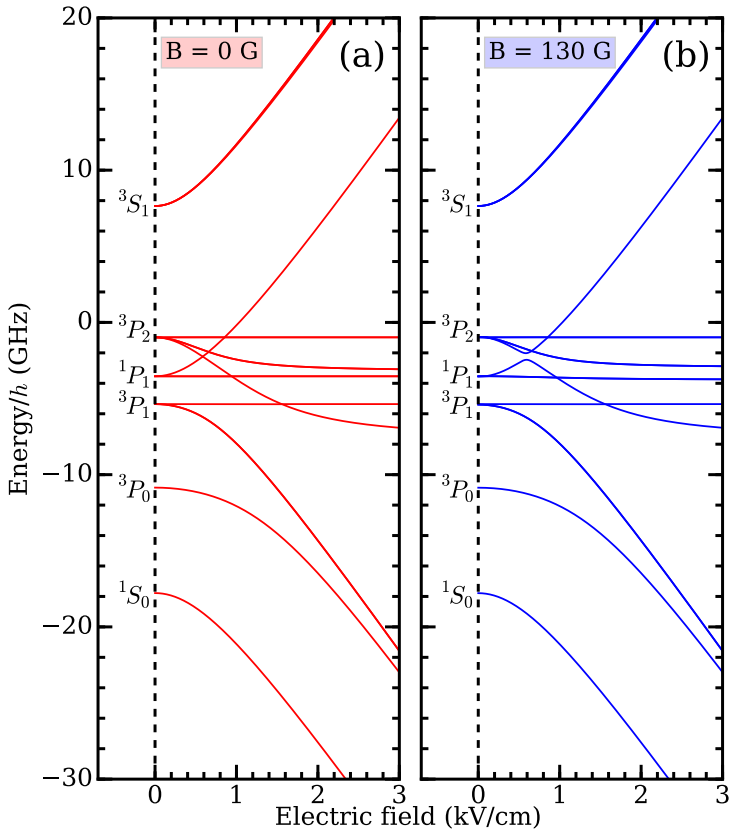

Figure 3.2: Dependence of the relative energies of all $n = 2$ eigenstates in Ps on electric field strength (a) in the absence of a magnetic field, and (b) in a parallel magnetic field of $B = 130$ G. From [Alonso *et al.* 2016b].

$C_{i,j}$, of the Hamiltonian matrix, such that

$$\Gamma_{\mathrm{fl},i} = \sum_j C_{i,j}^2 \Gamma_{\mathrm{fl},j} \tag{3.6}$$

and

$$\Gamma_{\mathrm{ann},i} = \sum_j C_{i,j}^2 \Gamma_{\mathrm{ann},j}. \tag{3.7}$$

Following this procedure the total lifetime $\tau_{\mathrm{tot},i}$, of each eigenstate could be determined,

$$\tau_{\mathrm{tot},i} = (\Gamma_{\mathrm{fl},i} + \Gamma_{\mathrm{ann},i})^{-1}. \tag{3.8}$$

These calculated excited-state lifetimes are displayed in figure 3.3(a) and (b), for cases in which $B = 0$ G and $B = 130$ G, respectively. From these data it can be seen in both cases that, as the strength of the electric field increases, mixing of the S and P terms leads to a reduction in the total lifetimes of the Stark states that adiabatically evolve, from high to low electric field, to the 2^3S_1 level. The lifetimes of these states reduce from 1 μs when $F = 0$ V/cm, to < 10 ns when $F \gtrsim 1$ kV/cm. On the other hand, the lifetime of the short-lived 2^1S_0 level, which decays predominantly by direct annihilation, increases slightly with increasing electric field.

In the presence of an electric field, the lifetimes of the 2P states evolve in three ways: (1) The total lifetimes of the 2^3P_J levels that mix with the 2^3S_1 level increase; (2) levels which remain unmixed in the field, i.e., those for which $|M_J| = 2$, maintain their field free 3.19 ns lifetime; and (3) the lifetimes of the levels that mix with the 2^1S_0 level [e.g., the 2^1P_1 ($M_J = 0$)], are reduced, in this case from 3.19 ns when $F = 0$ V/cm to ~ 2 ns when $F = 3$ kV/cm.

The effect of singlet-triplet mixing, induced by the presence of the magnetic field of $B = 130$ G, on the lifetimes of each of the Stark eigenstates can be seen in figure 3.3(b). The principal difference between this case and that in figure 3.3(a) is seen close to $F = 585$ V/cm, the field at which the avoided crossing in figure 3.2(b)

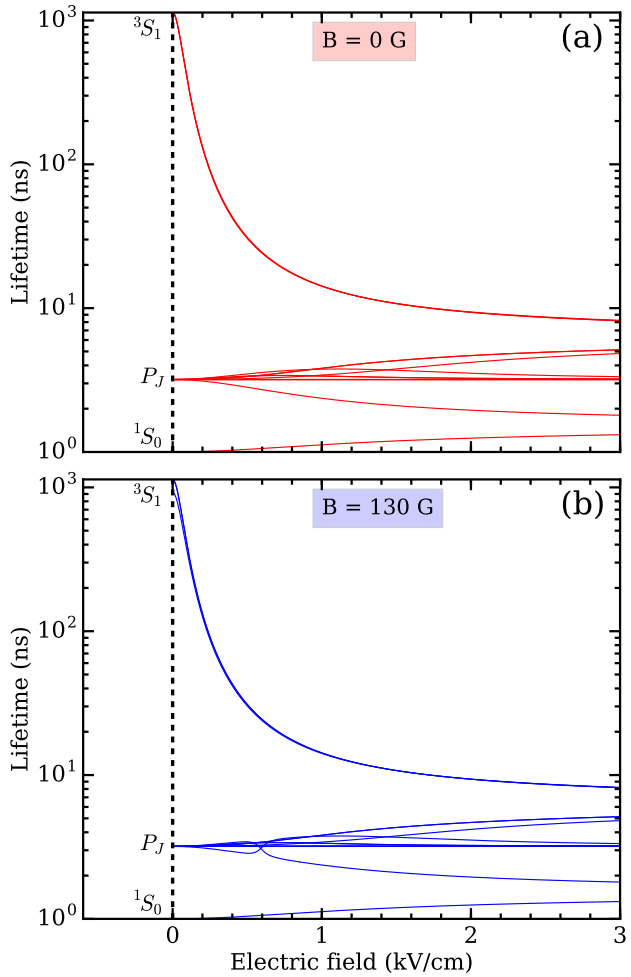

Figure 3.3: Dependence of the combined fluorescence and annihilation lifetimes of the $n = 2$ eigenstates in Ps on electric field strength for (a) $B = 0$ G, and (b) $B = 130$ G. The term symbols associated with the field-free eigenstates are indicated on the left side of each panel. From [Alonso *et al.* 2016b].

occurs. In this field, the slightly reduced lifetime of the $2\,^1\mathrm{P}_1(M_J = 0)$ sublevel that arises when it mixes with the $2\,^1\mathrm{S}_0$ level in the electric field, causes a subsequent reduction in the lifetime of the $2\,^3\mathrm{P}_2(M_J = 0)$ sublevel with which it interacts when the magnetic field is present.

The experiments described in later sections all involved exciting ensembles of Ps atoms, initially in the $1\,^3\mathrm{S}_1$ level, via single-photon transitions to $n = 2$ eigenstates with $^3\mathrm{P}_J$ character. As a result, the excited state lifetimes of importance are those of the states which are accessible via this photoexcitation scheme. The lifetimes of these states can be identified in figure 3.4. The electric field dependence of

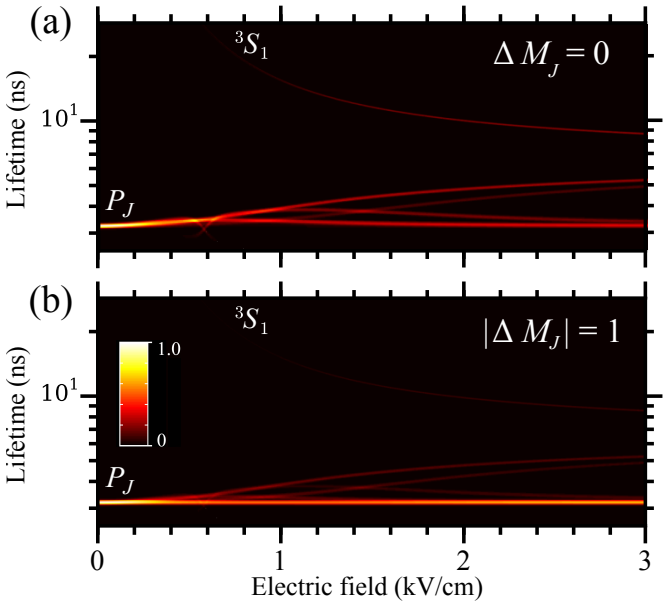

Figure 3.4: The electric field dependence of the total lifetimes (in the range from 2.5 ns to 25 ns) of the $n = 2$ eigenstates accessible by single-photon excitation from the $1\,^3S_1$ level when $B = 130$ G [as in Figure 3.3(b)]. The color scale represents the relative strength of the electric dipole transitions for laser radiation linearly polarised (a) parallel ($\Delta M_J = 0$), and (b) perpendicular ($|\Delta M_J| = 1$) to the z-axis with which the electric and magnetic fields are aligned. From [Alonso *et al.* 2016b].

the lifetimes of the $n = 2$ eigenstates included in this figure are identical to those in figure 3.3(b), while the color scale represents the relative $1\,^3S_1 \rightarrow 2\,^3P_J$ transition dipole moment to each state, calculated using equation 3.5. From this data it can be seen that for $\Delta M_J = 0$ transitions, driven with laser radiation polarized parallel to the axis defined by the electric and magnetic fields [figure 3.4(a)], a slight reduction in the total lifetime of some of the accessible $n = 2$ eigenstates from their field-free values of 3.19 ns occurs in an electric field of 585 V/cm, as a result of mixing with states possessing $2\,^1S_0$ components. However, in higher fields, transitions to longer-lived states with partial $2\,^3S_1$ character also play an important role. For $|\Delta M_J| = 1$ transitions, driven with laser radiation polarized perpendicular to the fields, only a very slight change in the direct $n = 2$ decay rates occurs in weak electric fields, while in strong fields the accessible sublevels to which the strongest transitions occur do not exhibit lifetimes significantly longer than those of the field-free levels.

The dependence of the total lifetimes of the $n = 2$ eigenstates on the electric

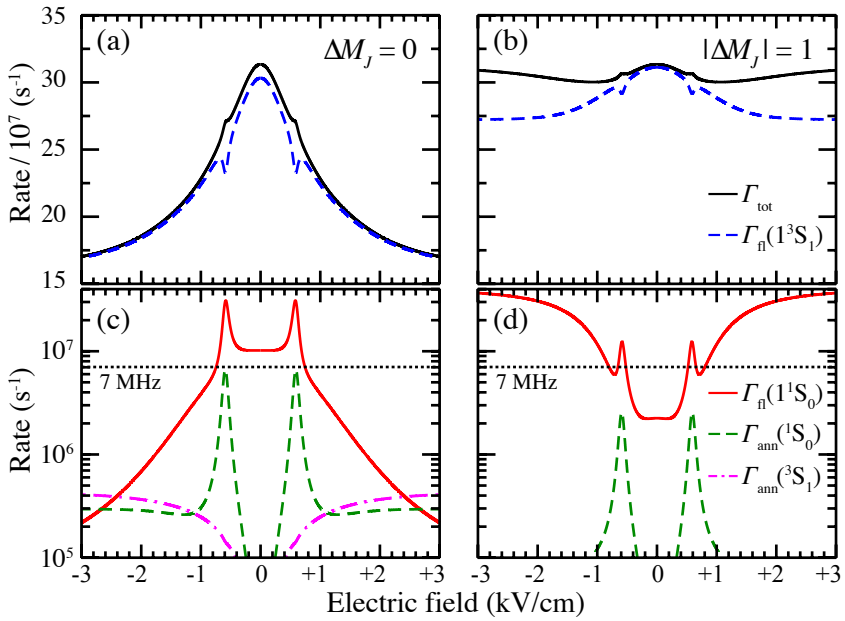

Figure 3.5: Spectral-intensity–weighted average $n = 2$ decay rates when $B = 130$ G for photoexcitation via (a) and (c) $\Delta M_J = 0$, and (b) and (d) $|\Delta M_J| = 1$ transitions from the 1^3S_1 level. (a) and (b), total $n = 2$ decay rates, Γ_{tot}, (continuous black curve), and triplet fluorescence rate, $\Gamma_{fl}(1^3S_1)$, (dashed blue curve). (c) and (d), fluorescence rate to the 1^1S_0 level, $\Gamma_{fl}(1^1S_0)$, (continuous red curve), and direct 2^1S_0, $\Gamma_{ann}(^1S_0)$, (dashed green curve) and 2^3S_1, $\Gamma_{ann}(^3S_1)$, (dash-dotted magenta curve) annihilation rates. The horizontal dashed lines in (c) and (d) corresponds to the 7 MHz annihilation rate of the 1^3S_1 level. From [Alonso *et al.* 2015].

and magnetic fields displayed in figure 3.3 and figure 3.4 does not, however, provide a complete picture of Ps annihilation in experiments where there was only $n = 2$ excitation. The dominant contribution to this results from spontaneous emission from excited states with 2^1P_1 character to the 1^1S_0 level, which rapidly self-annihilates. To identify the role of this process and its significance when compared to the other possible Ps decay pathways, spectral-intensity–weighted average decay rates were determined for a range of electric fields typically used in the experiments. These average decay rates, presented in figure 3.5, were calculated by assuming an equal laser intensity across the frequency range encompassed by the manifold of $n = 2$ levels in the presence of the fields. Displayed in figure 3.5(a) and (b) are weighted-average total decay rates calculated for each laser polarisation from the values of $\Gamma_{fl,i}$ and $\Gamma_{ann,i}$ (see equation 3.6 and equation 3.7), and the squares of the corre-

sponding transition dipole moments, $M_{i,nS\ell JM_J}$, where

$$M_{i,nS\ell JM_J} = \sum_j C_{i,j}^2 M_{j,nS\ell JM_J}, \tag{3.9}$$

and $|nS\ell JM_J\rangle$ are the sublevels of the $1\,^3S_1$ ground state. By comparison with the weighted-average values of the fluorescence rate to the $1\,^3S_1$ level, $\Gamma_{\rm fl}(1\,^3S_1)$, also included in these figures, these data indicate that for both laser polarizations the decay of the accessible excited states is dominated, in all electric fields considered, by the contribution from fluorescence via this decay pathway. However, as can be seen in figure 3.5(c) and (d), for particular combinations of electric field strength and laser polarisation, decay by fluorescence to the $1\,^1S_0$ is also of importance. This is particularly apparent in a field of 585 V/cm and in fields exceeding 1 kV/cm when the laser polarisation is selected to drive $\Delta M_J = \pm 1$ transitions.

3.2 Rydberg-Stark states

In hydrogenic atoms, states with the same n but different ℓ values are degenerate in the absence of external fields. Consequently, even very weak electric or magnetic fields, both of which are invariably present in our experiments, can lead to complete ℓ mixing within an n manifold [Merkt & Zare 1994]. In these conditions it is often more convenient to consider the atomic structure in terms of hydrogenic Stark states. If the Schrödinger equation is solved in parabolic coordinates the resulting eigenstates are labeled according to their parabolic quantum numbers n_1 and n_2, and the Stark states may then be characterized using the index $k = n_1 - n_2$ [Gallagher 1994], thus each Stark state may be characterized in the $|n, n_1, n_2, m\rangle$ basis, where $n = n_1 + n_2 + |m| + 1$. For each value of n and the azimuthal quantum number m, the allowed values of k range from $-(n - |m| - 1)$ to $+(n - |m| - 1)$ in intervals of 2.

In an electric field $\vec{F} = (0, 0, F_z)$, the energy shifts of these Stark states can be

expressed analytically to fourth order as [Damburg & Kolosov 1983, Hogan 2013]

$$\begin{aligned} E_{\text{Stark}} &= \frac{3}{2}nkea_{Ps}F_z - \frac{1}{16}n^4(17n^2-3k^2-9m^2+19)\frac{e^2a_{Ps}^2}{2hcR_{Ps}}F_z^2\ldots \\ &+\frac{3}{32}n^7k[23n^2-k^2+11m^2+39]\frac{e^3a_{Ps}^3}{(2hcR_{Ps})^2}F_z^3\ldots \\ &-\frac{1}{1024}n^{10}[5487n^4+35182n^2-1134m^2k^2+1806n^2k^2-3402n^2m^2\ldots \\ &+147k^4-549m^4+5754k^2-8622m^2+16211]\frac{e^4a_{Ps}^4}{(2hcR_{Ps})^3}F_z^4 \end{aligned} \tag{3.10}$$

where e is the charge of the electron, and a_{Ps} and R_{Ps} are the Bohr radius and Rydberg constant corrected for the reduced mass of Ps, respectively. Stark shifts for $n = 14$ Ps atoms with $m = 1$, calculated using this expression, are shown in

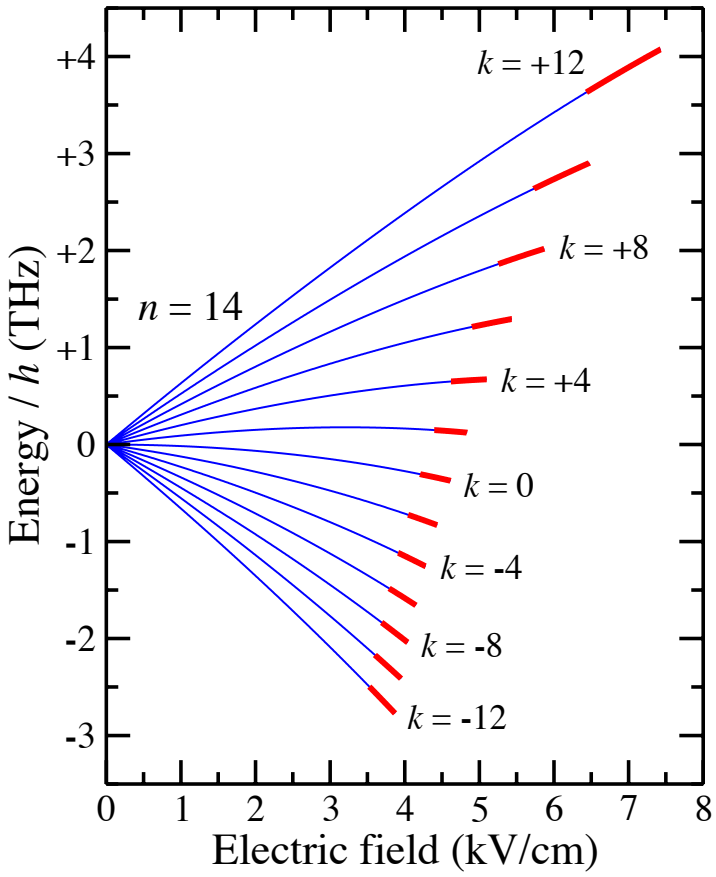

Figure 3.6: Stark structure at $n = 14$ in Ps. Each Stark state, labeled with the index k (see text for details), is displayed for fields in which the ionization rate is $< 10^{10}$ s. The thicker sections of each curve indicate the fields for which the ionization rate ranges from 10^8 s^{-1} to 10^{10} s^{-1}. From [Alonso *et al.* 2017a].

figure 3.6.

Since the energy shift of an electric dipole in an electric field $\vec{F}$ is [Griffiths 2012]

$$E_{\text{Stark}} = -\vec{\mu}_{\text{elec}} \cdot \vec{F}, \tag{3.11}$$

comparison with equation 3.10 indicates that, to first order, an electric dipole moment, $\vec{\mu}_{\text{elec}}$, can be associated with each Rydberg-Stark state such that [Gallagher 1994],

$$\vec{\mu}_{\text{elec}} = -\frac{3}{2} nk\, e\, a_{\text{Ps}}. \tag{3.12}$$

These large static electric dipole moments allow forces to be exerted on atoms in these states using inhomogeneous electric fields [Hogan 2016]. In a spatially inhomogeneous electric field the resulting force is

$$\vec{f} = \nabla(\vec{\mu}_{\text{elec}} \cdot \vec{F}). \tag{3.13}$$

The magnitude of this force therefore depends directly on the gradient of the electric field. In exploiting such forces to control the translational motion of Rydberg atoms the greatest accelerations that can be achieved using time-independent electric potentials are limited by field ionization of the Rydberg states. The tunnel ionization rate, $\Gamma_{nn_1n_2m}(F_z)$ for a Rydberg-Stark state in an electric field, is given by [Damburg & Kolosov 1983]

$$\Gamma_{nn_1n_2m}(F_z) = \frac{2hcR_{\text{Ps}}}{\hbar} \frac{(4C)^{2n_2+m+1}}{n^3\, n_2!\, (n_2+m)!} \exp\left[-\frac{2}{3}C - \frac{1}{4}n^3 \frac{e\, a_{\text{Ps}} F_z}{2hcR_{\text{Ps}}} \left(34n_2^2 + 34n_2 m + 46n_2 + 7m^2 + 23m + \frac{53}{3}\right)\right], \tag{3.14}$$

where

$$C = \frac{1}{e\, a_{\text{Ps}} \sqrt{2hcR_{\text{Ps}}}} \frac{(-2E_{nn_1n_2m})^{3/2}}{F_z}, \tag{3.15}$$

and $E_{nn_1n_2m} = -[hcR_{\mathrm{Ps}}/(n^2)] + E_{\mathrm{Stark}}$, is the total energy of the state with respect to the ionization limit, in the presence of the electric field. The Stark map presented in figure 3.6 is displayed for fields up to those in which the ionization rate exceeds 10^{10} s^{-1}. The thicker sections of each curve indicate the fields for which the ionization rate ranges from 10^8 s to 10^{10} s.

Chapter 4

Spectroscopy of $n = 2$ positronium

The experiments and results discussed in this chapter have been previously published in several articles, and as such, much of the content and figures used here were from these publications. Contents from section 4.1 describing the effects of electric and magnetic fields on the annihilation of positronium have been published in the following articles:

- A. M. Alonso, B. S. Cooper, A. Deller, S. D. Hogan and D. B. Cassidy. *Controlling Positronium Annihilation with Electric Fields.* Phys. Rev. Lett., **115**, 183401 (2015). doi: 10.1103/PhysRevLett.115.183401.

- A. M. Alonso, B. S. Cooper, A. Deller, S. D. Hogan and D. B. Cassidy. *Positronium decay from $n = 2$ states in electric and magnetic fields.* Phys. Rev. A, **93**, 012506 (2016). doi: 10.1103/PhysRevA.93.012506.

While contents from section 4.2 describing the production of positronium atoms in the $2\,^3S_1$ state were published in:

- A. M. Alonso, S. D. Hogan and D. B. Cassidy. *Production of $2\,^3S_1$ positronium atoms by single-photon excitation in an electric field*. Phys. Rev. A, **95**, 033408 (2017). doi: 10.1103/PhysRevA.95.033408.

4.1 Stark and Zeeman effects for $n = 2$ positronium

It is essential for our experiments to have a solid understanding of annihilation and decay dynamics of Ps in intermediate excited states, such as $n = 2$. This is important because all of our optical spectroscopy experiments (including manipulation of Rydberg states) start by exciting Ps from the ground state into $n = 2$. When performing similar experiments with other atomic species one needs to have an understanding of the energy level structure of whichever atom is being studied, and the *fluorescence decay* rates of each of these states to lower energy levels, however, when dealing with Ps, it is necessary to be equally mindful of the *annihilation decay* rates, since in some cases these are much higher than the fluorescence decay rates.

Such characteristic self-annihilating nature has many effects that need to be taken into account when studying Ps. Virtual annihilation has a large impact in the energy level structure of Ps [Ferrell 1951], but it is also important to consider real annihilation events for Ps, since these can be measured by detecting the gamma rays emitted by the annihilation of the positron-electron pair.

In the experiments outlined in this section, we used a $1\,^3S_1 \rightarrow 2\,^3P_J$ excitation scheme where we controlled the laser polarization. The degree of polarization was controlled by passing the laser beam through a half-waveplate, which rotates the polarization of the beam, and subsequently passing the beam through a Glan-Taylor beamcube which was able to achieve $> 95\%$ linear polarization purity. Figure 4.1(a) shows the approximate detector placement for the data shown in this section, and (b) displays the target-grid arrangement used to control the electric field in the excitation region. We applied parallel electric and magnetic fields to control the amount of Zeeman and Stark mixing, and thus the admixture of excited states in $n = 2$ with different orbital angular momentum and spin multiplicity. When the electric and magnetic fields were tuned to maximize the amount of $2\,^1P_1$ character of the excited eigenstate, while still maintaining efficient excitation from the $1\,^3S_1$ level, decay to the short-lived $1\,^1S_0$ level could occur, leading to rapid annihilation. Similarly, optical excitation to mixed states with $2\,^1S_0$ character result in direct annihilation from the excited state. Both of these mechanisms allowed us to use this technique as a de-

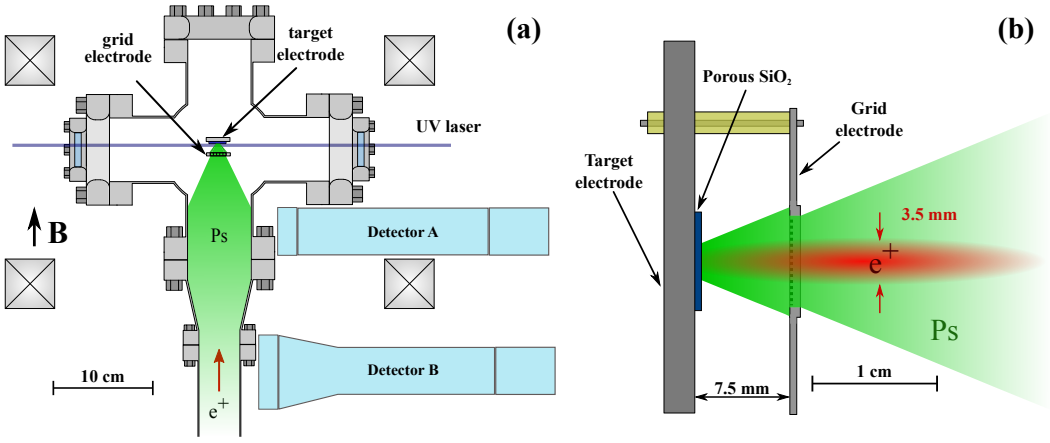

Figure 4.1: Positronium formation and excitation region, showing the positions of the two detectors (a) and the target and grid electrode arrangement (b). The shaded green regions represent the divergent Ps beam profile, as collimated by the grid electrode. From [Alonso *et al.* 2017b].

tection method. Conversely, controlling the fields in such a way as to maximize the amount of $2\,^3S_1$ character in the excited state leads to an increase in the annihilation lifetime; this will be shown in section 4.2.

Following the methods outlined in section 3 the Stark energy level structure can be computed for a range of fields. The experiments outlined in this section were performed in a magnetic field of 130 G (unless stated otherwise). Figure 4.2(a) shows the pure Stark effect on the $n = 2$ manifold, with no Zeeman terms.

The effect caused from adding a relatively-weak parallel magnetic field of 130 G is shown in figure 4.2(b), the change in the overall dependence of the energy levels on the electric field is not very significant. However, there is a particular region of interest when comparing figure 4.2(a) and (b) that allows us to optimize the signal caused by this excitation scheme. When the electric field is 585 V/cm, it can be clearly seen that what was an exact crossing when B $=$ 0 G, becomes an avoided crossing when a magnetic field is applied. This effect is caused by the initial singlet-triplet (Zeeman) mixing between the $2\,^1P_1(M_J = 0)$ and $2\,^3P_2(M_J = 0)$ levels (see section 3.1) which causes the electric field .

This effect can be clearly seen in figure 4.2(c). The eigenstates that would adiabatically evolve to be $2\,^1P_1(M_J = 0)$ and $2\,^3P_2(M_J = 0)$ in zero field, are ap-

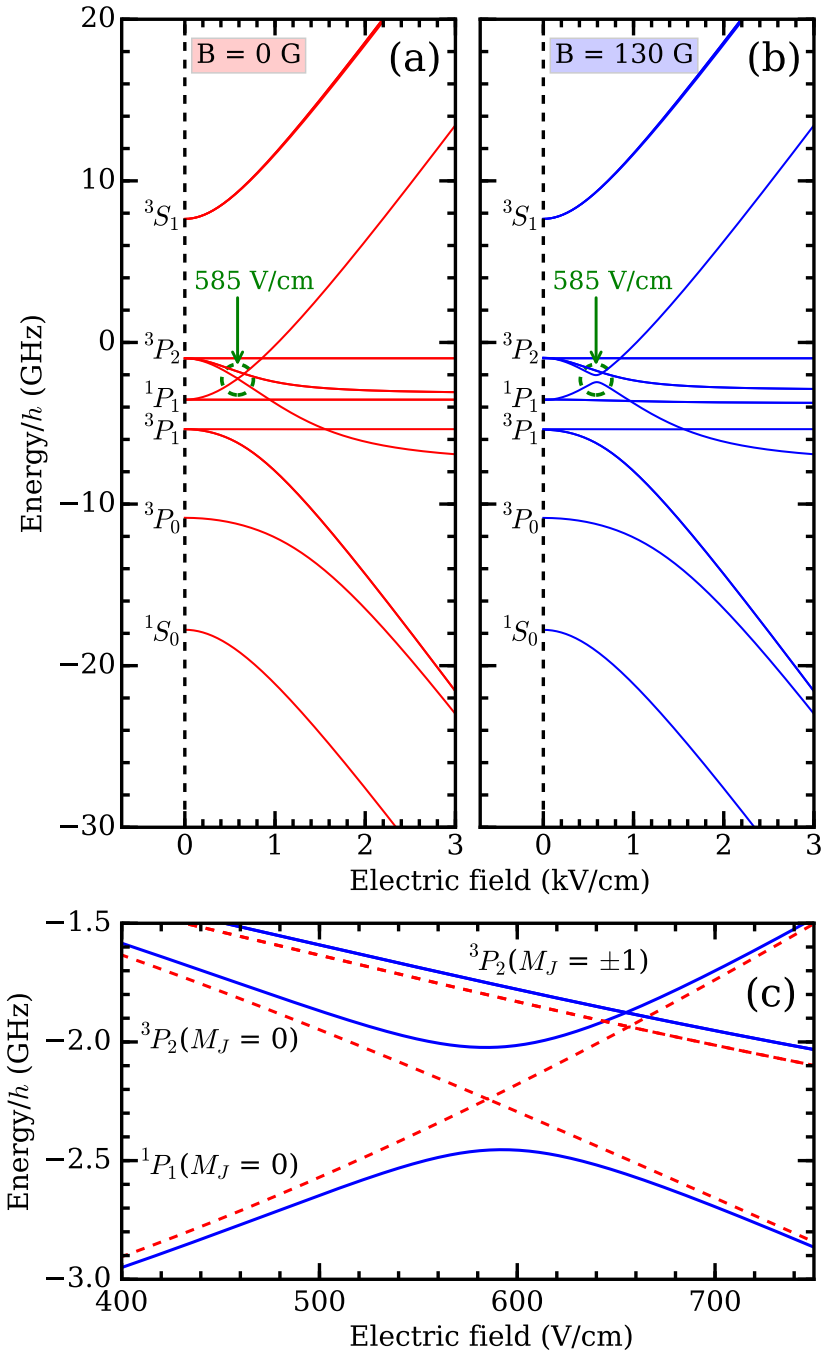

Figure 4.2: Dependence of the relative energies of all $n = 2$ eigenstates in Ps on electric field strength (a) in the absence of a magnetic field, and (b) in a parallel magnetic field of $B = 130$ G. (c) An expanded view of the regions enclosed by the dashed circles in (a) and (b). The results of calculations performed for $B = 0$ G (dashed red curves), and $B = 130$ G (continuous blue curves) are presented. From [Alonso *et al.* 2016b].

proximately 50 % mixed with each other at this electric field, meaning that there is still sufficient triplet ($2\,^3P_2$) character for the excitation to be efficient, but in addition, the significant amount of singlet ($2\,^1P_1$) character makes it possible for the excited state to radiatively decay to the short-lived singlet ground level ($1\,^1S_0$), and self-annihilate almost instantly (125 ps). Therefore, by tuning the fields to this specific configuration in our experiment, we are able to enhance the amount of long-lived triplet Ps atoms that decay into short-lived singlet atoms, thereby generating an identifiable signal via timing techniques (see section 2.3 for SSPALS method). It should be noted that when the electric field is $\sim$ 585V/cm as shown in figure 4.2(c), the effect is maximized, but nevertheless it will still be present at other fields (including 0 V/cm), and so making the electric field $\sim$ 585V/cm is simply an optimization for that given magnetic field (130 G). As discussed and shown in section 4.1.2 this effect can be seen at other electric field values.

4.1.1 Monte Carlo simulation of positronium annihilation

In order to obtain an estimate of the experimentally-measured S_γ parameter (see section 2.3) at different electric fields, a Monte Carlo simulation was performed. As a first step, an initial ensemble of Ps atoms was considered to be in the triplet ground state $1\,^2S_1$ at $t = 0$. During a short period of time allowing for the Ps atoms to diffuse through the porous silica, the ensemble of atoms was allowed to evolve normally, with a lifetime of 142 ns and using Monte Carlo methods to determine the number of atoms that annihilated after each time step of 1 ns. When an atom was selected to undergo annihilation, it was removed from the ensemble. Then the Ps atoms were considered to have escaped the silica target porous network and into the laser excitation region, where a fraction of them were considered to be excited into eigenstates with $2\,^3P_J$ character.

Four different channels were considered for the excited atoms. These are depicted in figure 4.3. (1) Decay by fluorescence to the long-lived $1\,^3S_1$ level, the atoms would then be assigned a lifetime of 142 ns again, and would not be removed from the simulation. (2) Decay by fluorescence to the short-lived $1\,^1S_0$ state, these atoms would then be considered to instantly annihilate (and thus be removed from

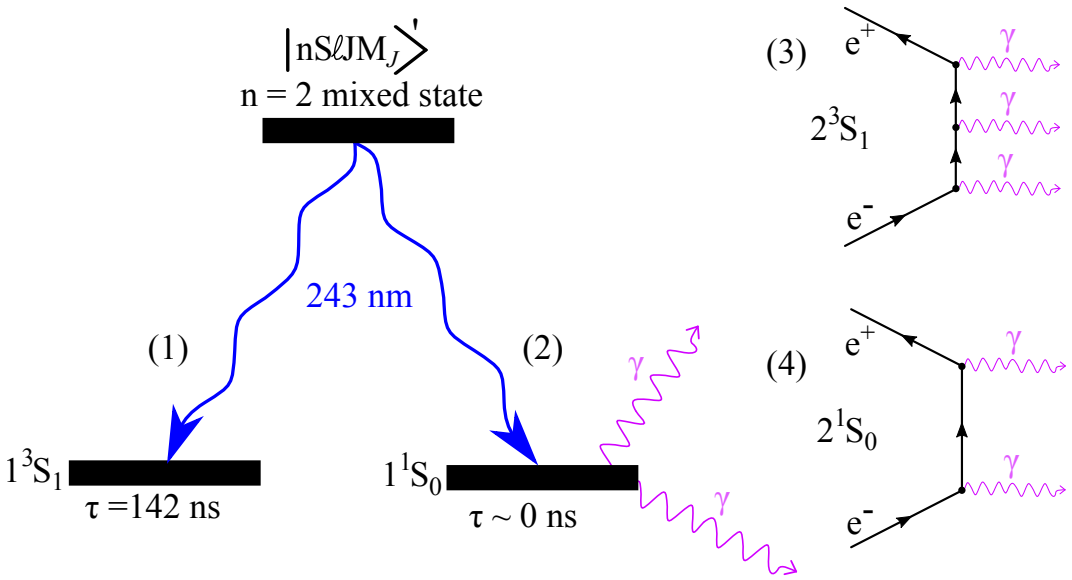

Figure 4.3: Possible decay channels considered in the Monte-Carlo simulation. Only channels 2,3 and 4 contributed towards the gamma ray count, and it was considered that in all three cases the only one of the produced gamma rays was detected.

the simulation), and a gamma-ray would be counted. (3) Direct annihilation from $n = 2$ due to $2\,^3\mathrm{S}_1$ character, and (4) direct annihilation from $n = 2$ due to $2\,^1\mathrm{S}_0$ character, in both of these cases the Ps atoms would be removed from the simulation and a gamma-ray would be counted, this process was repeated each time step until reaching $t \sim 1\ \mu s$. The counted gamma-rays were then convoluted with a detector response of 12 ns (since the data shown in this section was recorded using a PWO detector, see section 2.3). Figure 4.4 shows an example of such decay curve obtained with this method. In this case, the implantation of the positron pulse and the initial formation of p-Ps was not simulated, and instead, the background f value was made to match the experimental value by simply adding an arbitrary value to the total area under the curve, i.e.

$$f_{\text{calc.}} = \frac{\int_B^C V(t)\,dt}{\int_A^C V(t)\,dt + P_{\text{back.}}}, \tag{4.1}$$

where $P_{\text{back.}}$ is the background value being added to account for the "prompt peak". Changing this value accordingly makes the background f in figures 4.5(a) and 4.6(a) match with the experimental background when there is no "grid Ps".

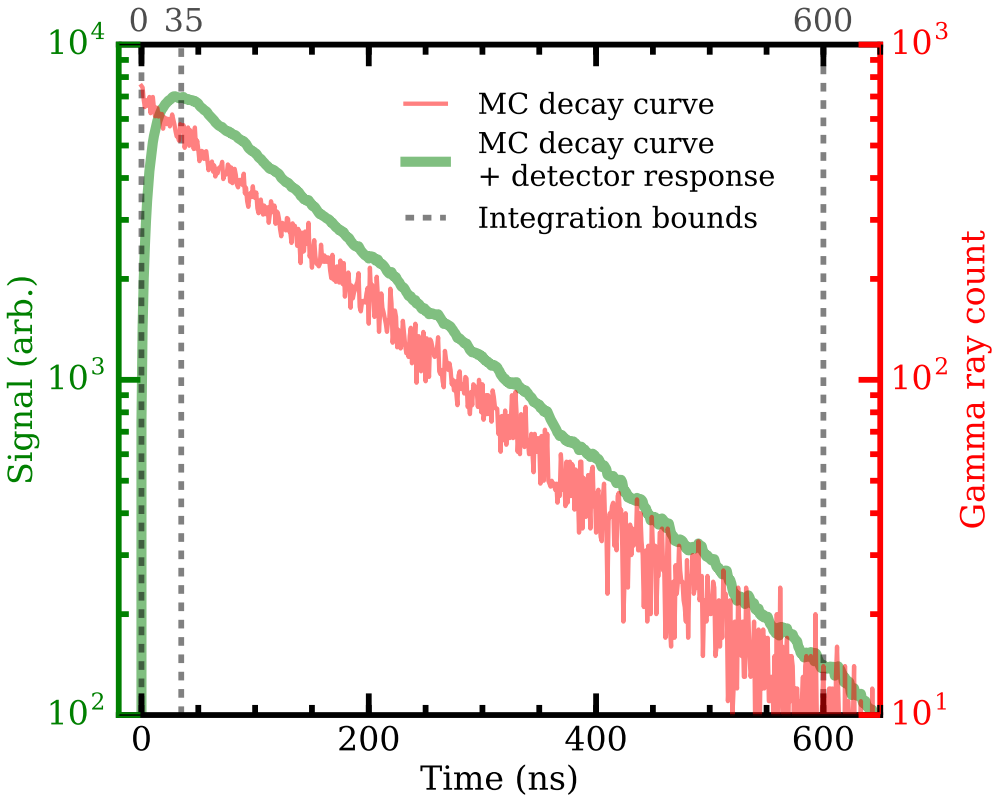

Figure 4.4: Decay curve generated using Monte-Carlo methods described in the text. The red line represents the raw gamma ray count, and the green line is the result after the counts have been convolved with a detector response decay time of 12 ns. The integration bounds used to calculate the f values and S_γ values are shown as vertical lines. The values of f were made to match the experimental background values (as shown in figure 4.5 and 4.6) by adding an arbitrary number to the total area under the curve, this accounts for the gamma rays from direct annihilations when the positron pulse is implanted and for p-Ps formation.

This method allowed for a simulated Ps decay curve to be obtained, and from it values of S_γ could be calculated by integrating the signal in the appropriate time windows (see section 2.3.2).

4.1.2 Electric field dependence

The main result of this section is the controlled mixing of short-lived and long-lived $n = 2$ levels of Ps using magnetic and electric fields. Single-shot lifetime spectra were recorded for different electric fields and with the $1^3S_1 \rightarrow 2^3P_J$ excitation laser having two different polarizations, $\Delta M_J = 0$ and $|\Delta M_J| = 1$. S_γ values were determined for each configuration, the excitation pathways allowed by the two po-

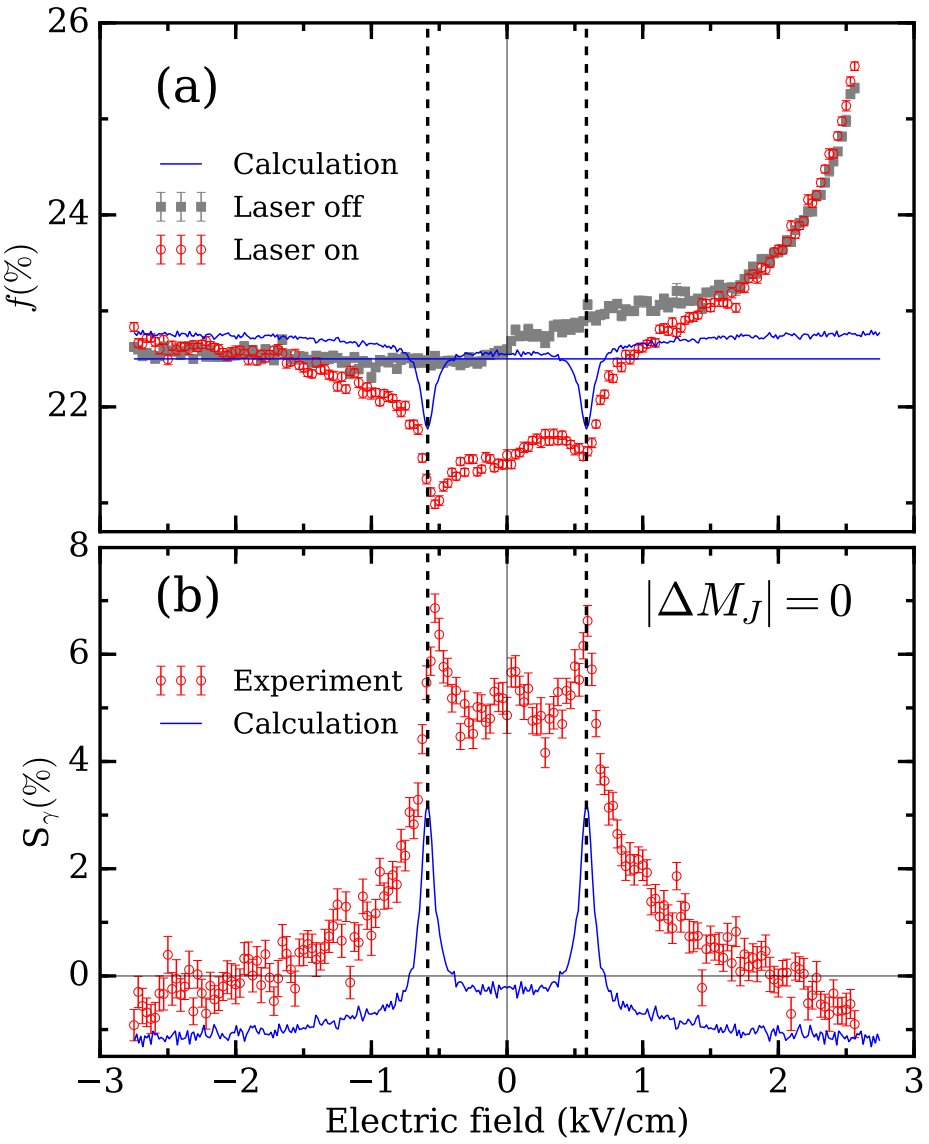

Figure 4.5: (a) Measurements and results of Monte Carlo calculations of the delayed fraction (f) of the annihilation signal with (red circles) and without (gray squares) the laser radiation present as a function of the applied electric field, for laser radiation polarized linearly parallel to the z-axis. (b) Dependence of the measured Ps annihilation signal (S_γ) on the electric field for with a constant magnetic field of ∼130 G. The calculated values of f and S_γ incorporate only experimental parameters and have not been arbitrarily scaled. From [Alonso *et al.* 2015].

larizations are represented by figure 3.1(a) and (b) respectively.

The S_γ values are shown in figure 4.5(b) and 4.6(b), where the structures observed are in qualitative agreement with the calculated effects of the Stark and Zeeman interactions discussed in section 3.1 and their implementation into the simu-

lations described in section 4.1.1. The dependence of the measured and calculated S_γ values on the electric field and laser polarizations are similar, indicating that the underlying physical processes are correctly interpreted. In particular, the peaks at 585 V/cm are clearly due to the mixing between singlet and triplet levels at the avoided crossing [see figure 4.2(c)], and the negative S_γ values correspond to the increased lifetime due to the 2^3S_1 level mixing with the 2^3P_J levels. Note that the positions of the Stark-tuned intensity maxima at 585 V/cm in the experimental data are not exactly symmetric, with the negative-field peak shifted slightly. This may be due to the presence of secondary electrons generated by the positron pulse [Overton & Coleman 1997] or the production of photoelectrons by the UV laser [Hauri *et al.* 2010], which could distort the field in the interaction region.

The calculated f values are scaled by the parameter $P_{\text{arb.}}$ to match the measured background values, though it is worth noting that the formation of "grid Ps" was not included in the simulations, and therefore the background and signal f are symmetric, however, since in the experiment the amount of grid Ps generated is independent of the laser being on or off resonance, when S_γ values are calculated, the effect of such grid Ps is subtracted away, and symmetry is recovered in the experimental data, and maintained in the calculated data. That being said, the calculated S_γ amplitudes should therefore also match. The fact that they do not suggests that there are additional mechanisms that have not been accounted for in the Monte Carlo model. These may be related to optical pumping processes that would excite atoms to states that could be magnetically quenched further, and thus could contribute to the disparity in the magnitude of the S_γ signal compared to the experimental data.

Figure 4.7 shows spectra encompassing the $1^3S_1 \rightarrow 2^3P_J$ transitions that were measured in three different static electric fields ($F = 0$, 585, and 3000 V/cm) with the UV laser radiation polarized linearly parallel to the z-axis ($\Delta M_J = 0$). In the highest of these fields we expect no quenching. Under these conditions photoionization of the 2^3P_J atoms can be used to generate a gamma-ray signal (as can be seen in the green data points in figure 4.7, where controlled Stark mixing is di-

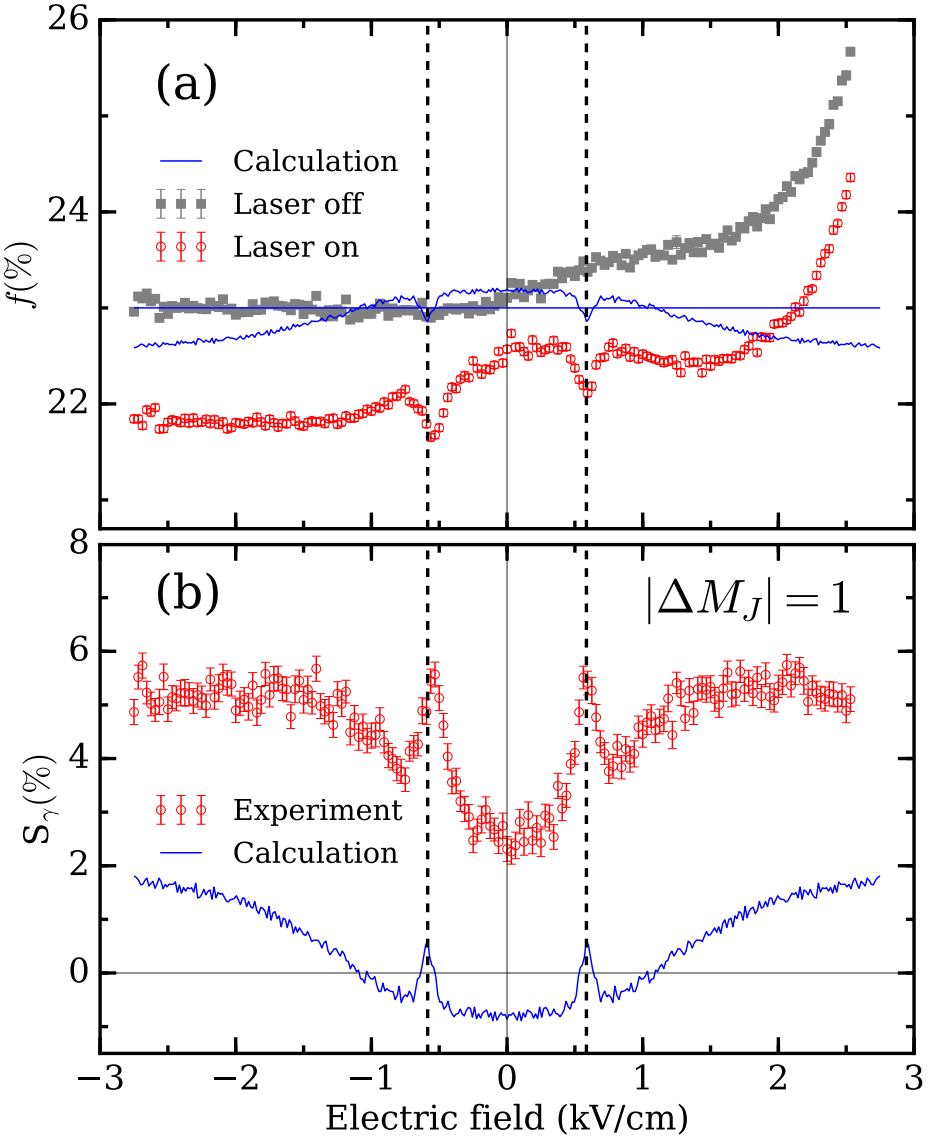

Figure 4.6: (a) Measurements and results of Monte Carlo calculations of the delayed fraction (f) of the annihilation signal with (red circles) and without (gray squares) the laser radiation present as a function of the applied electric field, for laser radiation polarized linearly perpendicular to the z-axis. (b) Dependence of the measured Ps annihilation signal (S_γ) on the electric field for with a constant magnetic field of ∼130 G. The calculated values of f and S_γ incorporate only experimental parameters and have not been arbitrarily scaled. From [Alonso *et al.* 2015].

rectly compared to photoionization using an additional green laser ($\lambda = 532$nm, with fluence of approximately ~ 130 mJ cm^{-2}) to excite Ps from $n = 2$ to beyond the ionization limit). The cross section for this process is approximately 10^6 times lower than that of the $1^3S_1 \rightarrow 2^3P_J$ excitation [Bethe & Salpeter 1957], and for typical experimental conditions pulse energies of ~ 10 mJ per pulse are required [Fee *et al.* 1991]. These high energies may not always be acceptable, for example in a cryogenic system, or if delicate Ps formation targets are used (e.g., [Andersen *et al.* 2015]).

Photoionization can always be made more efficient than magnetic quenching (with or without Stark mixing), since one can saturate the process. However, from a practical point of view, it can be very convenient to optimize an excitation process via magnetic quenching, independently of any subsequent ionization process.

In some cases longer-lived 2^3S_1 components may be mixed with the 2^3P_J

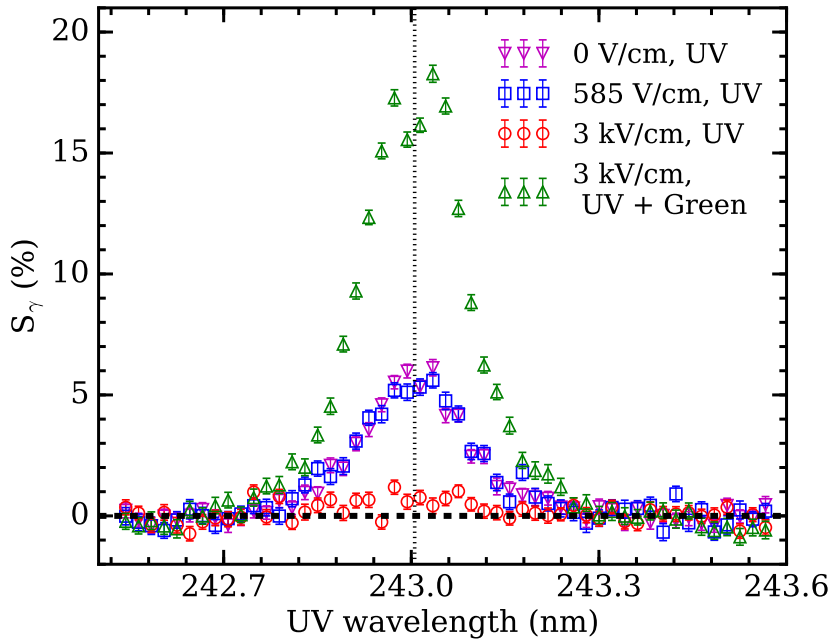

Figure 4.7: Spectra encompassing the $1^3S_1 \rightarrow 2^3P_J$ transitions in a range of electric fields. The data were recorded using laser radiation polarized parallel to the electric field ($\Delta M_J = 0$). For one scan (UV + Green) a 532 nm photoionization laser was also present to directly compare magnetic quenching and ionization signals. The noticeable Lamb dip [Demtröder 2003] in both the ionization and quenching lineshapes is attributed to UV radiation reflected from uncoated vacuum windows. From [Alonso *et al.* 2016b].

states, leading to an increase in their lifetime. By selecting the polarization of the laser radiation to be parallel to the electric field (see figure 3.4), excitation to states with a significant 2^3S_1 component can be optimized. We used this information to produce Ps atoms in the 2^3S_1 state using single photon excitation, these results outlined in the next section.

4.2 Production of 2^3S_1 positronium

Making use of the quenching mechanism described in the previous section, and utilizing fast high-voltage switching, it is possible to produce ensembles of pure 2^3S_1 states of Ps. The results shown in section 4.1.2 indicate that it should be possible to produce 2^3S_1 atoms by single photon excitation. This process, which is ordinarily forbidden by electric dipole selection rules (e.g., [Demtröder 2003]), is made possible by exciting Ps atoms in an electric field, so that Stark-mixing adds some P character to 2^3S_1 states; for the remainder of this section we shall refer to these mixed states as $2^3S_1'$ states. If the electric field in which they are produced is subsequently reduced to zero adiabatically, $2^3S_1'$ states can evolve into pure 2^3S_1 states.

In order to characterize 2^3S_1 production we define ε_{2S} as the fraction of incident positrons that ultimately form 2^3S_1 atoms, ε_{Ps}, the fraction of incident positrons that form 1^3S_1 Ps atoms, and ε_{ex}, the fraction of available atoms that are excited. In general we may write $\varepsilon_{2S} = \varepsilon_{Ps} \times \varepsilon_{ex} \times \varepsilon_Q$, where ε_Q refers to the fraction of excited atoms that subsequently form 2^3S_1 states. For convenience in the following we assume $\varepsilon_{Ps} = 0.3$ for all cases, although it can vary considerably depending on the Ps formation target used [Schultz & Lynn 1988].

This section describes our method for generating pure 2^3S_1 atoms by adiabatic extraction of Stark-mixed states from an electric field to a field-free region. Ps atoms were optically excited in parallel electric and magnetic fields, except in this case the electric field is turned off immediately after the excitation has occurred by switching off both of the biases in the target and grid electrodes using high voltage switches, as explained in section 2.5 and shown in figure 4.8 for the fields relevant

Method	$\varepsilon_{2S}(\%)$	Comments	Ref.
e^+-metal	0.05	clean Cu(110)	[Schoepf *et al.* 1992]
e^+-metal	0.38	untreated W	[Steiger & Conti 1992]
e^+-metal	0.47	untreated Au	[Day *et al.* 2001]
e^+-gas	1.1	H_2 gas	[Laricchia *et al.* 1985]
$1^3S_1 \rightarrow 2^3S_1$	5.3	Doppler-free	[Haas *et al.* 2006]
$3^3P_J \rightarrow 2^3S_1$	0.9	$\varepsilon_{ex} = 0.25$	[Aghion *et al.* 2016]
$2^3S_1' \rightarrow 2^3S_1$	1.9	$\varepsilon_{ex} = 0.25$	[Alonso *et al.* 2017b]

Table 4.1: Production efficiencies of 2^3S_1 Ps atoms using different techniques. For cases that involve exciting ground state atoms, an experimentally realistic Ps formation fraction of $\varepsilon_{Ps} = 30$ % has been assumed. The $2^3S_1' \rightarrow 2^3S_1$ case does not include losses due to field switching times. From [Alonso *et al.* 2017b].

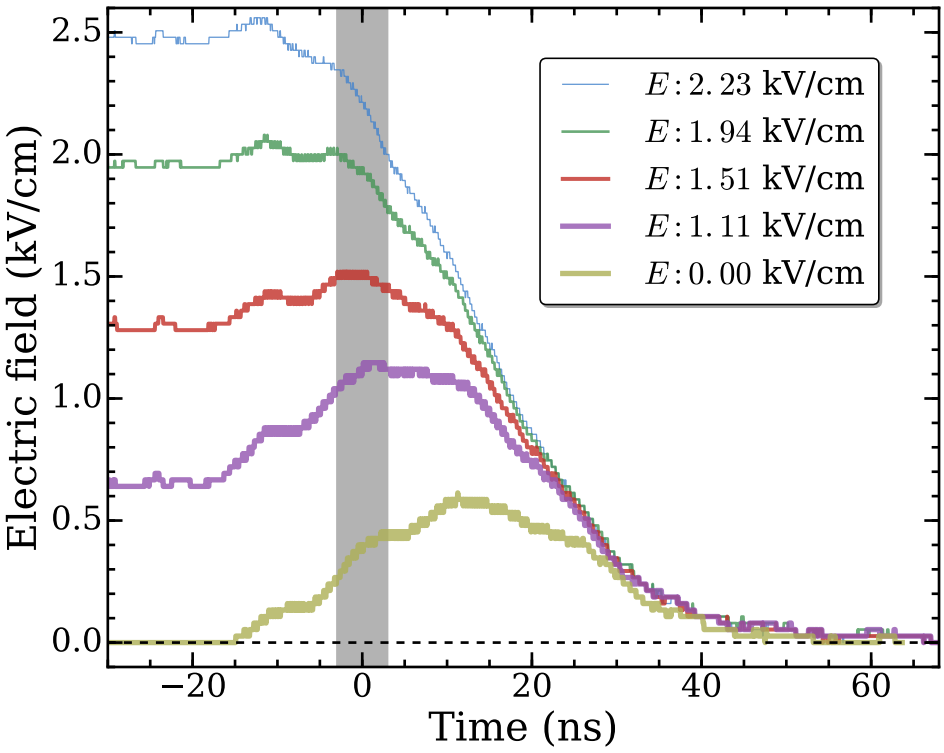

Figure 4.8: Time-dependence of the electric fields in the Ps excitation region, generated by switching off the target and grid electrode potentials. The shaded vertical bar indicates the time at which the laser is fired, and the temporal width of the laser pulse. The legend indicates the electric fields present at time $t = 0$ for different applied potentials. From [Alonso *et al.* 2017b]

to the measurements described here. If this is done on a time scale comparable with the lifetime of the $2^3S_1'$ states, that they can evolve into pure 2^3S_1 states. The efficiency with which this can be accomplished is limited by several factors which are discussed below; we estimate that in the present experiments we obtain $\varepsilon_{2S} \approx 0.2$ %.

As it can be seen from the yellow line in figure 4.8 where the initial field is 0 V/cm, if the target bias and the grid bias are switched at the same time (see figure 4.1 for relative target and grid positions), due to the differing capacitance of each electrode and thus the different switching time, the field during switching will not be zero. If laser excitation is performed during this switching cycle it will affect the electric field in the excitation region causing Stark broadening of the Rydberg lineshapes. This is shown in figure 4.9(a) where the $n = 13$ lineshape is measured when the switching occurs at approximately $\Delta t = 12$ ns, where Δt is the time when the high voltage switch is triggered. It can be seen that the lineshape at this switching time is equivalent to having a DC field of 400 V/cm. This allows us to determine the exact overlap of the positronium cloud laser excitation with the switching time, and as it can be seen from figure 4.9(b), if the switching takes place after $\Delta t \sim 32$ ns, it no longer causes Stark broadening, meaning that is the appropriate time to begin switching the voltages without affecting the laser excitation.

If there is a permanent voltage applied to the target and grid electrodes, even if the field between them is ~ 0 V/cm, after the Ps atoms exit the excitation region, they will experience a large electric field due to the voltage on the grid and the nearest ground plane (the chamber walls). This is enough to field-ionize most Rydberg states above $n \simeq 18$. This can be avoided by switching off the voltage on the grid (and the target simultaneously) as explained above and shown in figure 4.9. If the voltage applied to the grid is sufficiently low by the time that the atoms leave the region, they will be able to continue traveling until they annihilate due to hitting the chamber walls or radiatively decaying into the ground state.

This can be seen in figure 4.10 where $n = 18$ and 19 were excited in approximately zero electric field, by biasing both the grid and the target to 4 kV, and the

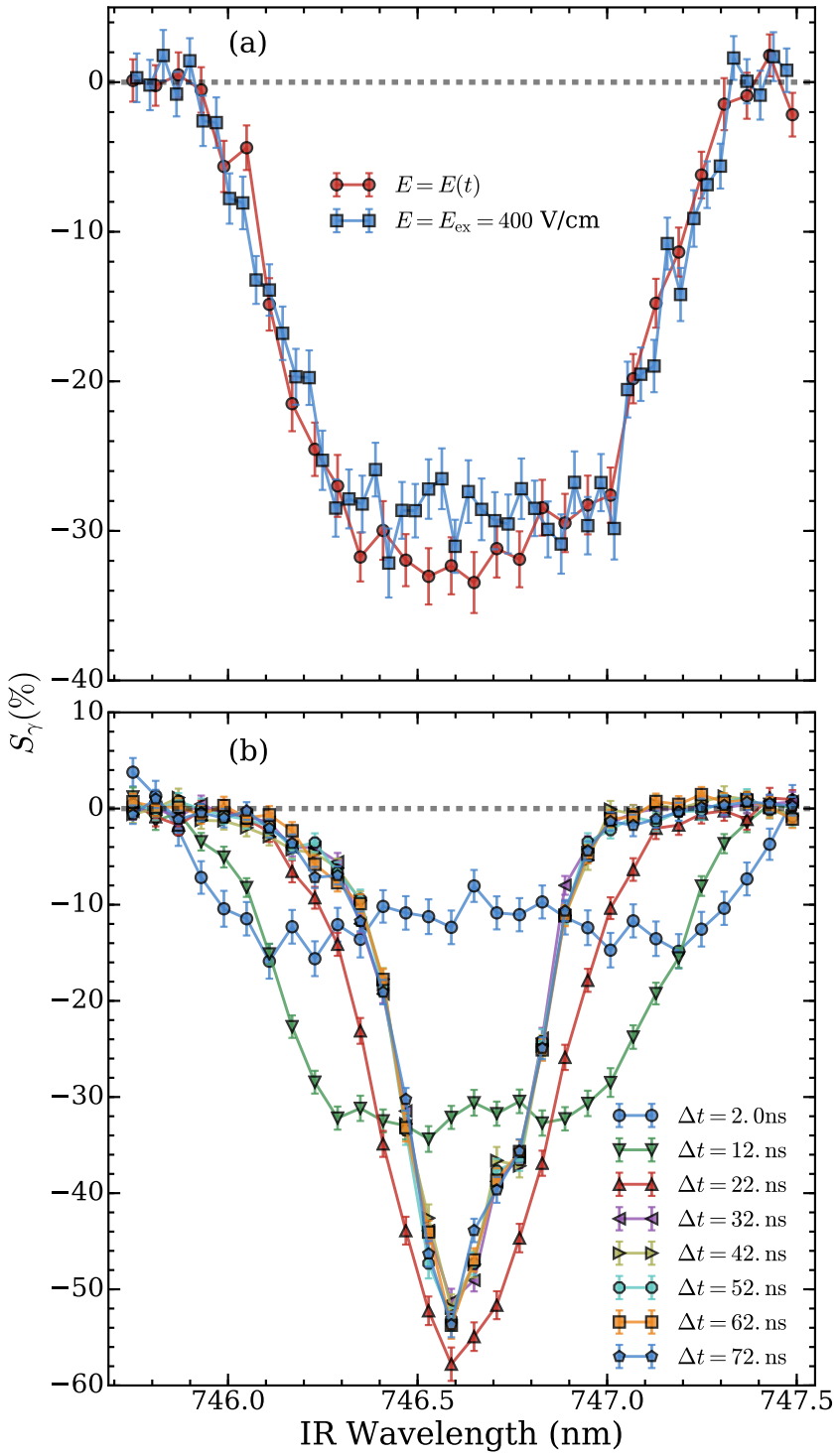

Figure 4.9: (a) $n = 13$ lineshape comparison for a static field value of 400 V/cm (red circles) and an electric field caused by switching the excitation region grid and target at the same time, thus inadvertently creating a field due to the different capacitance of the grid and target (blue squares), the switching time with respect to laser excitation is ~ 12 ns. (b) Broadening of the line caused by switching at different times, it can be seen that after $\Delta t \sim 32$ ns the excitation field is no longer affected, since the voltage change is happening after the laser pulses have left the excitation region.

annihilation radiation was detected by "Detector A" [see figure 4.1(a)]. In the case where the bias is not turned off ("Switch Off"), there is a large excess in annihilation gamma-ray signal at $t \sim 100$ ns, which corresponds to Rydberg Ps atoms being field ionized straight after exiting the excitation region, $n = 18$ has a small amount of excess annihilation at later times (~ 600 ns) which is due to a small amount of atoms exiting the grid at the center-most point, where the diverging fields to the chamber walls are weakest, and thus $n = 18$ does not get ionized. However, $n = 19$ is fully ionized and would be the limiting n state that we could transmit if we did not have the capability of switching the grid/target voltages off. It can be seen from the "Switch On" waveforms in figure 4.10 that the annihilation due to the grid voltage

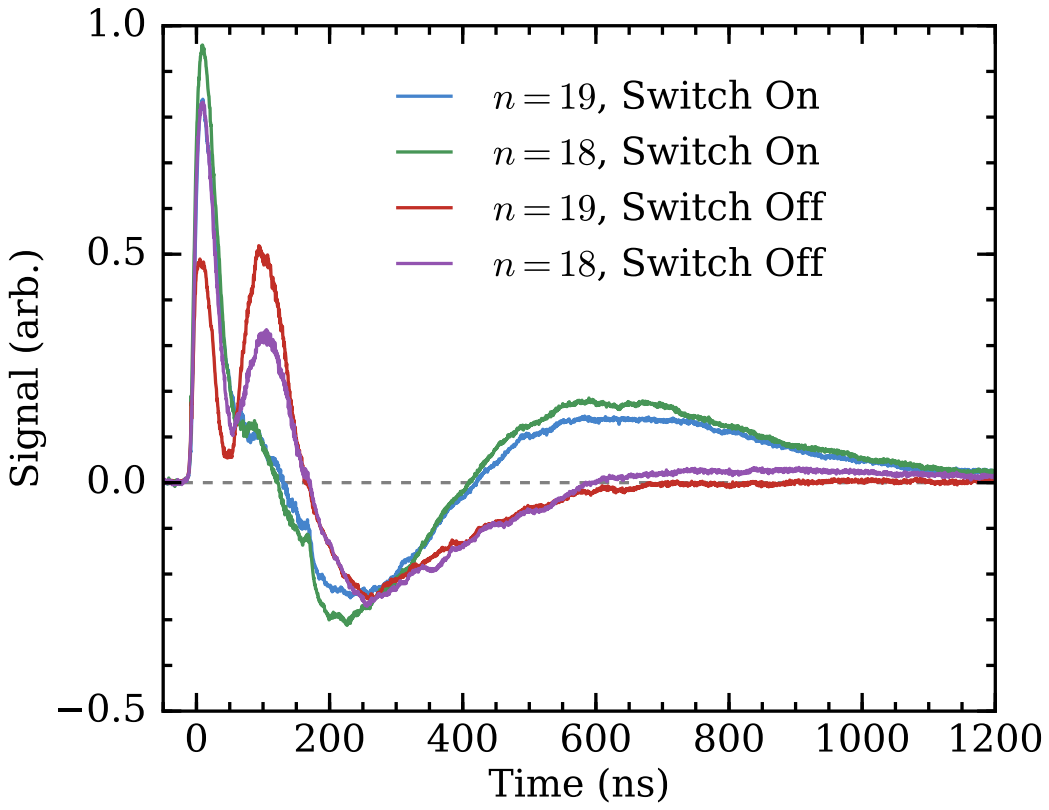

Figure 4.10: SSPALS background-subtracted spectra taken by detector A [shown in figure 4.1(a)] for $n = 18$ and $n = 19$. The electric field in the excitation region is ~ 0 V/cm, due to having biased the target and the grid at the same large voltage ($\sim$4kV/cm). The large bias on the grid causes a field after the excitation region that is able to ionize all $n = 19$ atoms and most $n = 18$, thus the excess signal at ~ 100 ns. When the bias on both electrodes is switched off before the atoms leave, both $n = 18$ and $n = 19$ can survive until hitting the chamber walls, thus causing the excess at ~ 600 ns.

can be completely suppressed when the voltage is switched off before the atoms exit the interaction region, since they are allowed to diverge and travel further, they collide with the chamber walls and emit gamma rays that are detected at $t \sim 600$ ns.

Figure 4.11 shows the single-event annihilation gamma rays detected by "Detector B" simultaneously to that shown in figure 4.10. In this case, it can be seen that even though a large portion of $n = 18$ atoms can be prevented from annihilating (as shown in figure 4.10), this does not significantly affect the count rate on Detector B, this is due to the fact that Detector B is only sensitive to atoms that are not very divergent, since they would collide with the chamber walls before reaching the

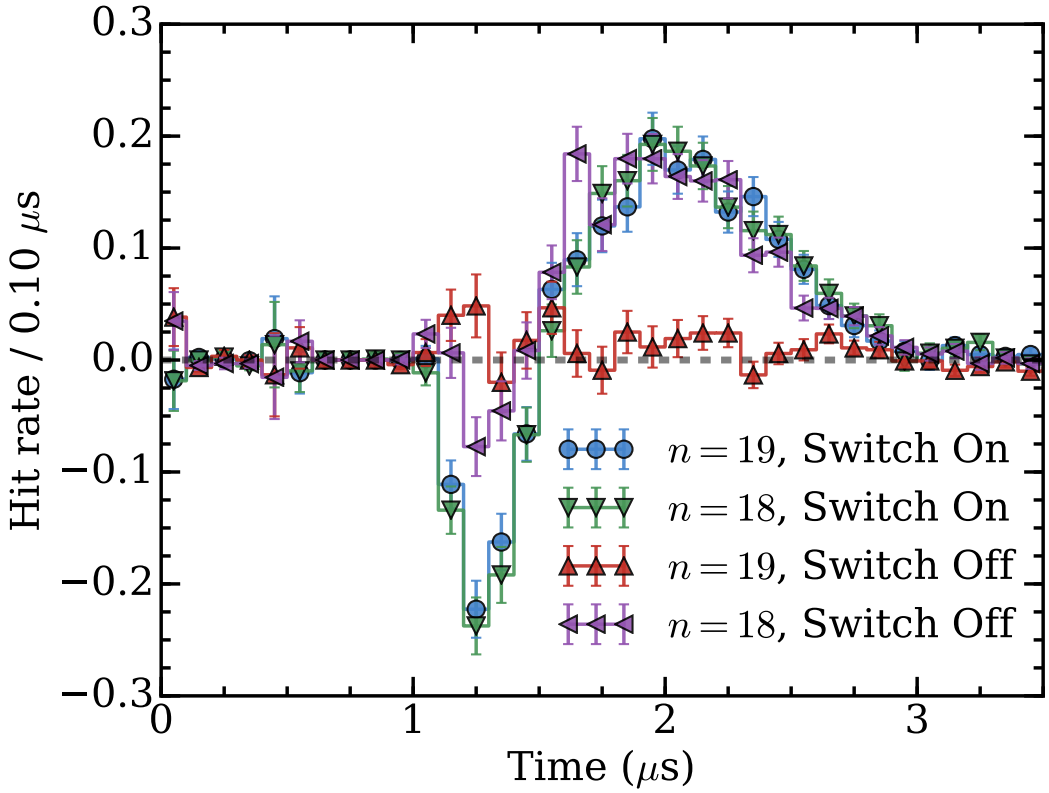

Figure 4.11: Singe-event counting data corresponding to the measurements in figure 4.10 as recorded by the more distant detector B [shown in figure 4.1(a)]. It can be seen that switching off the field outside the excitation region does indeed allow $n = 19$ to pass through the grid without being ionized. However, the count rate for $n = 18$ remains the same due to the fact that detector B can only detect atoms that have small perpendicular velocities, such that they do not collide with the walls before reaching the detector, these atoms will also experience smaller fields due to the divergent nature of the electric field from the grid to the chamber walls, and therefore do not get ionized even in the DC field case.

detector. For $n = 18$ these are also the atoms that are not ionized by the DC electric fields, due to being emitted from the center of the grid, the count rate for $n = 18$ is unchanged. However, as expected for $n = 19$, switching off the grid/target voltage allows these atoms to exit the excitation region and reach detector B.

Calculated Stark energies of the $n = 2$ eigenstates are shown in figure 4.12 (a), with the $2^3S'_1$ level indicated by the bold line. In order to produce pure 2^3S_1 atoms it is necessary to perform the excitation in an electric field that provides sufficient coupling to the $2^3S'_1$ state (via its P component), and then to lower the field on a time-scale commensurate with the lifetime of the $2^3S'_1$ states. The fraction of P character, and hence the $2^3S'_1$ lifetime, depends on the electric field strength, as shown in figure 4.12 (b) and figure 4.12 (c). The energies and lifetimes in the presence of electric and magnetic fields were determined from the eigenvalues and eigenvectors of the complete $n = 2$ Hamiltonian matrix using the procedures described in section 3.

Since the annihilation rate of Ps Stark-states with $n = 8$ is negligible, but their fluorescence lifetime is ≈ 1 μs [Deller *et al.* 2016b]. This is sufficiently close to the 1.1 μs annihilation lifetime of 2^3S_1 atoms that measurements employing $n = 8$ Rydberg atoms can provide a signal that has characteristics similar to those expected for the 2^3S_1 atoms, but with a much higher production efficiency. Such corresponding lifetime spectra recorded with the UV and IR lasers tuned to excite $n = 8$ states are shown in figure 4.13 (a).

The time-dependence of the annihilation radiation signal shown in figure 4.13 (b) is consistent with the physical geometry of the electrode structure and target chamber walls, and the mean speed of Ps atoms emitted from the silica target ($\approx 10^7$ cm s^{-1}). The underlying Ps velocity and angular distributions will be very similar for both $n = 2$ and $n = 8$ atoms because Doppler velocity selection by the excitation lasers is dominated by the UV laser bandwidth. Therefore the data in figure 4.13 are expected to give a good indication of the qualitative form of a 2^3S_1 signal, as long as additional annihilation channels are not present.

The goal of the measurement was to demonstrate that pure 2^3S_1 Ps atoms can

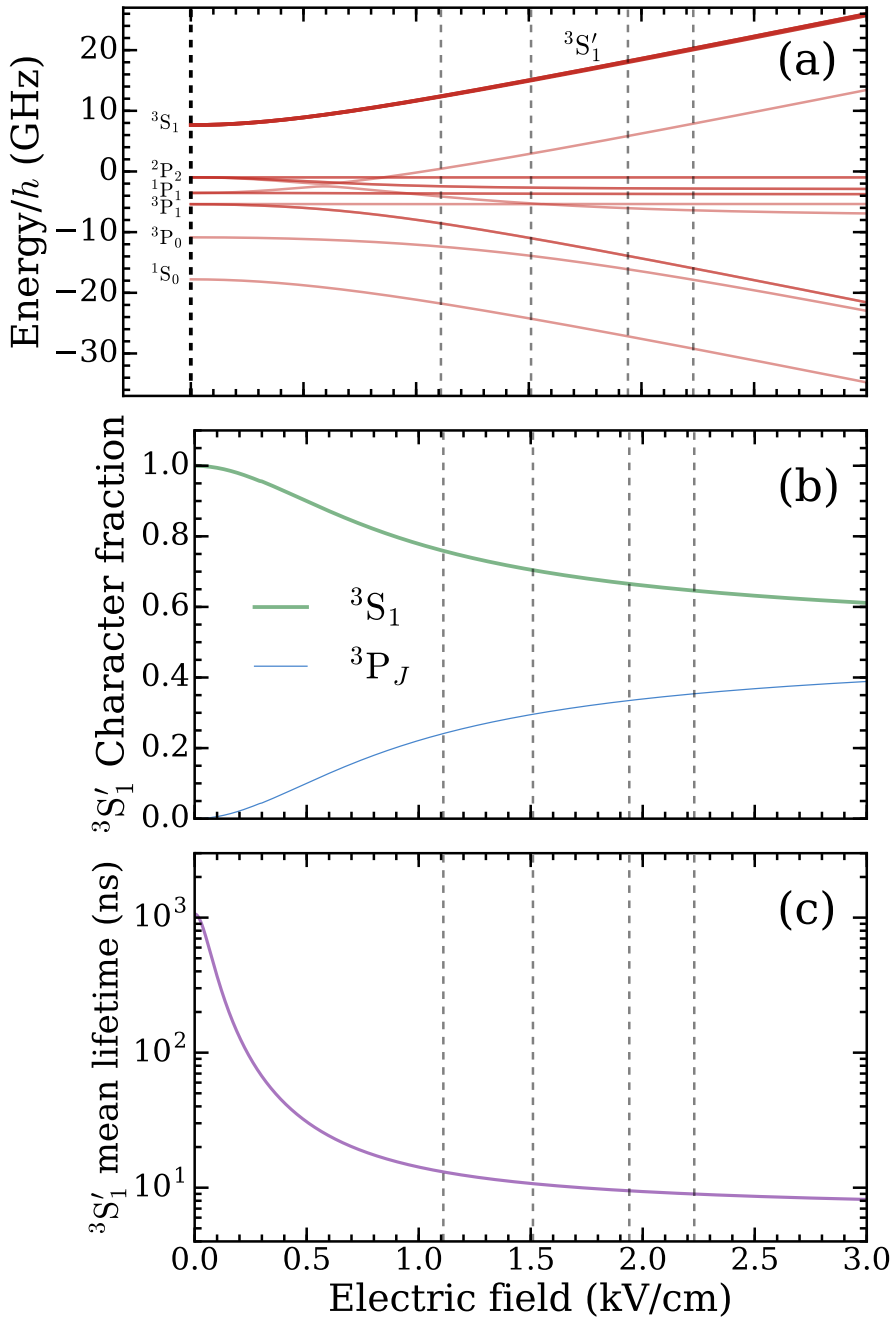

Figure 4.12: Calculated energy shift (a), fraction of 2^3S_1 and 2^3P_J character (b) and mean annihilation lifetimes (c) of the $2^3S_1'$ eigenstate as a function of the electric field, with a constant parallel magnetic field of 130 G. Also shown in (a) are the Stark shifts of other $n = 2$ levels. The dashed vertical lines indicate the excitation fields used used in the experiments. From [Alonso *et al.* 2017b].

be produced from $2^3S_1'$ atoms under typical experimental conditions, and to evaluate the efficacy of the process. We do in fact observe background-subtracted spectra characteristic of long-lived atoms when measurements are performed in a configuration expected to result in the production of 2^3S_1 states. The data in figure 4.14 (a) were recorded with an electric field of 2.23 kV cm^{-1}. When the electric field is switched off after excitation, an excess in annihilation signal peaking at $\approx$ 500 ns is observed. Using a static field that is always present, no excess signal is observed. The same measurement was performed in an electric field of 1.11 kV cm^{-1} [Figure 4.14 (b)] and an excess signal was observed. In this case, however, because

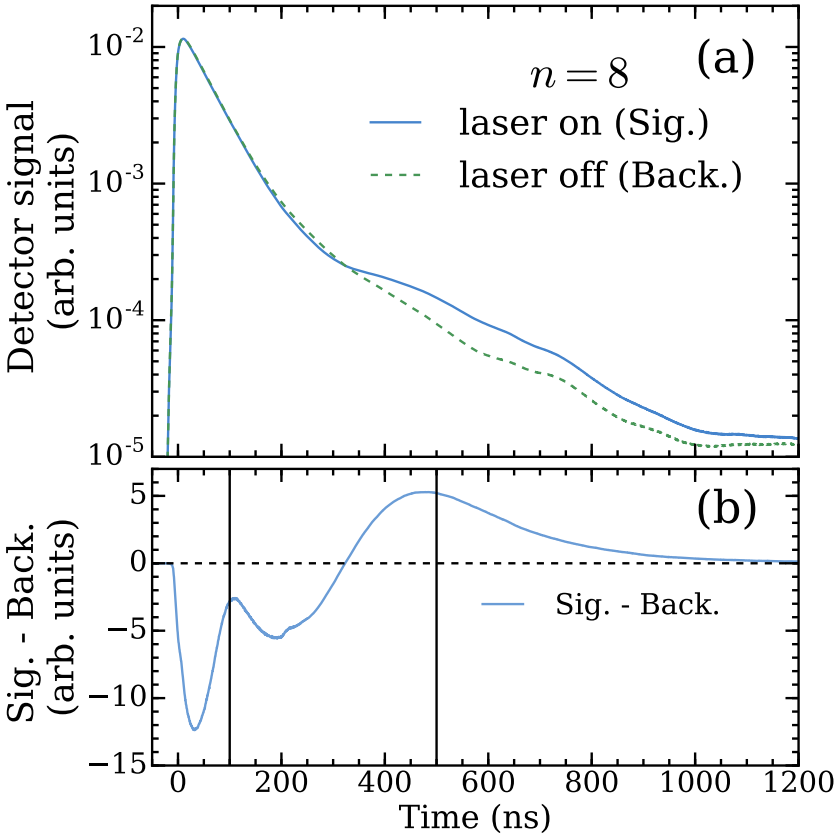

Figure 4.13: Lifetime spectra measured using LYSO A with and without laser light present (a). For these measurements the lasers were tuned to drive transitions to the $n = 8$ state. The difference between the laser on and off curves of (a) are shown in (b). The vertical lines at 100 and 500 ns indicate the approximate times of Ps annihilations occurring following collisions with the grid electrode and the chamber walls, respectively. The data are averages of 29000 shots each, and were acquired in 17 hours in a nominally zero electric field. From [Alonso *et al.* 2017b].

of the low excitation field there is also a magnetic quenching signal present. This signal is visible as an increase in annihilation events at early times and is relatively strong, making the 2^3S_1 signal appear less prominent. However, as can be seen more clearly in the inset to figure 4.14 (b), the magnitude of the delayed signal is comparable to that observed for higher fields. Similar measurements were also performed for fields of 1.51 and 1.94 kV cm^{-1} (see figure 4.15) as highlighted in figure 4.12.

The presence of long-lived Ps atoms can also be detected via single-event counting using detector B (see figure 4.1). This detector is further away from the

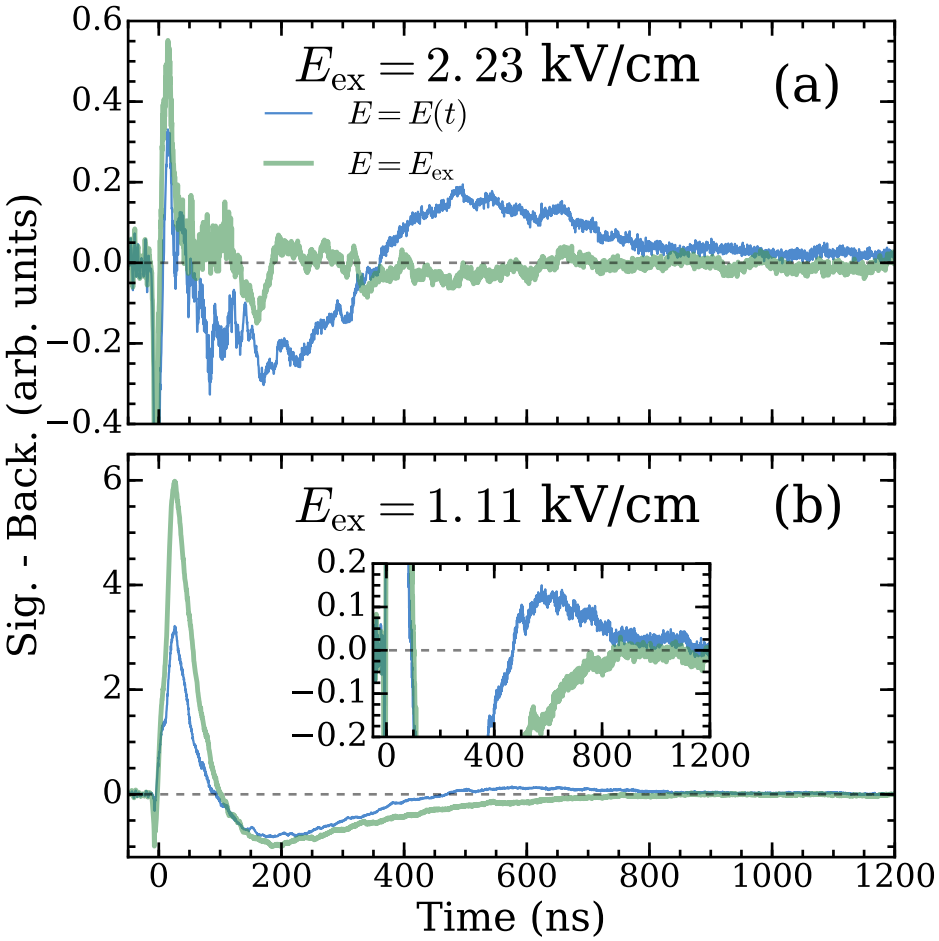

Figure 4.14: Difference curves recorded using LYSO A for excitation fields E_{ex} of (a) 2.23 kV/cm and (b) 1.11 kV/cm. Data are shown for for fields that are switched off ($E = E(t)$) and that are held at the excitation field ($E = E_{ex}$). The inset in (b) shows the delayed signal attributed to 2^3S_1 atoms on an expanded scale. Each curve is the average of approximately 13000 shots, and was acquired in 3.7 hours. From [Alonso *et al.* 2017b].

Ps target, and is therefore more sensitive to delayed annihilation events. A single-event counting procedure was used to produce time-of-flight (TOF) spectra, as described in section 2.4. TOF data are shown in figure 4.16; these were recorded at the same time as the data shown in figure 4.13 and figure 4.14. The TOF spectra have been background subtracted, where the background corresponds to the case where no laser light is present. Additionally, figure 4.17 shows TOF data for 1.51 and 1.94 kV cm^{-1}.

As in the single-shot lifetime data, the production of $n = 8$ atoms can provide a proxy signal that will have similar qualitative properties to that expected for 2^3S_1

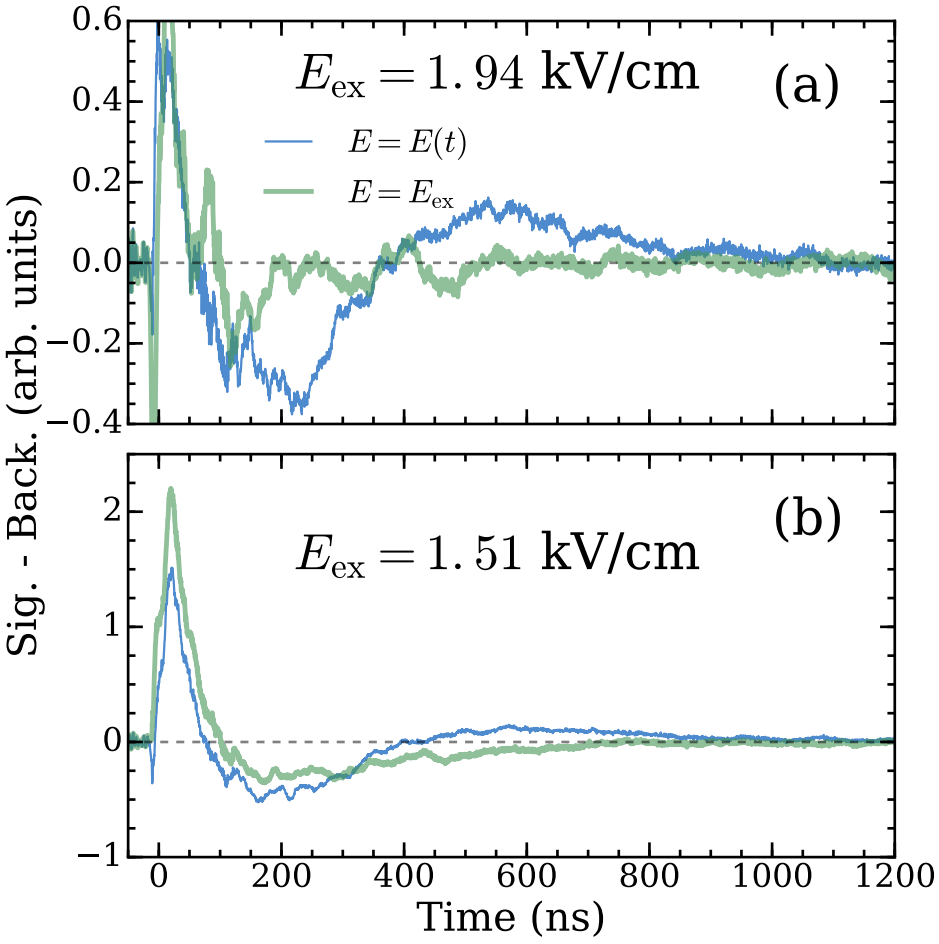

Figure 4.15: Difference curves recorded using LYSO A for excitation fields E_{ex} of (a) 1.94 kV/cm and (b) 1.51 kV/cm. Data are shown for for fields that are switched off ($E = E(t)$) and that are held at the excitation field ($E = E_{ex}$). The inset in (b) shows the delayed signal attributed to 2^3S_1 atoms on an expanded scale. Each curve is the average of approximately 13000 shots, and was acquired in 3.7 hours.

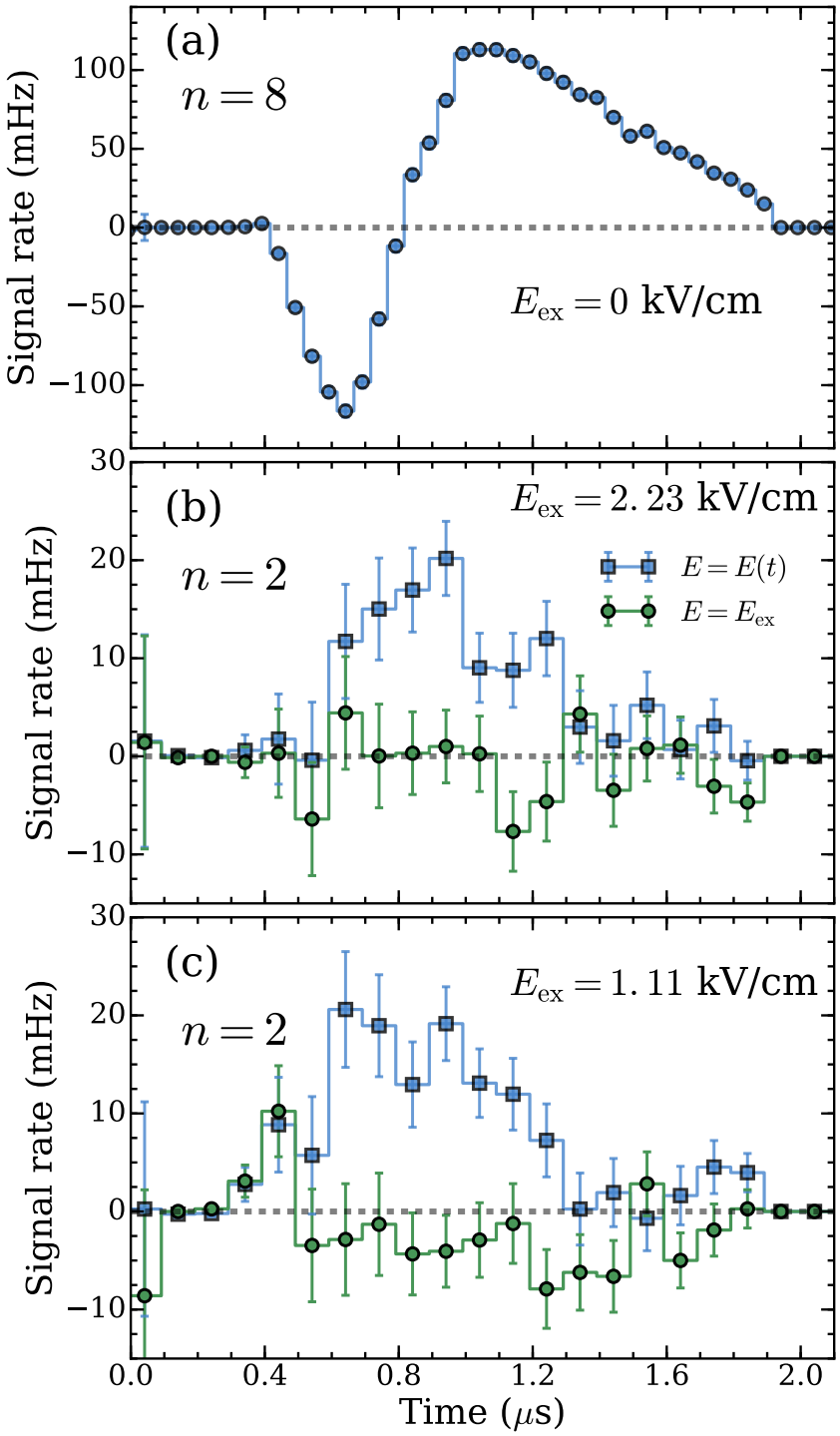

Figure 4.16: TOF spectra recorded by LYSO B with lasers tuned to excite $n = 8$ Rydberg states (a) or $n = 2$ states (b) and (c). The spectra are background subtracted as described in the text. Data were recorded in different electric fields, as indicated in each panel, and for the $n = 2$ data for cases with the fields switched off ($E = E(t)$, squares) or for static fields ($E = E_{ex}$, circles). From [Alonso *et al.* 2017b].

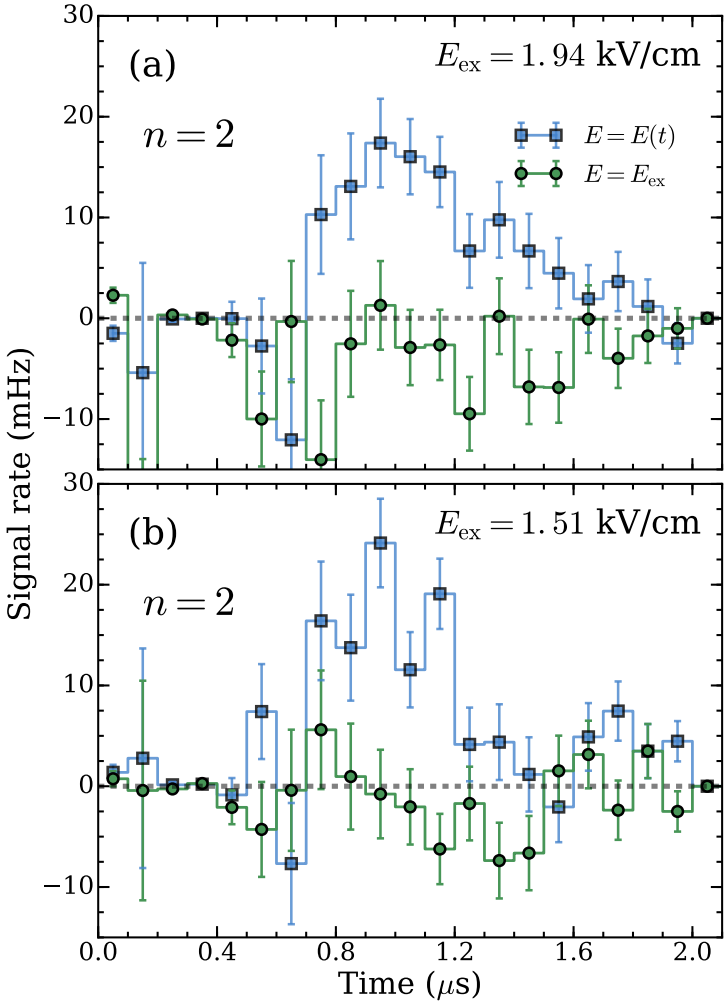

Figure 4.17: TOF spectra recorded by LYSO B with lasers tuned to excite $n = 2$ states. The spectra are background subtracted as described in the text. Data were recorded in different electric fields, as indicated in each panel, and for the $n = 2$ data for cases with the fields switched off ($E = E(t)$, squares) or for static fields ($E = E_{ex}$, circles).

atoms. Figure 4.16 (a) shows TOF data recorded with the UV and IR lasers tuned to excite $n = 8$ atoms. For these data the background subtraction procedure results in a negative peak at early times in the distribution because the transfer of ground-state atoms to Rydberg levels is so efficient that it significantly depletes the background population. By extrapolating over this negative region, however, one can infer that the distribution exhibits a peak in the region of $\sim 1\mu$s.

TOF spectra recorded under conditions where 2^3S_1 production is expected are shown in figure 4.16 and 4.17 (*cf* figure 4.14 and 4.15). As observed in the lifetime

spectra, a delayed signal is present when the electric field is switched off, but not when the field is maintained after laser excitation has occurred. Thus, these data confirm the observation that 2^3S_1 atoms have been produced.

For a given detector configuration, and using fixed integration regions, one can compare different S_γ measurements to infer a relative yield of long-lived states. The positive value of S_γ shown in figure 4.18 for low static electric fields arises through magnetic quenching (covered in section 4.1), whereas the negative values are due to long lived 2^3S_1 atoms.

The data shown in figure 4.13 correspond to $S_\gamma = -60\%$, using time windows of A = -5, B = 400 and C = 1200 ns (see equation 2.2 and equation 2.3). The 2^3S_1 production as measured via S_γ does not appear to depend strongly on the electric field, as shown in figure 4.8 (a). The average value obtained $S_\gamma = -2.2 \pm 0.4\%$ indicates that the production efficiency of 2^3S_1 atoms compared to Rydberg atoms was about 4%. If all of the accessible $n = 2$ states are produced with equal probability then, considering the allowed transitions and the laser polarization used (vertical) [Alonso *et al.* 2016a], the fraction of those in $2^3S_1'$ states would be 25% (i.e.,

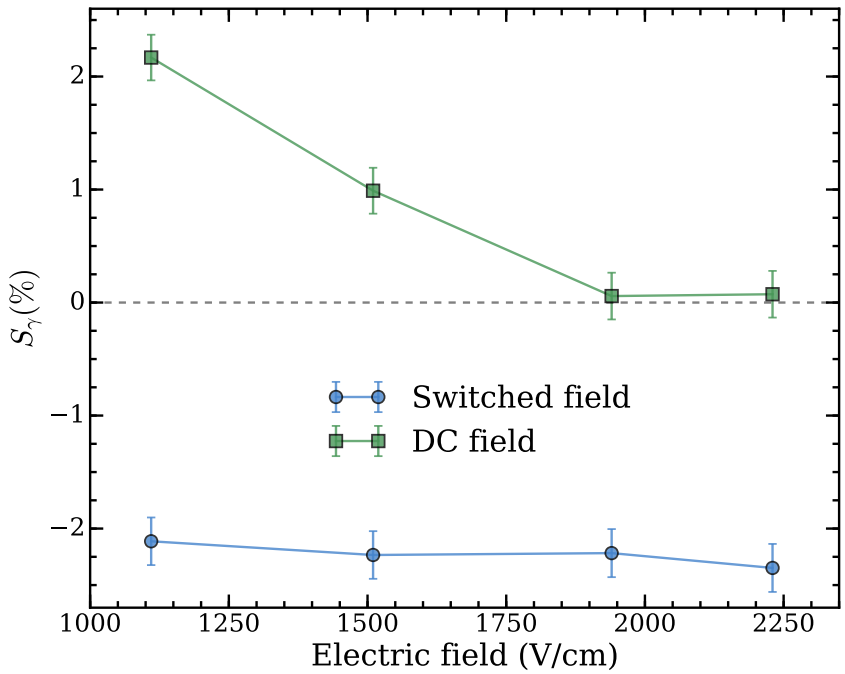

Figure 4.18: S_γ values obtained from lifetime spectra of figure 4.14 with and without switching off the electric field. From [Alonso *et al.* 2017b].

$\varepsilon_Q = 0.25$). If we assume that almost all $n = 2$ states are transferred to Rydberg levels [Cassidy *et al.* 2012a] then we would expect to measure $S_\gamma \approx -15$ %. The observed $S_\gamma = -2.2\%$ therefore suggests that an additional loss mechanism may be present.

This additional loss mechanism was investigated in [Alonso *et al.* 2017b] using simulations. By comparing the measurements with a Monte-Carlo simulation that included the measured electric field switching times as well as the excitation efficiencies and the corresponding 2^3S_1 and 2^3P characters, it was determined that the relatively long switching time of the electric fields is responsible for over 90% of these losses, which are caused mostly by fluorescent decay to the 1^3S_1 level. It was determined that if the switching time could be reduced to ~ 2 ns these losses would be recovered thus producing the expected S_γ values of $\sim -15\%$.

We estimate that in our experiments $\varepsilon_{ex} \approx 0.25$ and $\varepsilon_{Ps} \approx 0.3$. For $\varepsilon_Q \approx 0.25$ (i.e., the ideal case without switching losses) the maximum yield per positron is then $\varepsilon_{2S} \approx 1.9\%$.

Chapter 5

Selective production of Rydberg Stark states of positronium

The experiments and results discussed in this chapter have been previously published in several articles, and as such, much of the content and figures used here were From these publications. Contents from this chapter describing our ability to selectively produce specific k states of positronium and our measurements of fluorescence Rydberg lifetimes have been published in the following articles:

- T. E. Wall, A. M. Alonso, B. S. Cooper, A. Deller, S. D. Hogan, and D. B. Cassidy. *Selective Production of Rydberg-Stark States of Positronium.* Phys. Rev. Lett., **114**, 173001 (2015). doi: 10.1103/PhysRevLett.114.173001.

- A. Deller, A. M. Alonso, B. S. Cooper, S. D. Hogan, and D. B. Cassidy *Measurement of Rydberg positronium fluorescence lifetimes*. Phys. Rev. A, **93**, 062513 (2016). doi: 10.1103/PhysRevA.93.062513.

- A. M. Alonso, B. S. Cooper, A. Deller and D. B. Cassidy. *Single-shot positron annihilation lifetime spectroscopy with LYSO scintillators*. NIMA, **828**, 163 (2016). doi: 10.1016/j.nima.2016.05.049.

5.1 Rydberg positronium production

In order to excite ground state Ps to Rydberg levels we use a two-photon ($1\,^3\mathrm{S} \rightarrow 2\,^3\mathrm{P} \rightarrow n\,^3\mathrm{S}/^3\mathrm{D}$) excitation scheme through $n = 2$ as described in section 2. The main motivation for exciting Ps to Rydberg states is to increase the lifetime of the atoms, and to take advantage of their increased dipole moment to manipulate their motion. One can use inhomogeneous electric fields to control Rydberg Ps [Deller *et al.* 2016a, Alonso *et al.* 2017a] atoms in much the same way as been demonstrated for hydrogen [Vliegen *et al.* 2007] and other Rydberg atoms and molecules [Hogan & Merkt 2008].

The ability to selectively populate individual Rydberg-Stark states is advantageous to schemes designed to control Ps atoms via their electric dipole moments. Here I describe how our first Rydberg Ps excitation was performed, and the methods used immediately after to selectively produce individual k states in specific m manifolds by changing the laser polarization of the excitation radiation.

The production of Ps Rydberg states ranging from n = 9 up to the ionization limit was verified in measurements conducted in (nominally) zero electric field, as shown in figure 5.1. The states were resolved up to n $\sim$ 30 [figure 5.1 (c)]. For these measurements the background signal was obtained with the UV laser tuned to the $1\,^3\mathrm{S} \rightarrow 2\,^3\mathrm{P}$ resonance, and the IR laser averaged over 755-758.5 nm where it is not resonant with any n state and is therefore essentially as if it was "off", so that S_γ is sensitive only to the $2\,^3\mathrm{P} \rightarrow n\,^3\mathrm{S}/^3\mathrm{D}$ transitions. The decrease in the background level for $\lambda > 760$ nm [figure 5.1 (a)] is due to the production of Rydberg states by broadband light emitted via amplified spontaneous emission (e.g., [Demtröder 2003]), as these wavelengths are approaching the upper limit of the gain curve of the Styryl-8 dye used in the IR laser (see section 2.1.3). Both lasers were linearly polarized in the vertical direction for this particular measurement.

A notable feature of these data is that the negative S_γ values are inverted for $n > 17$, as seen in figure 5.1 (c), becoming positive thereafter. The timing windows used to analyze these data ($A = -2$, $B = 226$, $C = 597$) are such that this inversion occurs when Ps atoms are no longer able to pass through the grid due to field

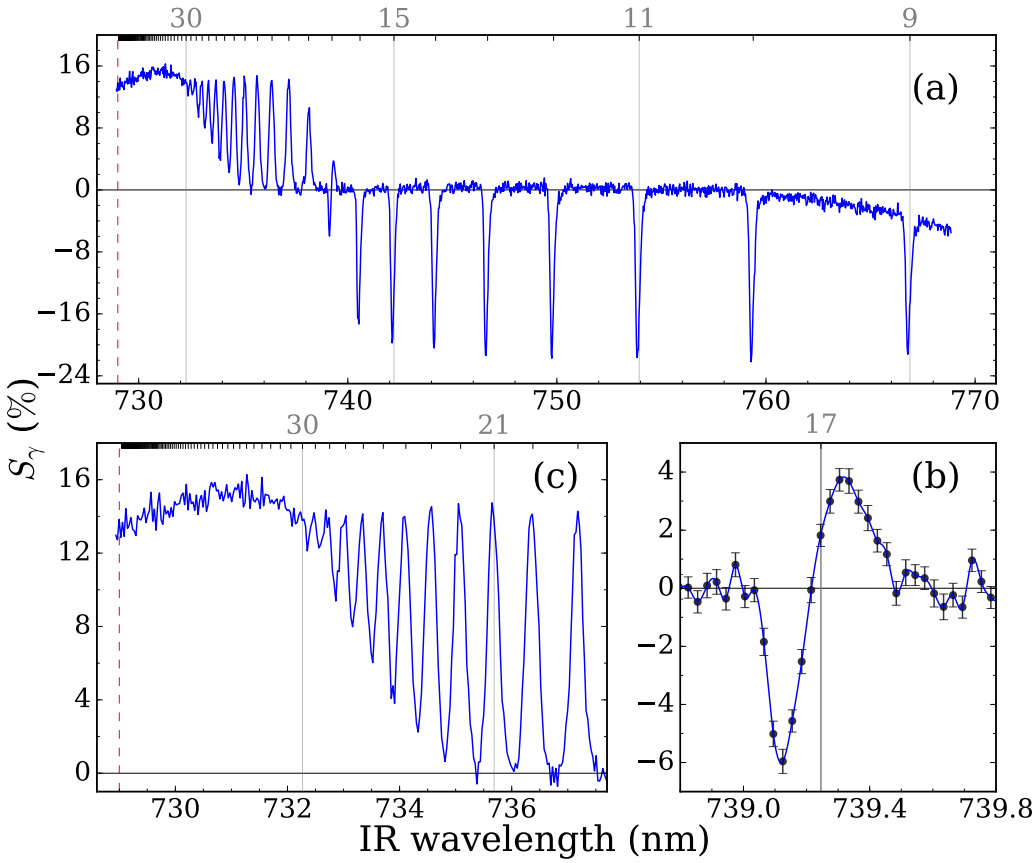

Figure 5.1: (a) Measured spectrum of Rydberg states excited in zero applied electric field. The data for n = 17 is expanded in (b) and $n \geq 19$ is shown in (c). The reversal of the sign of S is due to Ps atoms that cannot pass through the grid. The dashed lines indicate the ionization limit (729 nm). The timing windows used to analyze these data were A = -2 ns, B = 226 ns and C = 597 ns). The error bars, not shown in (a) or (c) for clarity, are of the same size as those shown in (b). Values of n are shown in the top axes of (a) and (c). From [Wall *et al.* 2015].

ionization, and Ps annihilation therefore occurs at earlier times. It is important to note that the magnitude of the positive and negative peaks cannot be directly compared as the detection efficiency is not the same in both cases. No electric field was applied in the excitation region when these data were recorded, however, the $\sim$ 130 G magnetic field will give rise to motional Stark fields that may be as high as 10 V/cm. There may also be fields present that are generated by secondary electrons produced following positron irradiation of the target [Overton & Coleman 1997] or photoelectrons made by the UV laser. The combined effect of these fields polarizes the Rydberg states in the excitation region, leading to a weak Stark splitting

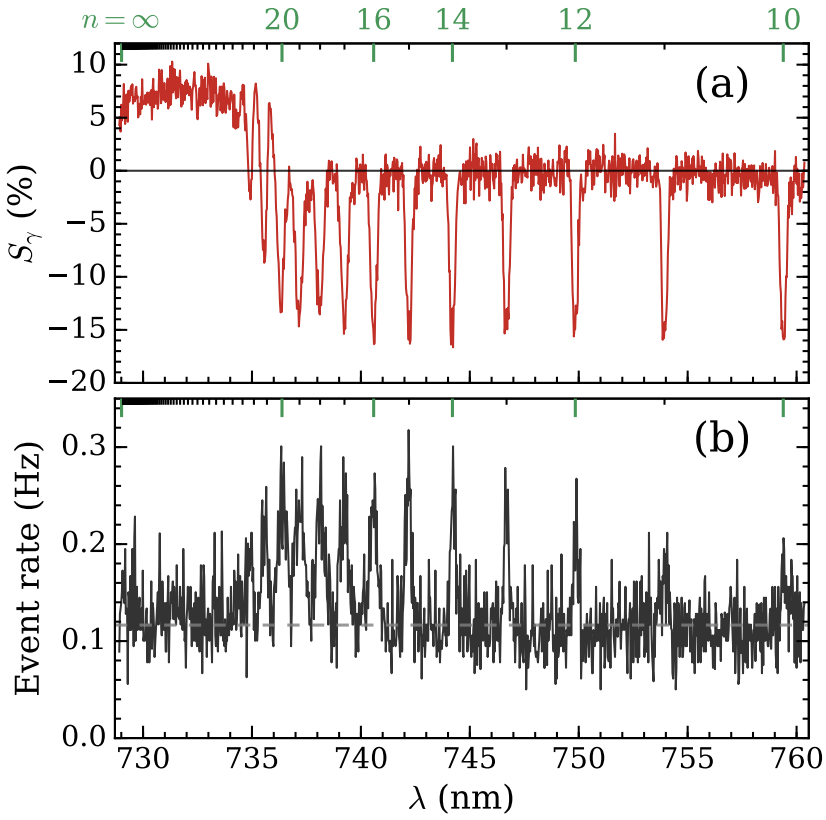

Figure 5.2: (a) SSPALS signal as the wavelength of the IR laser is tuned over the range of $n = 10 - \infty$. The expected position of each n-state is indicated along the top-axis. (b) Event rate registered by a detector positioned 1.2 m from the Ps-converter over the time window of 0.8 - 18 μs after positron implantation. Each data point represents 300 trap cycles. From [Deller *et al.* 2016b].

[Gallagher 1994].

Figure 5.2(a) shows similar data to Figure 5.1(a), however, in this case the implantation energy of the positrons was around 2kV instead of 4kV, a "ring" electrode was used instead of a mesh for field control, the integration windows (see section 2.3) used were optimized for later annihilation times, and the Rydberg atoms were allowed to travel a distance of ∼1.2 m before being detected using the single-event–counting techniques described in section 2.4, yielding the results shown in figure 5.2(b), which shown that, as the lifetime of the atoms increases with n, they can be detected more efficiently since less of them decay before detection, but after $n = 22$ approximately, the atoms become field ionized by the field generated due to the ring electrode. In this study, it was also possible to measure the lifetime of

specific n states [Deller *et al.* 2016b] which agreed with calculations performed according to the m manifold being populated, however, these calculations were not part of the projects outlined on this thesis and so they shall not be discussed further (see [Deller *et al.* 2016b] for more information).

5.2 Rydberg Stark filter

As the Rydberg Ps atoms pass through the grid (see figure 2.11) they experience a large inhomogeneous electric field on a distance scale commensurate with the mesh spacing ($\sim$ 100 μm). After being transmitted any remaining Rydberg Ps atoms experience an approximately homogeneous electric field defined by the potential applied to the grid plane. The data presented in figure 5.3 show spectra covering the transition to the $n = 18$ state, and demonstrate that transmission of Rydberg Ps atoms through the grid depends on their rate of electric field ionization. These data were recorded with a constant electric field of 63 V/cm applied to the excitation region and fields ranging from $\sim$1397 to 1985 V/cm in the region after the grid.

For weak fields, the short wavelength components of the $n = 18$ spectral feature are successfully transmitted through the grid (negative S_γ parameter) while only the outermost components at the long wavelength edge are not transmitted. This observation indicates that Rydberg-Stark states are sufficiently polarized by the electric field to result in a partial splitting of states with positive and negative Stark shifts, and that these states subsequently evolve adiabatically while passing from the excitation region through the grid.

Since the outermost Stark states with negative Stark shifts ionize in weaker electric fields than states with positive Stark shifts (see section 3.2), the cut-off in transmission through the grating occurs first for the outermost components at the long wavelength edge of the spectrum. For each value of n, the ionization field for the outermost Stark state with a negative Stark shift in Ps is approximately equal to the classical ionization field [Gallagher 1994] (*cf* equation 3.14)

$$F_{\text{ion}} = 2R_{\text{Ps}}hc/ea_{Ps}9n^4, \tag{5.1}$$

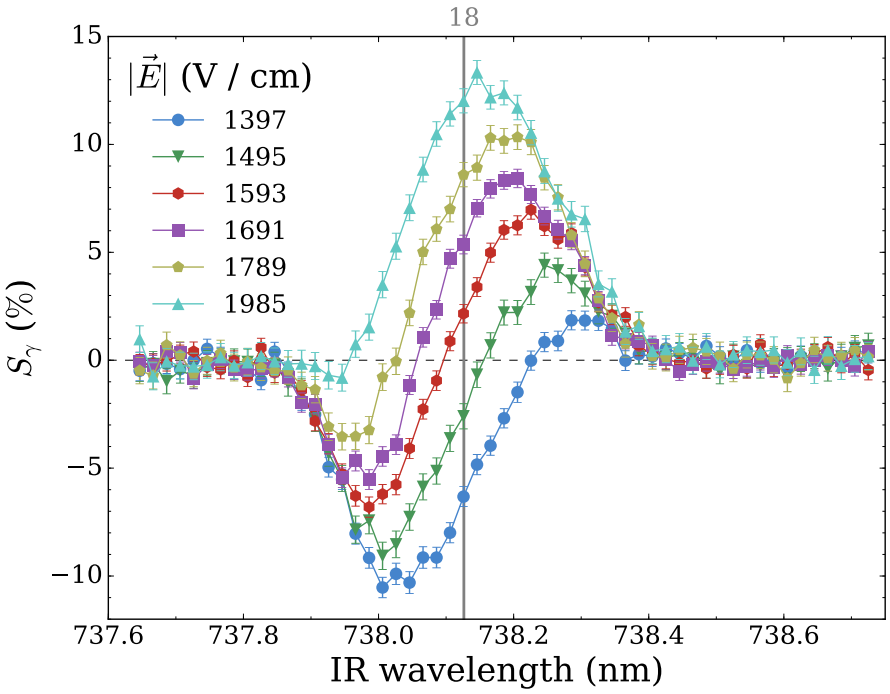

Figure 5.3: n = 18 peak measured with a 63 V/cm electric field in the excitation region and varying fields outside the grid as indicated. The vertical line shows the position of the n = 18 peak. Positive S_γ values indicate atoms in Stark states that cannot pass through the grid. From [Wall *et al.* 2015].

where $R_{\mathrm{Ps}} = 0.5\,R_\infty$ is the Rydberg constant for Ps, and $a_{Ps} = 2a_0 = 1.058 \times 10^{-10}$ m is the Ps Bohr radius. This suggests an ionization field of 1360 V/cm for $n = 18$, close to that observed for the transmission of the corresponding states in figure 5.3. On the other hand, the outermost Stark states with positive Stark shifts ionize at approximately $2F_{\mathrm{ion}}$, indicating that a field of 2721 V/cm is required to completely inhibit transmission through the grid for all states with $n = 18$. The observation that a field slightly below this (1985 V/cm) is sufficient to inhibit transmission of the outermost states with positive Stark shifts can be attributed to effects of n-mixing with states of higher principal quantum number in the combined magnetic and inhomogeneous electric fields in the vicinity of the grid. This possibility is further emphasized by figure 5.4 which shows that even at fields as low as $\sim$ 250V/cm, there is overlap with Stark states from neighboring n states ($n = 19$ in this case), thus, if there is a magnetic field present too (not included in the calculations shown in figure 5.4), the different Stark states would become mixed, and in the case of

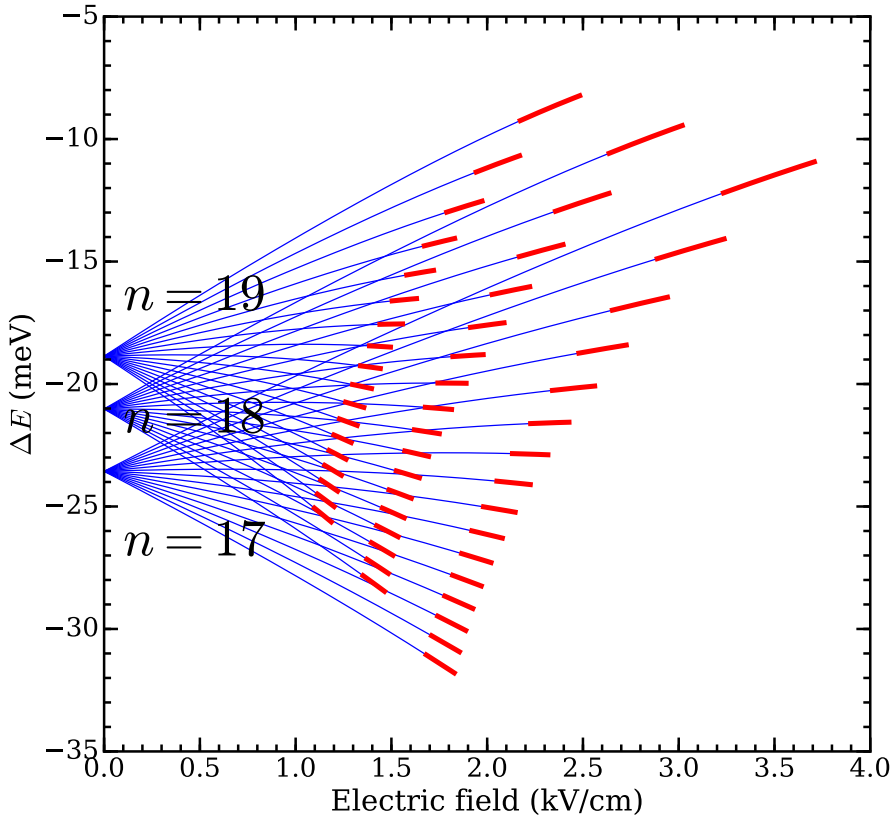

Figure 5.4: Stark shifted energy spectra calculated (up to fourth order, as described in equation 3.10) for $n = 17, 18$ and 19 and $|m| = 1$. The thick red lines show the range of fields for which each state has an ionization decay rate between 10^8 s^{-1} and 10^{10} s^{-1}.

positive Stark shifts for $n = 18$, they would become mixed with $n = 19$ (and others n states not shown for clarity), which have lower ionization fields, thus lowering the effective field ionization limit for these states. In this configuration the grid acts as a filter for the unresolved Rydberg-Stark states. This Stark-state filter permits spectral broadening arising from electric fields to be distinguished from Doppler broadening, and is therefore of particular value in obtaining information on the magnitude of the electric field in the photoexcitation region.

5.3 Selecting Stark states and varying laser polarization

To demonstrate the possibility of resolving individual Rydberg-Stark states, the lineshape for $n = 11$ was recorded at increasing electric fields until the Stark states

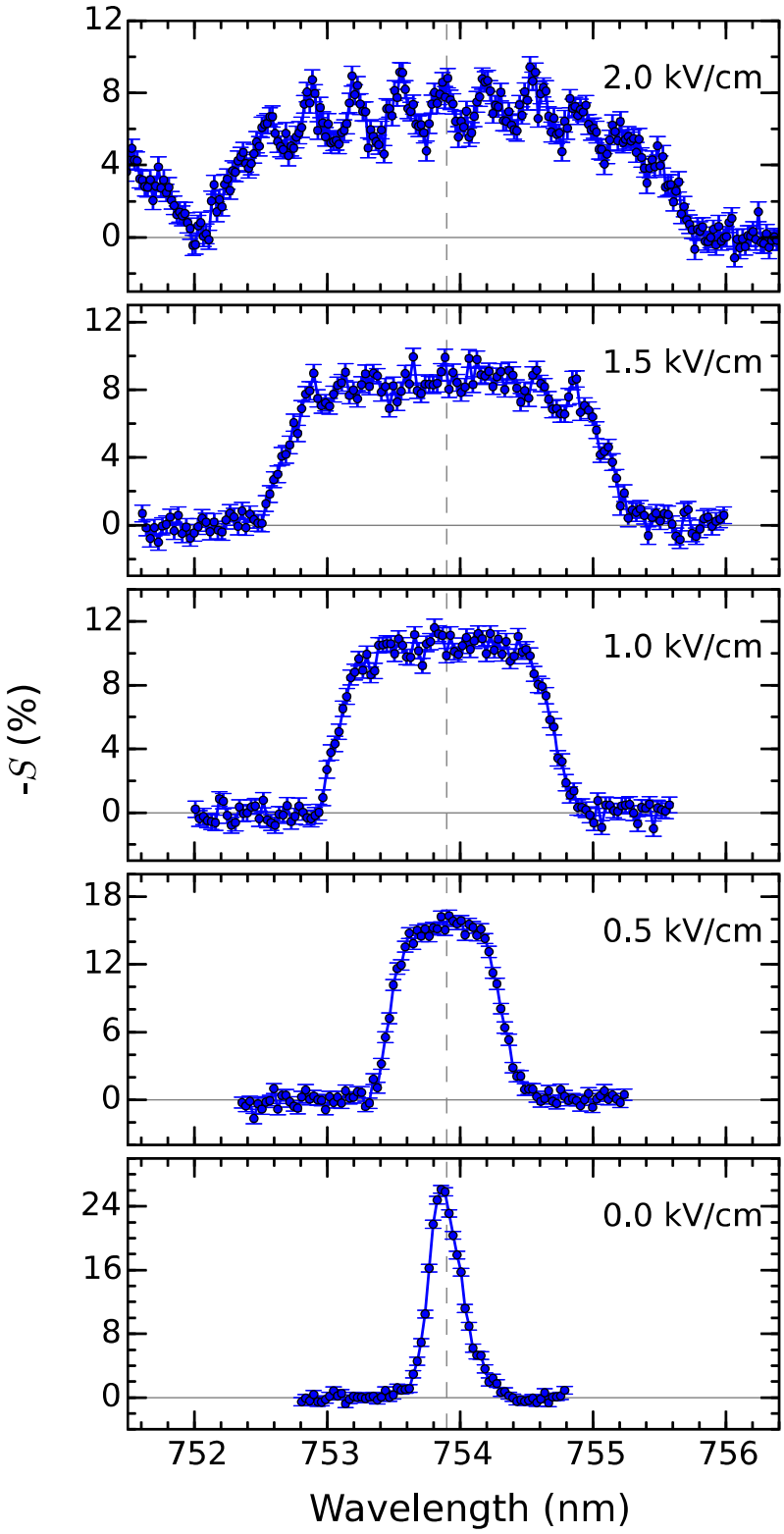

Figure 5.5: Stark broadening of $n = 11$ Ps states in various electric fields, as indicated in the panels. The dashed line represents the expected IR transition wavelength at zero field. For the highest field (2 kV/cm), the encroachment of neighboring $n = 12$ states can be seen at the shorter wavelengths. The individual Stark states can be partially resolved at the highest field, but are limited by the 85 GHz bandwidth of the 1S-2P excitation laser and Doppler broadening effects. From [Cooper *et al.* 2015].

could be resolved, this is shown in figure 5.5. Additionally, the spectra at the largest fields were recorded for multiple laser polarizations, the spectra presented in figure 5.6, the Stark states are separated in frequency by $\sim$ 165 GHz. However, this field also gives rise to mixing between the intermediate 2S and 2P triplet states (as described in chapter 4), and unresolved Stark splittings at $n = 2$ approaching 30 GHz. The complexity of the Stark structure arising from the spin-orbit coupling in this intermediate state means that the Stark manifolds in the Rydberg states can not be fully described by hydrogenic expressions for individual values of $|m|$, even at the 90 GHz resolution of the experiment. These effects are accounted for by calculating the eigenvalues and eigenvectors of the Hamiltonian matrix including the electric field for the triplet states of Ps with $n = 2$ in an $|nS\ell JM_J\rangle$ basis [Curry 1973] to determine the relative populations of each Stark sublevel. The results of this calculation were then used to determine the intensities of the subsequent transitions to the 11S and 11D Rydberg-Stark states following a transformation to the $|n\ell m_\ell\rangle$ basis for the description of these states. The results of this calculation, including a convolution with a 90 GHz FWHM Gaussian spectral function, are overlaid with the experimental data in figure 5.6.

The calculation does not take into account the polarization of the initial positron beam or optical pumping through $1\,^3\mathrm{S} \leftrightarrow 2\,^3\mathrm{P}$ transitions, which may play an important role. The asymmetric structures observed in the spectra of figure 5.6 are primarily related to the details of the Stark structure of the $n = 2$ manifold. However, even though the calculations shown in figure 5.6 are similar to those described in section 3.1, it should be noted that they did not constitute a part of the work outlined in this thesis and were performed in their entirety by S. D. Hogan.

Figure 5.7 shows an $n = 12$ lineshape performed in a similar way to the data shown in figure 5.1. It can be seen that the data recorded with a LYSO detector has better signal-to-noise ratio. This is relevant for other long-lived Ps measurements that were made plausible thanks to LYSO detectors. Additionally, figure 5.8 shows data taken with the same polarization as in figure 5.6(c) for $n = 11$, and it can also be seen that LYSO detectors are beneficial for these kind of measurements.

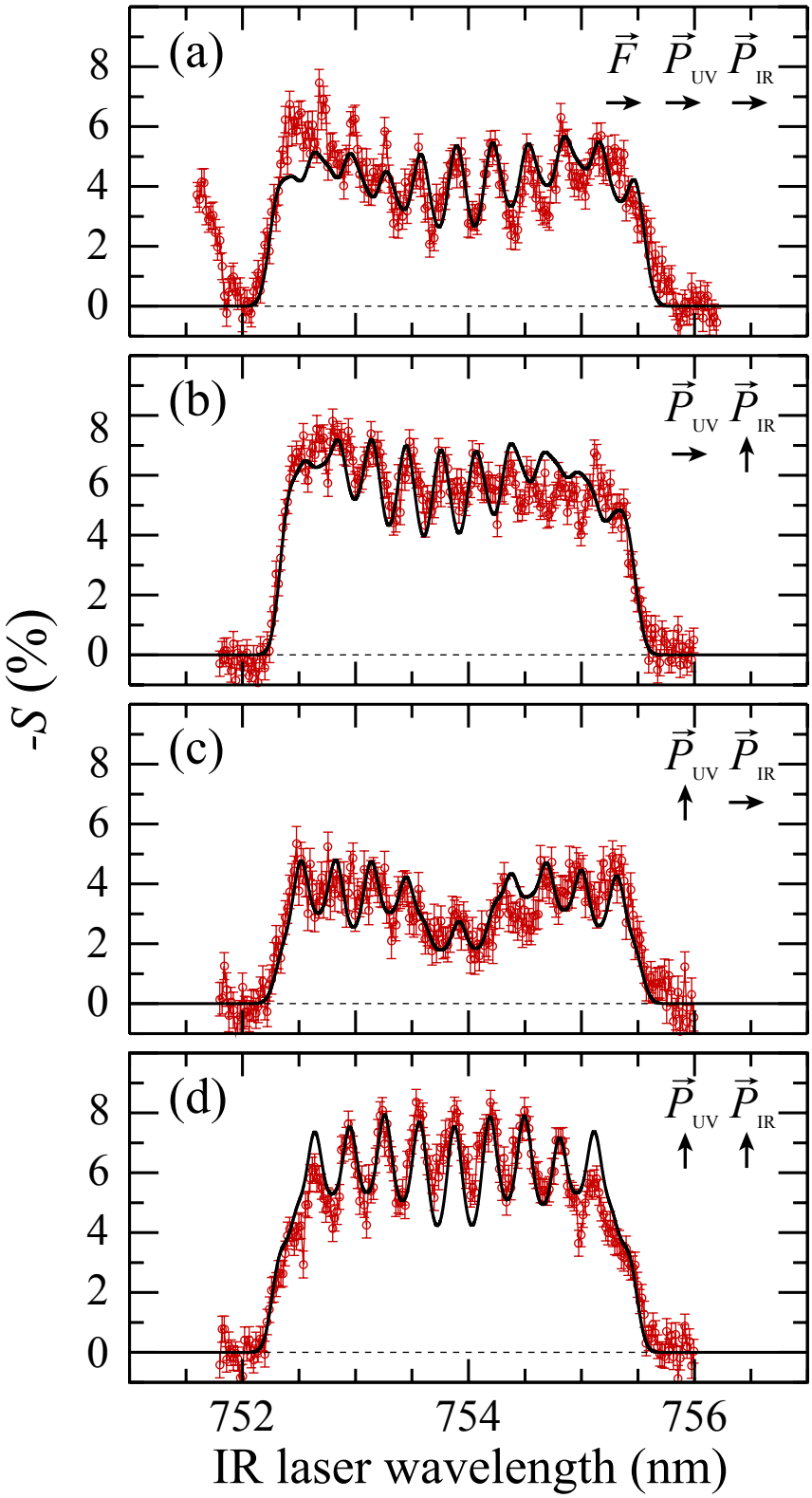

Figure 5.6: Measured (points) and calculated (lines) Rydberg Stark spectra of n = 11 Ps atoms in an electric field of 1.9kV/cm. The excitation was performed with different combinations of UV and IR laser polarizations P with respect to the electric field direction F, as indicated. In panel (a) the intrusion of neighboring n = 12 states (not included in the calculation) is seen below 752 nm. From [Wall *et al.* 2015].

Efficient production of Ps Rydberg states has been observed before [Cassidy *et al.* 2012a], this likely involves a mechanism wherein Ps Rydberg atoms are excited into states that cannot subsequently be pumped back to the $n = 2$ level, leading to an enhanced excitation efficiency, and even saturation, of Rydberg state production. This could occur, for example, via m changing collisions with secondary or photo-electrons. There are no data in the literature concerning electron interactions with Ps in Rydberg states, but it is well known that the cross sections for state-changing collisions between Rydberg atoms and charged particles can be very large [Gallagher 1994]. Whether such collisions take place or not could be investigated by directly measuring Ps lifetimes in beams or traps, as they would be

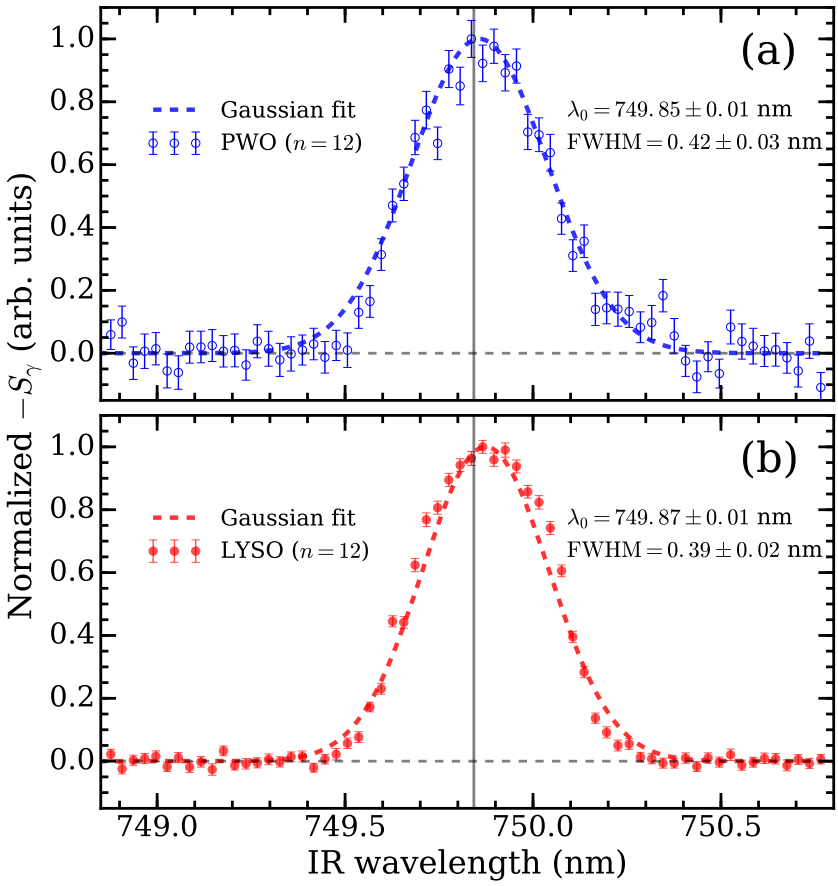

Figure 5.7: Lineshape for $n = 12$ Ps excitation, recorded with LYSO and PWO detectors. The acquisition time was 400 seconds per point, or approximately 7 hours for the entire spectra. These data have been normalized to the maximum peak amplitude. The vertical line represents the wavelength of the transition from the $n = 2$ gross energy level as described by the Bohr model. From [Alonso *et al.* 2016a].

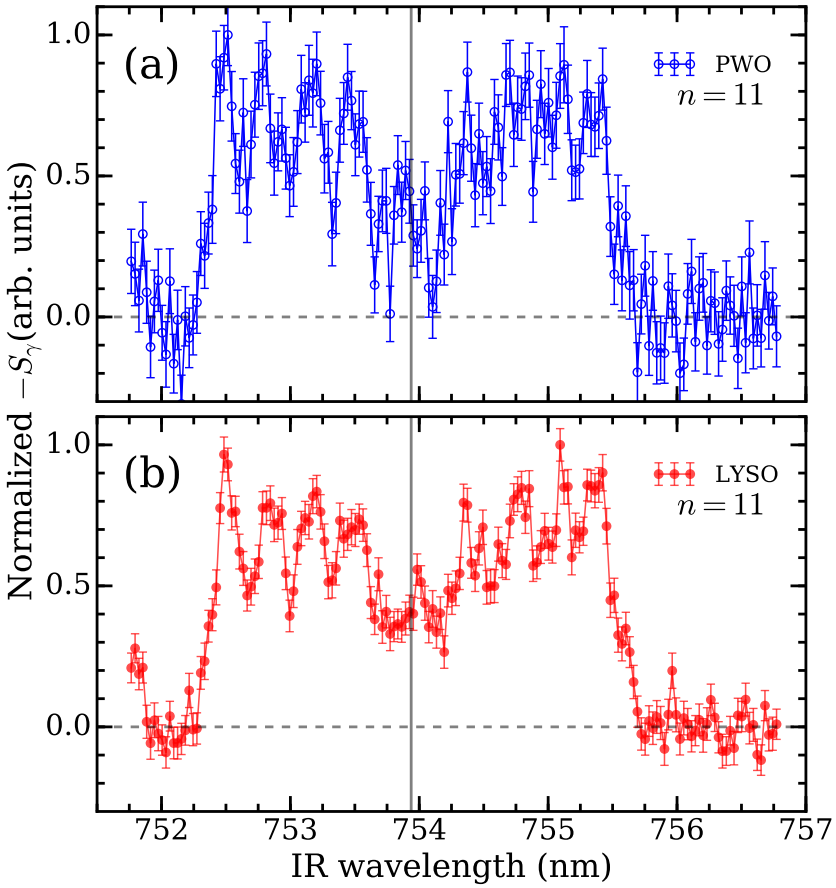

Figure 5.8: Stark broadened lineshapes for $n = 11$ Ps excitation, recorded with (a) PWO and (b) LYSO detectors in an electric field of 1.875 kV cm^{-1}. The acquisition time was 200 seconds per point, or approximately 9 hours for the entire spectra. These data have been normalized to the maximum peak amplitude. The vertical line represents the wavelength of the transition from the $n = 2$ gross energy level as described by the Bohr model. From [Alonso *et al.* 2016a].

increased significantly if higher angular momentum states are produced.

Future refinements of the positron beam may also make it possible to use a Doppler free two-photon excitation scheme [Wall *et al.* 2014], which would provide improved resolution, and hence state selectivity, at higher values of n.

Chapter 6

Spatial manipulation of Rydberg positronium

The experiments and results discussed in this chapter have been previously published in several articles, and as such, much of the content and figures used here were taken from these publications. Contents from this chapter describing our ability to manipulate the motion of Rydberg Ps with different designs of quadrupole guides have been published in the following articles:

- A. Deller, A. M. Alonso, B. S. Cooper, S. D. Hogan, and D. B. Cassidy. *Electrostatically Guided Rydberg Positronium.* Phys. Rev. Lett., **117**, 073202 (2016). doi: 10.1103/PhysRevLett.117.073202.

- A. M. Alonso, B. S. Cooper, A. Deller, L. Gurung, S. D. Hogan, and D. B. Cassidy. *Velocity selection of Rydberg positronium using a curved electrostatic guide.* Phys. Rev. A, **95**, 053409 (2017). doi: 10.1103/PhysRevA.95.053409.

6.1 Generating a quadrupole field

The increased lifetimes and enhanced electric dipole moment of atoms in Rydberg states have been used in the past to manipulate the motion of several species using inhomogeneous electric fields [Hogan & Merkt 2008, Townsend *et al.* 2001, Wing 1980, Breeden & Metcalf 1981] over long time scales. Variations of such techniques have been used for decades [Bennewitz *et al.* 1955] to manipulate ground-state polar molecules [van de Meerakker *et al.* 2012, Fulton *et al.* 2006] as well as atoms and molecules in Rydberg states [Hogan 2016], and other methods such as traveling optical latices to manipulate the motion of ground state atoms [Barker & Shneider 2001, Barker & Charlton 2012]. Most experiments that have previously demonstrated manipulation of atoms and molecules due to their electric dipole moment made use of supersonic jet expansions, which provides a very efficient form of cooling during the expansion phase due to collisions between the atoms/molecules. This is not the case for our Ps experiments, as the typical densities in our experiments are not large enough for significant Ps-Ps interactions [Cassidy & Mills 2008]. Manipulation of Rydberg atoms has been achieved using relatively large electrode structures [Seiler *et al.* 2011b] and more refined chip-based techniques [Hogan *et al.* 2012].

In this chapter we outline our results for the implementation of some of these techniques to Rydberg Ps, specifically, using quadrupole electric fields generated by four electrode structures to radially confine Ps atoms and guide them [Deller *et al.* 2016a, Alonso *et al.* 2017a].

The Ps atoms were created in an electric field to facilitate selective excitation of specific parts of the Stark manifold (see chapter 5). After entering the guide, atoms in states with positive Stark shifts [i.e., low-field-seeking (lfs) Stark states] are deflected away from the electrodes by the inhomogeneous electric fields [Townsend *et al.* 2001], and are thus guided along the length of the device. Atoms in states with negative Stark shifts [i.e., high-field-seeking (hfs) Stark states] are deflected away from the axis of the guide and are lost.

The Ps excitation region and the quadrupole guide structure and electric fields

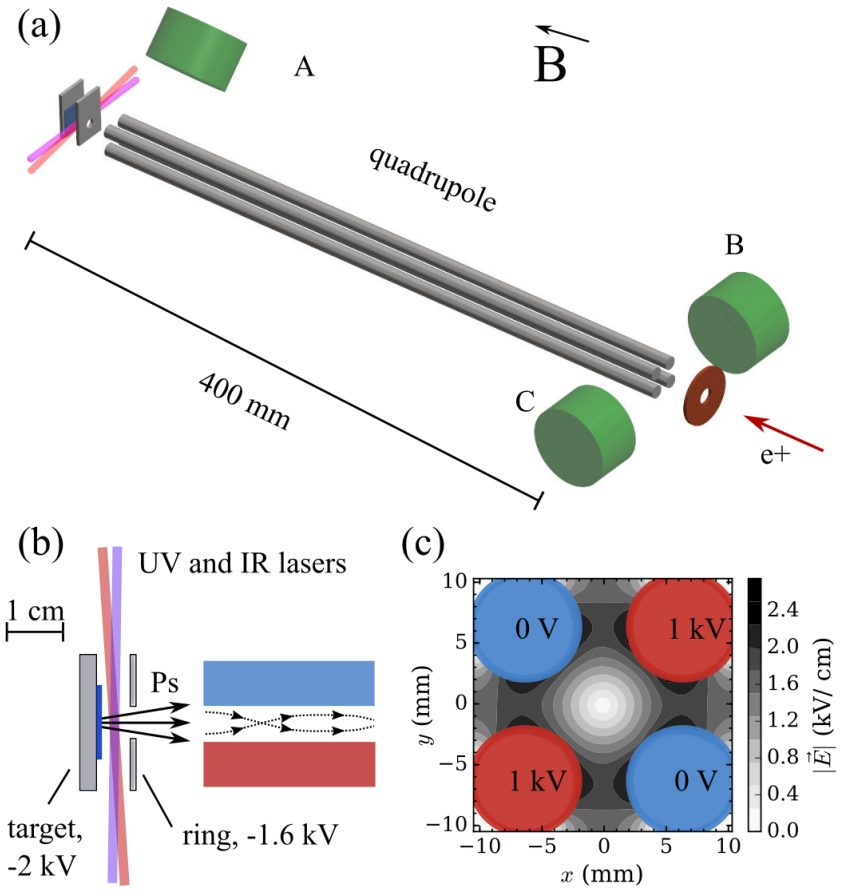

Figure 6.1: (a) Schematic layout of the experiment, indicating the Ps excitation region, the position of the quadrupole guide, and the LYSO gamma-ray detectors *A*, *B*, and *C*. (b) Expanded view of the excitation region, and (c) a contour plot of the electric field strength inside the quadrupole with 1 kV applied. From [Deller *et al.* 2016a].

are shown schematically in figure 6.1. Because Ps is produced in a reflection geometry, the guide potentials are switched on 150 ns after the positron beam has passed through using the methods described in section 2.5. Ps atoms are excited by the UV and IR lasers and travel towards the guide, reaching the entrance in ∼200 ns. As indicated in figure 6.1(b), the path from the silica target to the guide is partially collimated by a 5.8 mm diameter hole in a ring electrode, located 6.0 mm from the target, this is slightly different from most of our other experiments which had a "grid" electrode here instead (see section 2.7). Also shown in figure 6.1 are the positions of three LYSO detectors. The first detector (*A*) covers the target area and is used to monitor Ps formation and excitation, while Ps atoms that leave the exci-

tation region are detected by two more detectors (*B* and *C*) located approximately 0.4 m away.

6.2 Guiding positronium in a straight guide

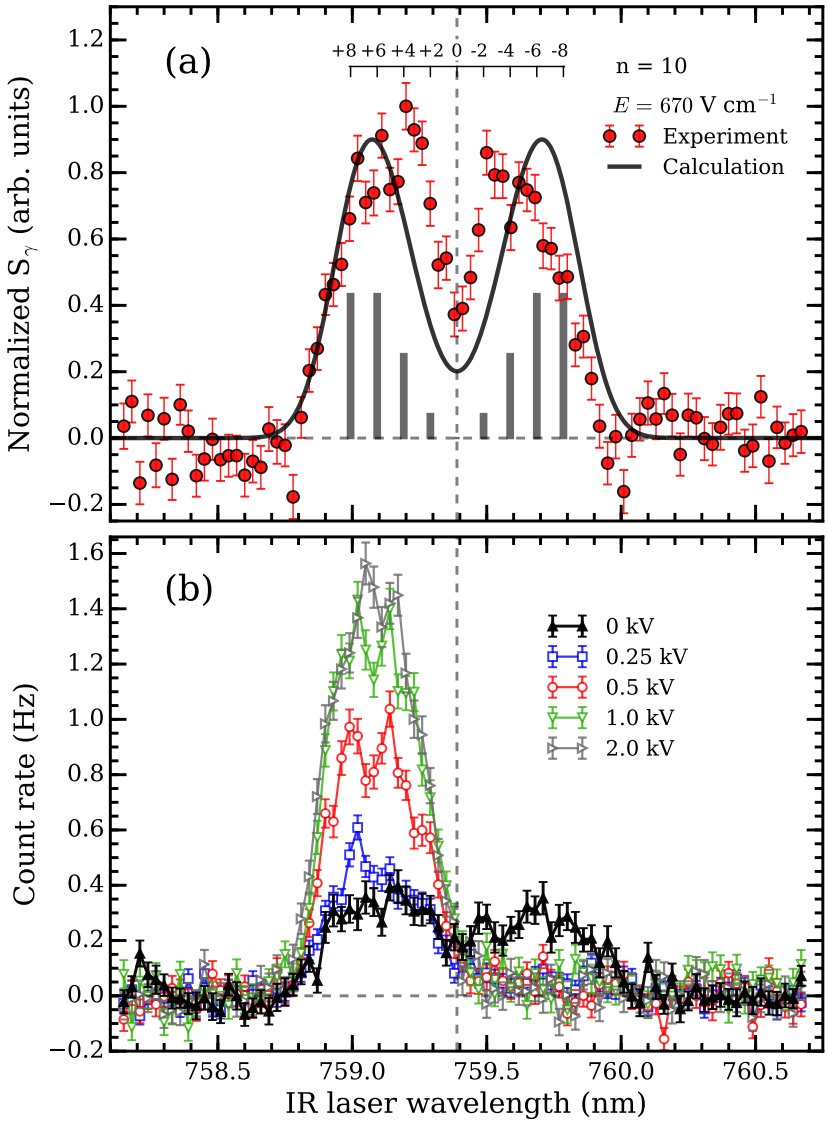

Figure 6.2: (a) Spectrum of the $n = 2 \rightarrow 10$ transitions measured using detector A. The grey vertical bars represent the relative spectral intensity for individual k states, labeled by the horizontal scale. The black solid line is a convolution of these with the ∼130 GHz experimental spectral resolution. (b) The background subtracted count rate obtained from detectors *B* and *C*, measured with the indicated potentials applied to the guide. The dashed vertical line in both panels represents the expected centroid wavelength for $n = 10$. From [Deller *et al.* 2016a].

In order to separate the Rydberg-Stark states, an electric field of 670 V cm^{-1}

was applied in the excitation region , and the resulting Stark-broadened spectrum of transitions from $n = 2$ to $n = 10$ is shown in figure 6.2(a). These data were obtained via SSPALS methods using detector A. There is a slight difference in the detection efficiency of lfs and hfs states because they are deflected by the inhomogeneous electric fields between the ring and guide electrodes. As a result, the measured spectrum is not perfectly symmetric. The applied field is not sufficient to permit the spectral resolution of individual Stark states (compared to figure 5.6, for example), but it is sufficient to allow for the optical selection of predominantly lfs or hfs states.

The IR and UV laser polarizations employed here were horizontal and vertical respectively, corresponding to data displayed in figure 5.6(c). The calculated relative spectral intensities [Hogan 2013] of the transitions to the nD components of the $m = 1$ Stark states are indicated by the vertical bars in figure 6.2(a). The solid black line is a convolution of the calculated intensity distribution with a 130 GHz Gaussian function, representing the experimental spectral resolution due to the laser bandwidth and Doppler broadening.

Enhanced Ps transport along the guide is indicated by an increased count rate in detectors B and C. Single event counting is used to detect atoms that travel away from this region (see section 2.4). For this particular set of data, detectors B and C were used, it is estimated that the detector efficiency including the solid angle coverage is around 5%. Figure 6.2(b) shows the background subtracted total count rate from detectors B and C as a function of the IR laser wavelength, for a range of voltages applied to the guide. The background was measured with the IR laser off resonance. The data obtained with 0 V applied to the guide were recorded at the same time as the spectrum shown in figure 6.2(a). In this case we detect any Ps Stark states that are emitted towards the guide within a narrow cone with a half angle of approximately 1°.

When the guide fields are applied the signal detected by B and C depends strongly on the IR laser wavelength. No hfs states are detected, demonstrating that even for states with the smallest electric dipole moments (i.e., $k = -2$ states with $\mu = 150$ D) and for the lowest applied fields, the hfs states cannot traverse the guide.

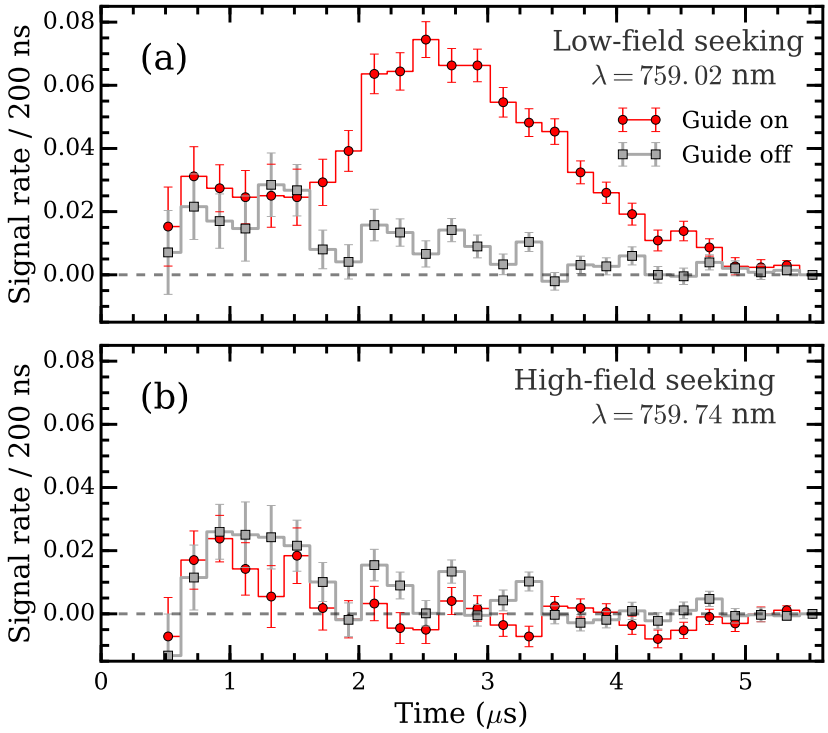

Figure 6.3: Background subtracted TOF data recorded by detectors *B* and *C* with 1 kV applied to the guide electrodes, for IR laser wavelengths corresponding to (a) outer lfs ($k \sim +6$) and (b) outer hfs ($k \sim -6$) states, as indicated. The data set is truncated for times less than $\sim 0.5\mu$s because of detector saturation following implantation of the positron pulse. From [Deller *et al.* 2016a].

The maximum applied potential results in a maximum electric field of 4.2 kV cm^{-1}, which is well below the lowest field required to ionize $n = 10$ ($\sim$14 kV cm^{-1}, see section 3.2)

For a low guide field only those states with the highest dipole moment (i.e., $k = +8$ states with $\mu = 610$ D) are observed above the guide off background signal. Nevertheless, this field is sufficient to suppress transport of all hfs states. When the field is increased, more of the lfs Stark states are transported, which may be partially due to a focusing effect in the space between the ring and guide electrodes and due Ps atoms traveling at larger speeds being able to be guided. The TOF distributions of the guided atoms have been directly measured for two different IR wavelengths, for which either lfs ($k \sim +6$) or hfs ($k \sim -6$) Stark states were predominantly prepared. These data are shown in figure 6.3. These TOF spectra are consistent with numerical

trajectory simulations which will be discussed in the section 6.4.

6.3 Velocity selection of guided positronium

After achieving radial confinement of Rydberg positronium with a straight guide, a curved version of the quadrupole was constructed and implemented to perform velocity selection and separate the guided Rydberg Ps beam from the positron beam. This will allow future scattering experiments to take place at the end of the guide. This type of curved guiding structure has been widely used in experiments with polar molecules [Rangwala *et al.* 2003, Motsch *et al.* 2009, van Buuren *et al.* 2009, Bertsche & Osterwalder 2010, Sommer *et al.* 2010]. The setup used is depicted in figure. 6.4, where it can be seen that the curved guide had a 45° bend and detectors were placed near the production region (D1 & D2), near the bend (D3), and after the exit of the guide (D4 & D5).

Rydberg Ps atoms were prepared both with and without a uniform electric field present (by changing the voltage difference between the grid and the target, see figure 2.11). The corresponding lineshapes, measured using D2, for the $2\,^3\mathrm{P} \rightarrow 14\,^3\mathrm{S}/14\,^3\mathrm{D}$ transitions are shown in figure 6.5(a). The Stark-broadened transition allows us to tune the laser wavelength to preferentially excite lfs states as discussed in section 5. This is not possible if the excitation is performed with zero applied field because we have insufficient spectral resolution (owing primarily to the laser bandwidth and Doppler broadening) to address only the part of the Stark manifold containing the desired lfs states. These states still exist even when no field is applied as a result of the magnetic field and stray electric fields in the excitation region.

Rydberg atoms that enter the quadrupole guide structure and are transported to the end are detected by D4 and D5 where a single-event counting procedure is performed (see section 2.4). The total event rate recorded during the lineshape measurements is shown in figure 6.5(b). Here we see that when lfs states are preferentially prepared, the event rate is much higher and occurs at a wavelength that is down-shifted from the resonant wavelength. These data show conclusively that it is more efficient to broaden the line and then tune the laser to the lfs side of the

spectrum, which is to be expected since we will not then produce any hfs states, which cannot be guided. This procedure will mostly result in the production of Rydberg-Stark states with values of the parabolic quantum number $k = +12$ and dipole moments of 1280 D (see section 3.2). The maximum electric field strength encountered in the guide is ≈ 7 kVcm^{-1}, which would result in field ionization rates of the $k = +12$ Stark-states of $\approx 10^9$ s^{-1} (see figure 3.6). However, simulations indicate that the Ps atoms do not spend much time in these field extrema.

TOF spectra of guided atoms recorded near the bend (by D3, see figure 6.4), and at the end of the guide (by D4 & D5) for different applied electric potentials are shown in figure 6.6. These spectra have been background subtracted, where the background corresponds to the case where no IR laser light is present. The data show that increasing the quadrupole field strength increases the overall guiding

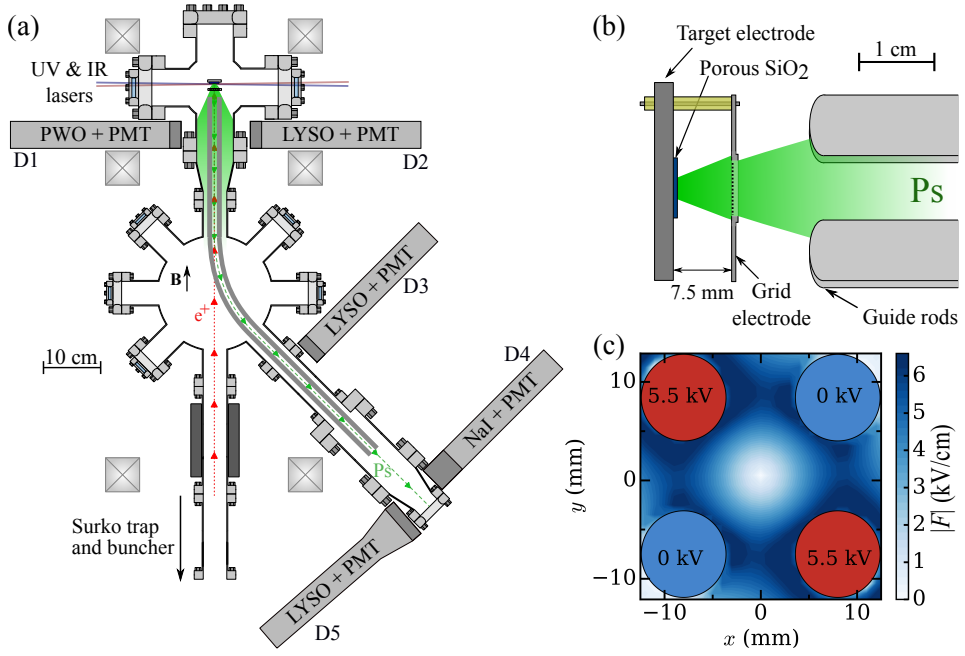

Figure 6.4: (a) Schematic representation of the experimental apparatus containing the curved guide. The positions of the five γ-ray detectors used in the experiment are indicated (see text for details). D1 and D2 are used to monitor Ps atoms in or near the excitation region via lifetime spectroscopy, whereas D3, D4, and D5 are used to generate single-event TOF spectra. (b) Close up of the excitation region indicating the Ps formation target and excitation region, and the position of the quadrupole guide rods relative to the grid electrode, and (c) electric field map within the guide with 5.5 kV applied to one pair of rods. From [Alonso *et al.* 2017a].

efficiency by capturing more of the Ps atoms. The count rate measured by D3 has a maximum value at intermediate guiding fields because D3 will predominantly detect atoms that are guided in the straight section, but are not transported around the bend.

We may evaluate the degree of velocity selection imposed by the curved guide by considering velocity distributions measured with and without guiding, as shown in figure 6.7. These distributions were derived from measured TOF distributions, with the data rebinned into equal sized (10 kms^{-1}) bins. The "no guide" data were

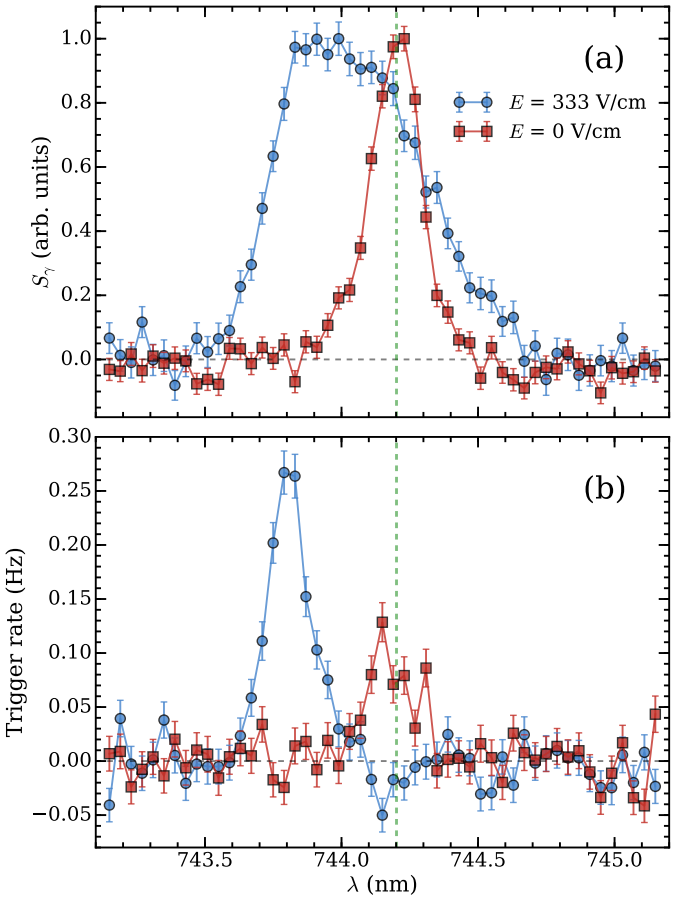

Figure 6.5: (a) Lineshapes for the $2^3\mathrm{P}_J \rightarrow 14^3\mathrm{S}/14^3\mathrm{D}$ transitions measured by D2 with and without a 333 V/cm linear electric field applied in the excitation region. The asymmetric lineshape measured with the electric field applied is due to deflection of atoms towards or away from D2. The data have been normalized to peak amplitude. (b) Total count rates for guided atoms as a function of the IR laser wavelength in the corresponding electric fields, measured by D4/5. The dashed vertical line represents the expected zero-field resonant wavelength, and the voltage applied to the guide was 5.5 kV. From [Alonso *et al.* 2017a].

recorded using $n = 20$ Ps atoms, measured 1.2 m away from the Ps production region (see section 5.1), and with a positron beam energy of 2 keV. In this configuration only atoms emitted in a small ($\sim 1^\circ$) cone were detected, and therefore atoms with the largest (smallest) longitudinal (radial) speeds were selected. A mean Ps speed of 115 kms^{-1} was measured near the Ps source region, while $\approx$ 225 kms^{-1} was measured 1.2 m away, as shown in figure 6.7. This spectrum represents an upper limit to the possible initial Ps distribution as accepted into the guiding structures since this represents the distribution without any velocity selection introduced by the acceptance of the guide.

Ps atoms transported by the straight guide are radially trapped (see section 6.1); this introduces some longitudinal velocity selection owing to the correlation between the longitudinal and transverse velocity components [Deller *et al.* 2015]. The straight guide distribution shown in figure 6.7 was obtained using a relatively low guiding field, which therefore selected slower atoms. This spectrum indicates a mean speed of 137 kms^{-1} and represents a lower limit to the possible initial Ps

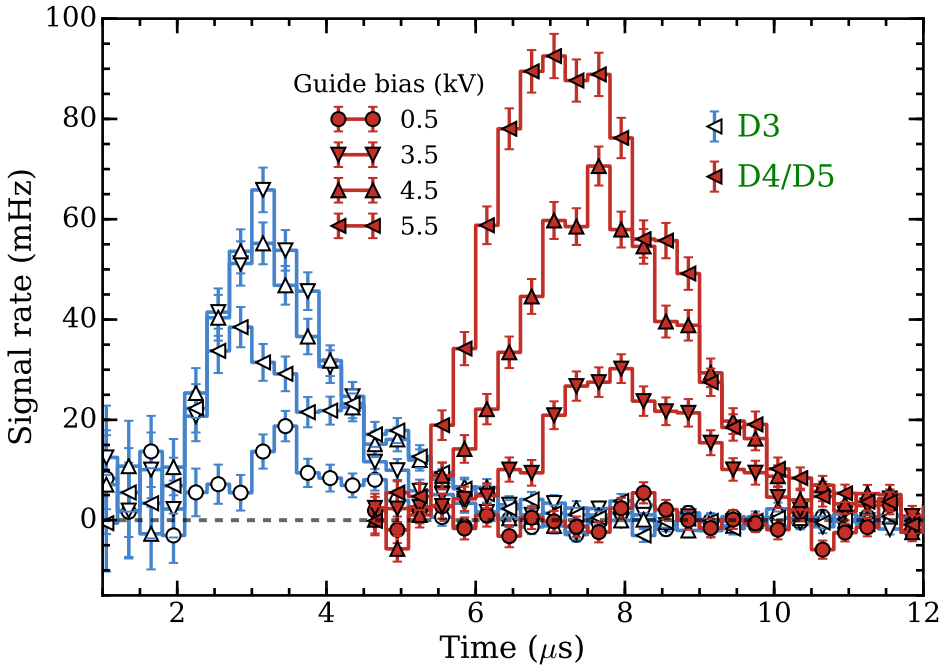

Figure 6.6: (a) TOF data measured using D3, and D4/5 for guide voltages of 0.5, 3.5, 4.5 and 5.5 kV, as indicated in the legend. Additional spectra (not shown) were recorded for guide voltages of 1.5, 2.5 and 5.0 kV and lfs Ps atoms with $n = 14$. Each curve was acquired in 4 h. From [Alonso *et al.* 2017a].

distribution at the guide entrance.

Thus, as a rough approximation, we can expect a representation of the initial Ps velocity distribution entering the curved guide to fall somewhere between the unguided and straight guide distributions shown in figure 6.7. The absolute number of atoms detected in each case depends on several factors, such as guide efficiency, beam collimation, Ps-guide alignment, and detector solid angle. These factors are not necessarily the same for all measurements, and the unguided case is of course intrinsically much less efficient. The distributions have been normalized to peak amplitude to facilitate comparison of the mean speeds, but the transport and detection efficiencies will be different in each case.

6.4 Trajectory simulations

Simulations of the motion of Ps atoms in Rydberg-Stark states in the electrostatic quadrupole field were carried out to help understand the experimental data, and

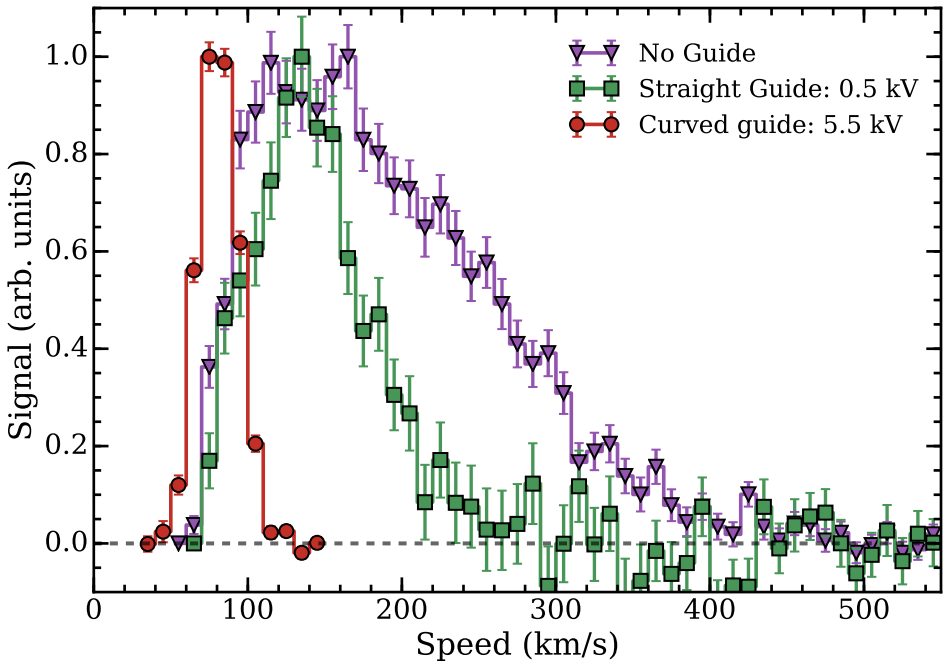

Figure 6.7: Longitudinal velocity distributions as derived from TOF measurements obtained with no guide (triangles, see section 5.1) , a straight guide (squares, see section 6.1) and with the curved guide (circles). The electric potential applied to the guide rods are indicated in the legend. The curved guide data is derived from the data shown in figure 6.6. TOF spectra were re-binned into 10 kms^{-1} steps to generate the velocity distributions. From [Alonso *et al.* 2017a].

also to examine the possibility of performing scattering measurements using guided Rydberg Ps. The equations of motion of Ps atoms in a quadrupole electric field were solved to find the Ps trajectories using the fourth-order Runge-Kutta algorithm [DeVries 2010], with the acceleration of each atom given by

$$\vec{a} = \frac{\mu_{\text{elec.}}}{2m_e}\nabla\vec{F}, \tag{6.1}$$

since the force in a dipole can be expressed as $\vec{f} = \nabla(\mu \cdot \vec{F})$ [Griffiths 2012]. Where μ represents the dipole, $\vec{f}$ the classical force exerted on the dipole, and $\vec{F}$ is the electric field vector. The electric field gradients were obtained using finite element calculations of the electric field distribution within the guide as shown in figure 6.8.

The trajectory calculation was seeded using a Monte-Carlo simulation of the initial Rydberg Ps velocity distribution. Ground-state Ps atoms were modeled as being emitted from the converter with a thermal speed distribution ($T = 1200$ K) and cosine angular distribution. Ps produced from porous silica films is not expected to exhibit a thermal distribution but previous measurements [Deller *et al.* 2015] have shown that the actual Ps distributions can be approximated with reasonable accuracy in this way using an arbitrary temperature value. The spectral overlap was determined by the laser bandwidth, $\Delta\nu = 100$ GHz, and the Doppler shift of each atom according to its velocity in the direction parallel to the propagation of the laser, v_x.

The Ps atom trajectories were calculated taking into account the electric field experienced by each atom and the corresponding ionization rate (see section 3.2) as well as the Ps fluorescence lifetimes. The latter were obtained from the calculated values described in [Deller *et al.* 2016b]. If an atom decayed, was field ionized, collided with a chamber wall, the grid, the target, or the guide electrodes, the trajectory was terminated. The Monte-Carlo simulations were run using 1000 particles and the results are shown in figure 6.8 for different guiding fields.

For the initial velocity distributions and the maximum guide voltages used in these experiments, the simulations indicate that $n = 14$ is the optimal guiding state as shown in figure 6.9, based on the guide efficiency and loss mechanisms (decay

and ionization). The data shown in figure 6.8 (d) show that at these fields Ps atoms that are not guided will be ionized before leaving the guide structure. The simulations indicate that higher n states can be guided in lower fields, although this is only possible if the excitation region field is turned off before the Ps atoms exit through the grid electrode (see section 4.2) to prevent field ionization.

Figure 6.10 shows a comparison of the measured event rate and calculated guiding efficiency, as well as the measured and calculated mean Ps speeds. We find a broad agreement over the range for which measurements were performed. The TOF distributions were fitted to Gaussian functions in order to estimate the mean Ps speeds, and we find reasonable agreement between the measurements and

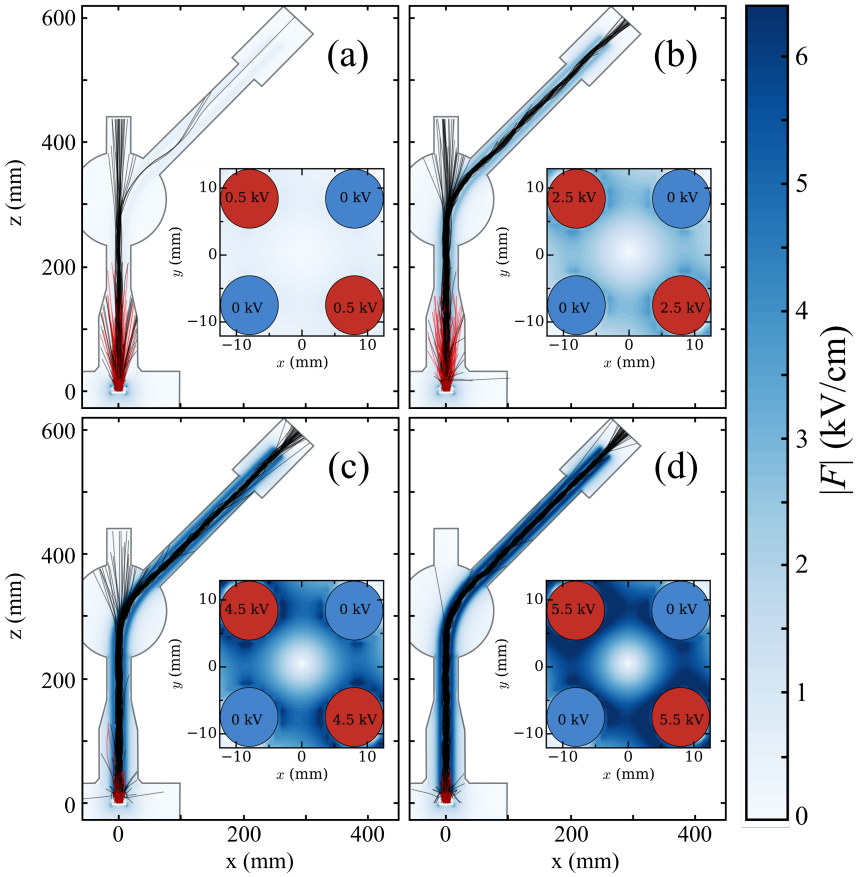

Figure 6.8: Simulated trajectories for guide biases of 0.5 (a), 2.5 (b), 4.5 (c), and 5.5 kV (d). The black lines represent atoms in the low-field-seeking state with $k = +12$, whereas the lighter (red) lines represent atoms in the high-field-seeking state with $k = 12$. Also shown in each panel is an inset of the electric field strength for each configuration, and an outline of the chamber walls representing the ground plane of the electric field. From [Alonso *et al.* 2017a].

simulations. These data indicate that by adjusting the guide field, the mean speed of atoms can be selected over a small range (approximately 75-90 kms^{-1}). However, this variation is small compared to the width of the velocity distribution, and is accompanied by a large reduction in the guiding efficiency.

The measured TOF distributions can be used to evaluate the efficacy with which our arrangement could be used to observe the formation of positron-atom bound states. To do this the attenuation of the measured Ps TOF distributions was simulated by including an interaction cross section, and assuming an atom was re-

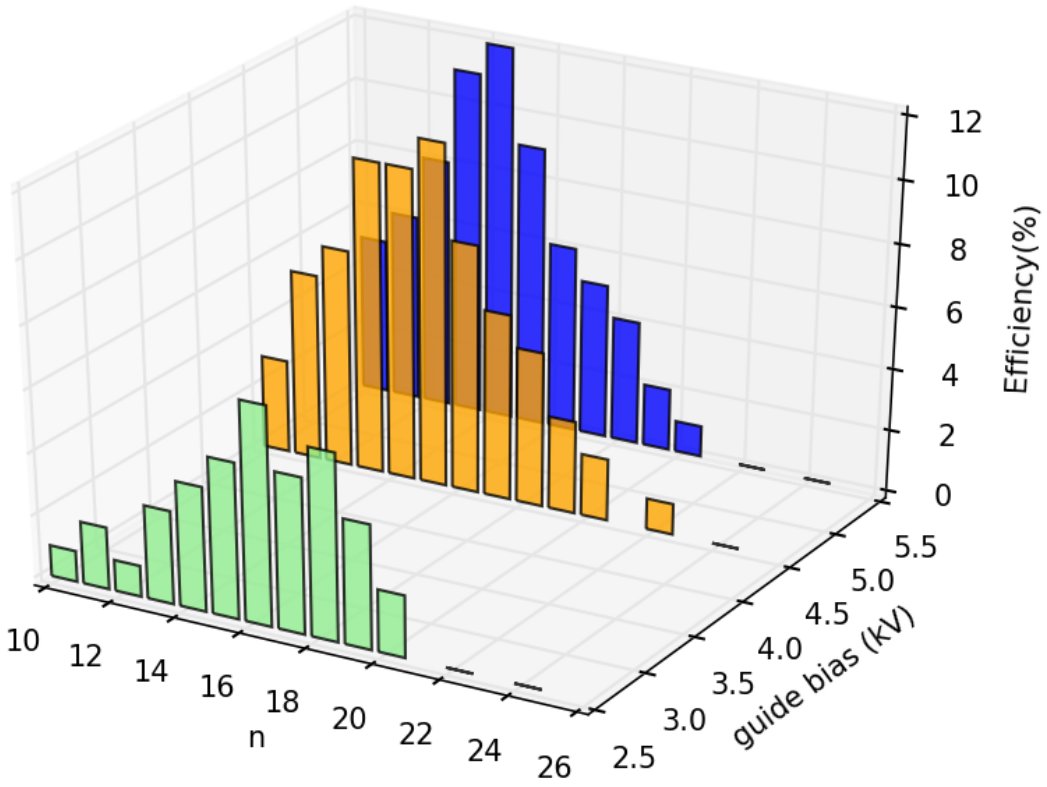

Figure 6.9: Simulated transport efficiency for a range of n from $n = 10$ to $n = 24$ for a range of curved guide biases. The higher the guide bias, the deeper the radial potential well for the Rydberg Ps atoms due to the dipole forces, and thus more of the fast-moving atoms may be trapped. However, large electric fields due to large biases may also lead to field ionization, which means that there is a limit to how large a field can be applied to a certain n state. But the classical field ionization for different n's scales as n^4 (see equation 5.1), and thus lower n's are more suitable to survive these large fields. All of this factors are taken into account in the simulation, and it can be seen that the best guiding efficiency attainable in this configuration is at the largest guiding bias that the high voltage switches can apply ($\sim$5.5 kV/cm), and when $n = 14$.

moved from the system if a scattering event occurred. The cross sections used were those calculated for positrons binding to Zn atoms [Swann *et al.* 2016], and are shown in figure 6.11(a). Zn atoms were chosen because they have the largest calculated cross sections out of all the species considered in [Swann *et al.* 2016]. The simulated attenuation of the Ps distribution is shown in figure 6.11(b) for different Zn pressures at a temperature of 485 K. The trajectories shown in figure 6.8(d) were used as the basis for Ps-atom interactions in a 3.5 cm long scattering region that encompassed the entire radial extent of the beam. The velocity of each particle was obtained from a weighed distribution based on the measured data shown in figure 6.6, and the interaction rate per particle in the simulation (Γ) was given by

$$\Gamma = \sigma(v)\rho \mathrm{d}L/\mathrm{d}t, \tag{6.2}$$

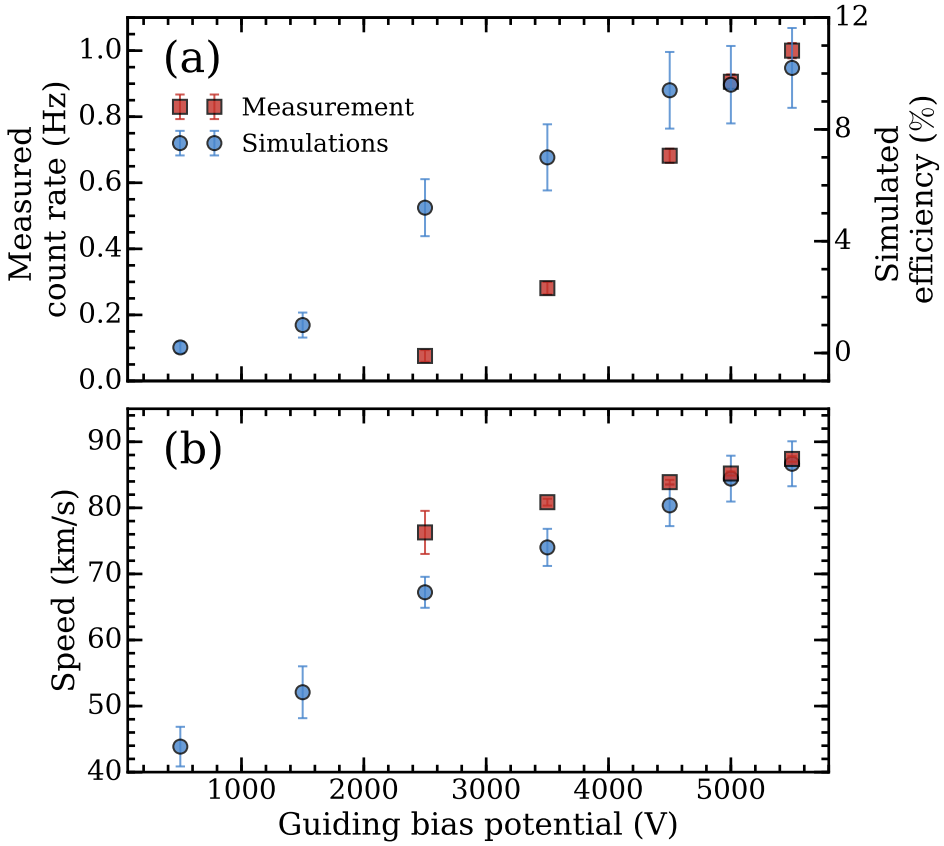

Figure 6.10: Measured count rate and simulated guiding efficiency (a) and mean Ps velocities derived from the TOF data and simulations (b) for different voltages applied to the quadrupole rods. From [Alonso *et al.* 2017a].

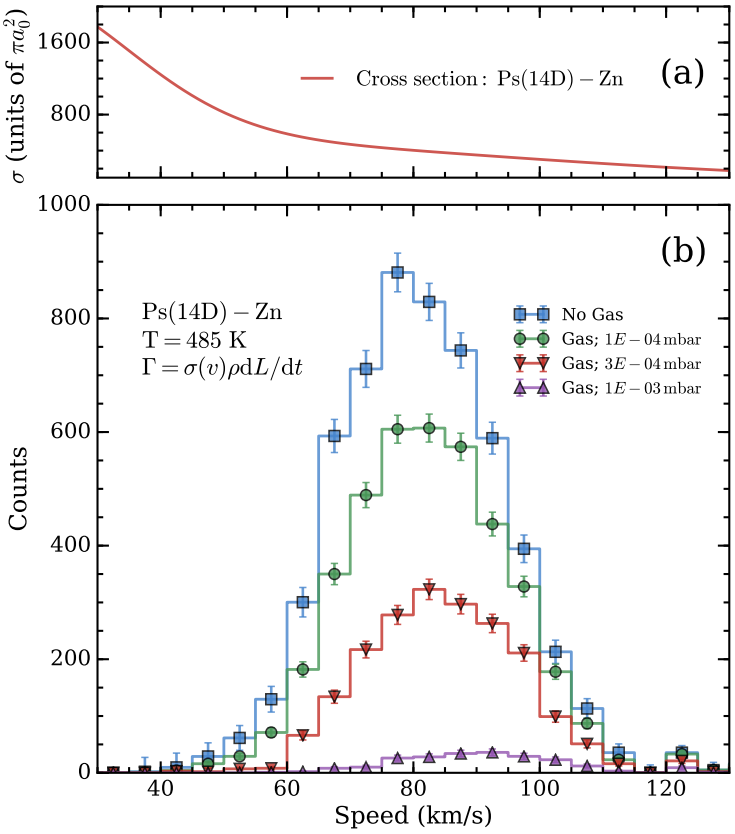

Figure 6.11: (a) Calculated cross section σ for positron-atom bound state formation in collisions of $n = 14$ Ps atoms with Zn atoms and (b) simulated data indicating how the observed velocity distribution would be attenuated by Ps charge exchange reactions with Zn at the indicated pressures. The measured TOF distribution has been re-binned into 5 kms^{-1} steps to generate the velocity distribution. From [Alonso *et al.* 2017a].

where ρ is the target species number density, dL is the distance traveled in each time step dt, and $\sigma(v)$ is the relevant cross section as a function of speed, obtained from [Swann *et al.* 2016], and shown in figure 6.11(a). For each particle whether an event had occurred or not was determined by comparing the calculated probability with a randomly generated number between 0 and 1. The simulations were run with 5865 particles for each pressure shown in figure 6.11. We note that the cross sections used in the simulations were calculated for Ps Rydberg levels with specific angular momentum ℓ values (in this case, D states), whereas experimentally we expect to produce only Rydberg-Stark states (i.e., states that are strongly ℓ-mixed) [Deller *et al.* 2016b]. However, test calculations designed to estimate the likely cross section ℓ dependence indicate that below energies of 1 eV it is relatively

weak [Swann *et al.* 2016]. Nevertheless, this determination of possible positron-atom bound state production rates should be considered only as an order of magnitude estimate.

Figure 6.11 shows the simulated attenuation of the Ps distribution for different Zn gas pressures in the scattering region. These data indicate that a clearly discernible signal could be achieved, but that it would require Zn pressures close to 1×10^{-4} mbar, unless slower Ps atoms can be employed. Such pressures can be achieved by heating Zn to temperatures $\gtrsim$ 500 K [Greenbank & Argent 1965]. Although there are some experimental challenges associated with producing hot metal vapors it can be achieved by integrating a hot cell into our system (e.g., [Anderson *et al.* 2014]). If this can be successfully accomplished with Zn then our simulations indicate that a measurement of positron-atom binding is in principle feasible using this Rydberg Ps source.

From a practical point of view, this velocity selection method is convenient in that it can remove the Ps beam from the trap axis, allowing for improved separation of the detection and production regions. A rotated Ps formation target can also be used to achieve this goal (e.g., [Jones *et al.* 2014]), but at the cost of increasing the effective positron beam spot size, and hence the spatial extent of the Ps source. Alternatively one can bend the incident positron beam using magnetic fields (e.g., setup used to acquired the data in figure 5.2), although this can make the beam alignment more complicated. Moreover, both of these methods retain a direct line of sight between the excitation and detection regions, which for some experimental arrangements could be undesirable; for example, scattered laser light may reach the interaction region and interact with sensitive micro-channel plate detectors [Jones *et al.* 2016], or the Ps formation target may become contaminated by scattering-target gases.

Chapter 7

Future prospects and conclusions

7.1 Trapping Rydberg positronium

There have been many previous studies that made use of the large static dipole moments of Rydberg-Stark states to perform three dimensional trapping of atoms [Vliegen *et al.* 2007, Hogan & Merkt 2008, Seiler *et al.* 2011b, Seiler *et al.* 2012, Hogan *et al.* 2013, Lancuba & Hogan 2016] and molecules [Hogan *et al.* 2009, Seiler *et al.* 2011a, Seiler *et al.* 2012]. This possibility has also been investigated throughout the course of this project by performing trajectory simulations similar to the ones described in section 6.4 and therefore we would like to now apply these methods to decelerate and trap Ps.

A simple configuration of electrodes was found to be a potential candidate for this future experiment, the result of these simulations at four different stages of trapping are shown in figure 7.1. The black bars labeled A, B, C, and D are all square 40×40 mm electrodes, B and D both have transmissive meshes that allow Ps atoms to travel through them, while C has a central 13 mm hole where the trapped atoms oscillate around their equilibrium position. The voltage applied to all four electrodes must be controlled independently during each time-step in the simulation.

In order to obtain these trajectories initially 5000 Ps atoms were generated using Monte-Carlo methods to determine their initial velocity spread using a Maxwell Boltzmann distribution which was then truncated at low energies to account for the quantum confinement energy of the pores [Cassidy *et al.* 2010a]. The resulting

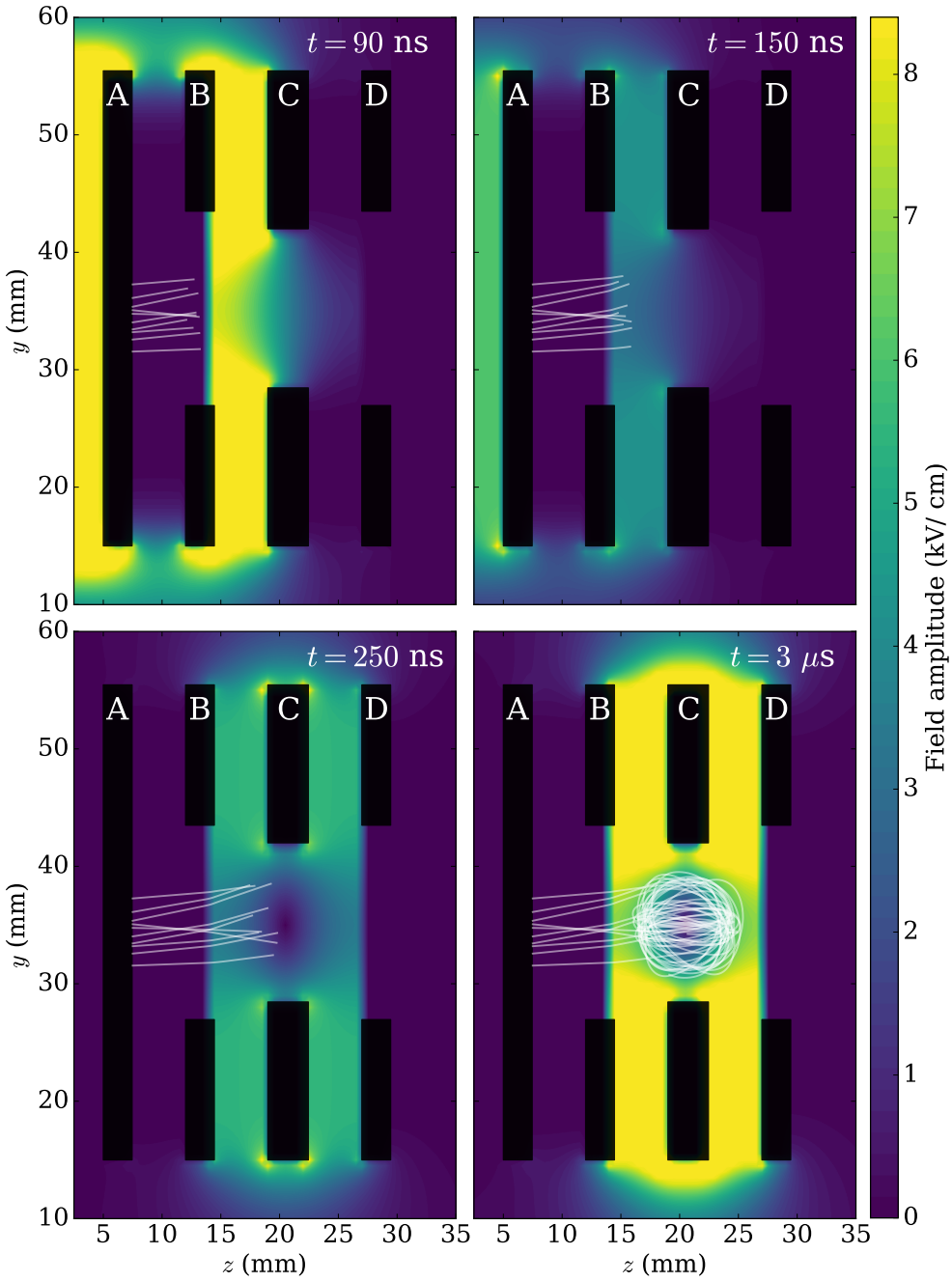

Figure 7.1: Simulated trajectories of 10 Ps atoms in $n = 13, k = +11$, initially traveling with perpendicular velocities of ∼60 km/s (kinetic energies of ∼33 meV). The black bars represent a cross section of the electrodes, A is the target electrode, B and D are both electrodes with a transmissive circular mesh similar to the ones shown in figure 6.4(b), and C is a 3 mm thick square electrode with a 13 mm hole in the center, which acts as the center of the trap. The time since laser excitation is shown in the top right of each panel. The white lines denote the trajectories of each atom backtracking to $t = 0$, the color scale represents the electric fields generated by the electrodes, the scale is truncated at 8.3 kV/cm where the field-ionization rate for $n = 13, k = +11$ exceeds 10^8 s^{-1}.

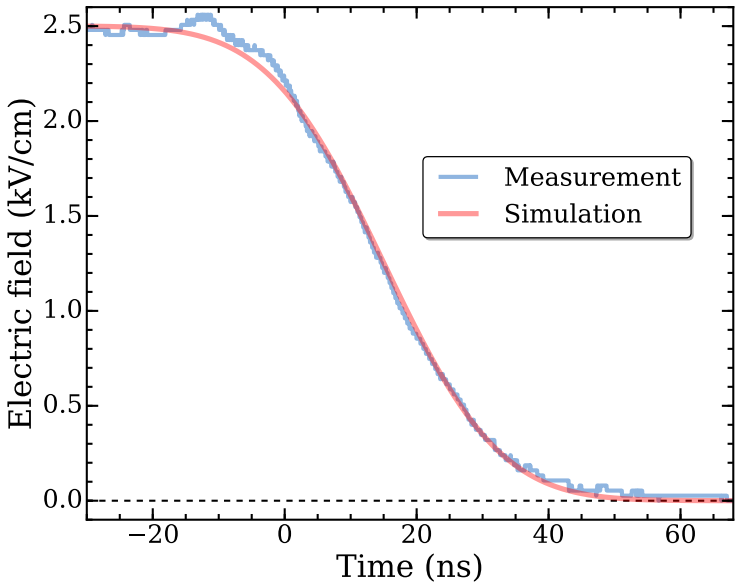

Figure 7.2: Measured switching time on a target electrode using a high voltage probe (as shown before in figure 2.24) and simulated switching field used to calculate trapping trajectories for Rydberg positronium as shown in figure 7.1, the simulated voltage is given by equation 7.1.

velocity distribution was made to match our TOF results shown in figure 6.7.

Positronium atoms were generated in the $n = 13$, $k = +11$, $|m| = 1$ state, and their trajectories were calculated as described in section 6.4, The time profile of each electrode when the voltage is being switched was modeled as a modified error function given by

$$\mathrm{erf}(x) = \frac{2}{\sqrt{\pi}} \int_0^x e^{\frac{-(t-t_0)^2}{\left(\frac{\tau_{sw}}{4\sqrt{\ln(2)}}\right)^2}} dt, \tag{7.1}$$

where t_0 is the time at which the switch is triggered, τ_{sw} is the full rise time of the high voltage switches that we use in our experiments and in this case it was fixed to 50 ns (as can be seen in figure 2.24), then the error function was shifted and scaled accordingly to match the simulated applied voltage to the electrode in question. Figure 7.2 shows the simulated switching field due to one of the electrodes and the corresponding measurement for such field, demonstrating that the fields applied in the simulations shown in figure 7.1 are attainable in the current experimental arrangement.

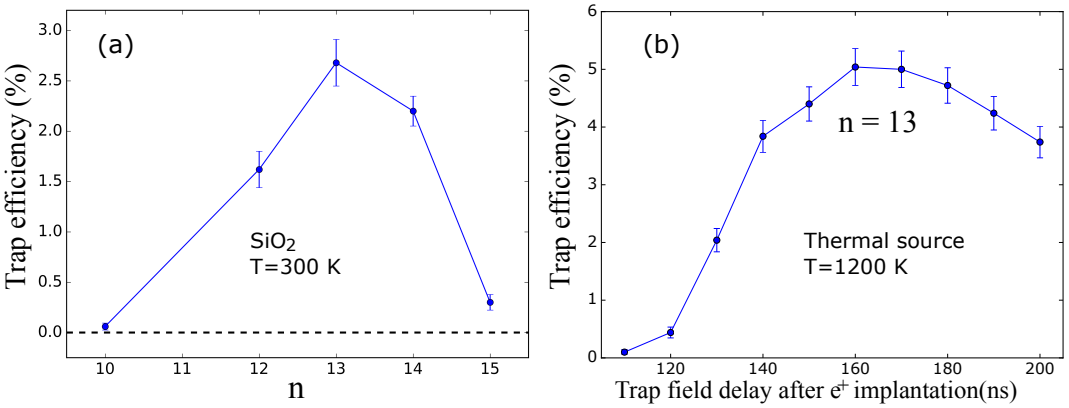

Figure 7.3: (a) Simulated trap efficiency for different n states using a truncated distribution as mentioned in the text, the optimum n is found to be 13. (b) optimization of the trapping field switching time for a thermal distribution of Ps atoms (such as the one obtained from hot metals) showing that there would be a wide range of times where the trapping deficiency could exceed 5%.

The results shown in figure 7.1 show both deceleration and trapping, this is achieved by turning off the field once the atoms have transferred some of their kinetic energy into potential energy by entering a large electric field region. In this case this happens between the first and second panel in figure 7.1 where the voltage applied to electrodes A and B is decreased from 5.5kV to 0 V, then the voltage applied to C is increased from 0 V to 5.5kV forming the electric field minimum seen in the last two panels. The voltage applied to D is always 0 V.

In this electrode configuration the simulations suggest that we should be able to extract $\sim$12 meV of energy from a portion of $n = 13$ atoms (as shown in figure 7.3(a), $n = 13$ would be the most efficient n to be guided), leading to a trapping efficiency of $\sim 2.7\%$. It is also worth noting that another version of these simulations was performed in which we made use of a 1200 K beam Maxwell Boltzmann distribution without truncation at low energies due to quantum confinement, these distributions would be attainable by using hot metal targets which produce thermal Ps [Mills 1979], if we could use this type of targets instead of SiO_2, the simulations suggest that we could achieve efficiencies of up to 5% [as shown in figure 7.3(b)], this possibility is also currently being investigated, however preparing metal film targets usually require very stable vacuum conditions, and an alternative option of metal "beads" is being considered [Voigtlnder *et al.* 2008].

We found that for our experimental limitations, including voltage switching time τ_{sw}, maximum switching voltage, and small percentage of low-energy atoms, $n = 13$, $k = +12$ would be the most efficient state to trap, since higher states have lower ionization energies, and thus will always have less energy extracted before ionizing, and lower states require fields that we cannot easily achieve with our current electronics, and they would have significantly lower fluorescence lifetimes.

7.2 Positron-atom bound states and Rydberg scattering

The feasibility of producing positron-atom bound states by means of Rydberg positronium scattering has been investigated in section 6.4, the simulations shown in figure 6.11 suggest that his can be done with with pressures (of atomic Zn gas) as low as $\sim 1 \times 10^{-4}$ mbar at approximately $T = 485$K. There are many theoretical predictions for the existence of these states [Mitroy *et al.* 2002, Cheng *et al.* 2011, Harabati *et al.* 2014] but they have never been realized experimentally, however it has indeed been predicted that our Rydberg Ps beam would be suitable for this experiment [Swann *et al.* 2016]. This measurement would involve using a hot vapor cell with an aperture through which Rydberg Ps could traverse, and a simple attenuation measurement measured by an MCP could be performed. This arrangement could also be modified to perform measurements of scattering rates of Rydberg Ps with neutral atoms and molecules [Hotop & Niehaus 1968]. It would also be possible to perform merged beams experiments [Osterwalder 2015, Gordon & Osterwalder 2017] which would significantly increase the cross sections measured since the relative velocities between particles would be greatly reduced.

7.3 Gravity measurements

It has been proposed that a free-fall measurement of Ps could be performed in order to measure the coupling of antimatter to gravity [Cassidy & Hogan 2014, Mills & Leventhal 2002] (the same has also been proposed for anti-hydrogen [Charlton *et al.* 1994]). Our current setup with the curved guide as described in sec-

tion 6.3 provides a collimated beam of Ps atoms with some control over their velocities, and some additional focusing (similar to [Jones *et al.* 2017]) and cooling of the Ps beam, perhaps by using cryogenic targets may eventually lead to a suitable source for performing such a free fall experiment. There has already been a proof-of principle measurement by the ALPHA collaboration [ALPHA Collaboration 2013] consisting of releasing trapped antihydrogen atoms from their trap, which has placed upper bounds to this possible measurement (i.e., gravitational to inertial mass ratios larger than 75 may be rejected with 5% statistical confidence).

However, it is far more likely that if an accurate antimatter gravity experiment is to be performed, the more reliable method is likely to be atom interferometry [Kasevich & Chu 1991] as opposed to a free-fall experiment. A free fall experiment is unlikely to achieve the level of accuracy that would be needed to detect a small deviation from the expected free-fall, and it is difficult to scale up. Interferometric measurements have been successful at accurately measuring the gravitational constant [Biedermann *et al.* 2015].

It may be possible to perform interferometric measurements with Rydberg Ps, however, the susceptibility of Rydberg states to electric fields may be incompatible with accurate interferometric measurements, since they would be likely to be deflected due to their large dipole moment, or field ionized. However if they are prepared in a circular state, with no dipole moment, these problems may be mitigated.

7.4 Precision spectroscopy

In all the experiments described here the electric field in the laser excitation region is known to within $\sim$1 V/cm, and in some cases the inhomogeneity of the field can only be estimated through simulations, not directly measured. If the electric field could be accurately measured and consequently we could apply field cancellation techniques, our arrangement could be used to perform microwave spectroscopy between neighboring n states. This could lead to a new measurement of the Rydberg constant in which the Lamb shift does not include the proton

charge distribution. This is relevant to the "proton radius puzzle", a current disagreement in the measured proton charge radius [Pohl *et al.* 2013] between measurements performed with muonic hydrogen [Pohl *et al.* 2010] and other measurements of the charge radius, including spectroscopic measurements of hydrogen [de Beauvoir *et al.* 1997, Schwob *et al.* 1999, Parthey *et al.* 2011], electron scattering, [Zhan *et al.* 2011, A1 Collaboration 2010], and the combination of the last two methods into the accepted value of the proton charge radius [Mohr *et al.* 2016]. The measurement for muonic hydrogen disagrees with all of these measurements (except for a recent spectroscopy measurement of hydrogen [Beyer *et al.* 2017] which identified a series of systematic errors, and after accounting for these, their measurement agrees with the muonic hydrogen value, although the uncertainty of this value is $\sim$14 times less precise than the muonic hydrogen experiments).

The transition frequency between two states depends on the Rydberg constant and the Lamb shift [Mohr *et al.* 2016]. However, for S states, the Lamb shift includes the proton charge radius, which cannot be accurately calculated since it requires complicated QCD calculations. The proton charge radius must therefore be measured directly by electron scattering [A1 Collaboration 2010] or indirectly via spectroscopy [Beyer *et al.* 2017]. The latter method of course requires an already known value for the Rydberg constant in order to calculate the charge radius, it is this latter method performed with muonic hydrogen that lead to the proton radius puzzle, since it is believed that the value of the Rydberg constant is accurate, but the value of the proton radius is in question. However, it is possible that if a measurement of the Rydberg constant is to be performed in Ps, (where the corrections to the Lamb shift due to the proton charge radius are completely non-existent, unlike any other system) the resulting proton charge radius value calculated using such value may be in agreement with the muonic hydrogen experiments.

7.5 Conclusion

Throughout the course of this project a number of significant milestones in Ps spectroscopy have been achieved. Efficient optical excitation into selected Stark states

was achieved (section 5.1) and the lifetime of a range of n states was directly measured. The laser field polarization used in this excitation was linked to the relative spectral intensities of each Stark state (section 5.3). A rudimentary form of a Stark filter was realized (section 5.2) making use of controlled electric field ionization. Stark and Zeeman mixing in $n = 2$ Ps was characterized (section 4.1) making measurements that optimize the amount of magnetic quenching by increasing singlet-triplet mixing using electric fields, and using vertical or horizontal laser polarization lead to further experiments that allowed for the formation of pure ensembles of $2\,^3S_1$ states (section 4.2) with single photon excitation. The characterization of LYSO scintillators for use in SSPALS detection and single-event counting techniques allowed us to improve the rate at which we are able to perform measurements with significant signal to noise ratios (section 2.3.2). The first demonstration of Rydberg Ps manipulation was achieved in the form of guiding low-field-seeking states of Rydberg Ps in a straight quadrupole guide structure (section 6.2) which was modified to include a 45° bend which provided some velocity selection (section 6.3), and separated the Rydberg Ps path from the interaction region and the positron beam path.

This opens the door for a variety of different experiments to be performed after the curved guide such as scattering experiments to generate atom-positron bound states [Swann *et al.* 2016]. This work will enable a new generation of Rydberg atom-optics experiments including deceleration, focusing, and trapping which may be instrumental in making a gravity measurement with Ps Rydberg states [Mills & Leventhal 2002]. Additionally, it is possible that our experiments could inform high precision microwave spectroscopy between n states that could lead to a new spectroscopic measurement of the Rydberg constant without corrections due to the proton charge distribution, even for S states [Pohl *et al.* 2013]. If this value were to differ from the accepted CODATA standard by a relative fraction of $\sim 3.1 \times 10^{-11}$, it would contribute towards explaining the proton radius puzzle as a discrepancy in the Rydberg constant.

Bibliography

[A1 Collaboration 2010] A1 Collaboration. *High-Precision Determination of the Electric and Magnetic Form Factors of the Proton*. Phys. Rev. Lett., **105**, 242001 (2010). doi: 10.1103/PhysRevLett.105.242001.

[Adkins 1983] G. S. Adkins. *Radiative corrections to positronium decay*. Annals of Physics, **146**, 78 (1983). doi: 10.1016/0003-4916(83)90053-2.

[Aghion *et al.* 2016] S. Aghion *et al.* *Laser excitation of the $n = 3$ level of positronium for antihydrogen production*. Phys. Rev. A, **94**, 012507 (2016). doi: 10.1103/PhysRevA.94.012507.

[Alekseev 1958] A. I. Alekseev. *Two-Photon Annihilation of Positronium in the P-State*. Soviet Phys. JETP., **7**, 826 (1958).

[Alekseev 1959] A. I. Alekseev. *Three-Photon Annihilation of Positronium in the P-State*. Soviet Phys. JETP., **9**, 1312 (1959).

[Alonso *et al.* 2015] A. M. Alonso, B. S. Cooper, A. Deller, S. D. Hogan and D. B. Cassidy. *Controlling Positronium Annihilation with Electric Fields*. Phys. Rev. Lett., **115**, 183401 (2015). doi: 10.1103/PhysRevLett.115.183401.

[Alonso *et al.* 2016a] A. M. Alonso, B. S. Cooper, A. Deller and D. B. Cassidy. *Single-shot positron annihilation lifetime spectroscopy with LYSO scintillators*. NIM A, **828**, 163 (2016a). doi: http://dx.doi.org/10.1016/j.nima.2016.05.049.

[Alonso *et al.* 2016b] A. M. Alonso, B. S. Cooper, A. Deller, S. D. Hogan and D. B. Cassidy. *Positronium decay from $n = 2$ states in electric and magnetic fields*. Phys. Rev. A, **93**, 012506 (2016b). doi: 10.1103/PhysRevA.93.012506.

[Alonso *et al.* 2017a] A. M. Alonso, B. S. Cooper, A. Deller, L. Gurung, S. D. Hogan and D. B. Cassidy. *Velocity selection of Rydberg positronium using a curved electrostatic guide*. Phys. Rev. A, **95**, 053409 (2017a). doi: 10.1103/PhysRevA.95.053409.

[Alonso *et al.* 2017b] A. M. Alonso, S. D. Hogan and D. B. Cassidy. *Production of $2\,^3S_1$ positronium atoms by single-photon excitation in an electric field*. Phys. Rev. A, **95**, 033408 (2017b). doi: 10.1103/PhysRevA.95.033408.

[ALPHA Collaboration 2013] ALPHA Collaboration. *Description and first application of a new technique to measure the gravitational mass of antihydrogen*. Nature Communications, **4**, 1785 (2013). doi: 10.1038/ncomms2787.

[Andersen *et al.* 2015] S. L. Andersen, D. B. Cassidy, J. Chevallier, B. S. Cooper, A. Deller, T. E. Wall and U. I. Uggerhj. *Positronium emission and cooling in reflection and transmission from thin meso-structured silica films*. Journal of Physics B: Atomic, Molecular and Optical Physics, **48**, 204003 (2015). doi: 10.1088/0953-4075/48/20/204003.

[Anderson *et al.* 2014] E. K. Anderson, R. A. Boadle, J. R. Machacek, L. Chiari, C. Makochekanwa, S. J. Buckman, M. J. Brunger, G. Garcia, F. Blanco, O. Ingolfsson and J. P. Sullivan. *Low energy positron interactions with uracil-Total scattering, positronium formation, and differential elastic scattering cross sections*. The Journal of Chemical Physics, **141**, 034306 (2014). doi: 10.1063/1.4887072.

[Anderson 1933] C. D. Anderson. *The Positive Electron*. Phys. Rev., **43**, 491 (1933). doi: 10.1103/PhysRev.43.491.

[Barker & Charlton 2012] P. F. Barker and M. Charlton. *Directed fluxes of positronium using pulsed travelling optical lattices*. New Journal of Physics, **14**, 045005 (2012). doi: 10.1088/1367-2630/14/4/045005.

[Barker & Shneider 2001] P. F. Barker and M. N. Shneider. *Optical microlinear accelerator for molecules and atoms*. Phys. Rev. A, **64**, 033408 (2001). doi: 10.1103/PhysRevA.64.033408.

[Bennewitz *et al.* 1955] H. Bennewitz, W. Paul and C. Schlier. *Fokussierung polarer Molekle*. Zeitschrift fur Physik, **141**, 6 (1955). doi: 10.1007/BF01327279.

[Bertsche & Osterwalder 2010] B. Bertsche and A. Osterwalder. *State-selective detection of velocity-filtered ND_3 molecules*. Phys. Rev. A, **82**, 033418 (2010). doi: 10.1103/PhysRevA.82.033418.

[Bethe & Salpeter 1957] H. A. Bethe and E. E. Salpeter. Quantum Mechanics of One- and Two-Electron Atoms. Springer, Berlin (1957).

[Beyer *et al.* 2017] A. Beyer, L. Maisenbacher, A. Matveev, R. Pohl, K. Khabarova, A. Grinin, T. Lamour, D. C. Yost, T. W. Hänsch, N. Kolachevsky and T. Udem. *The Rydberg constant and proton size from atomic hydrogen*. Science, **358**, 79 (2017). doi: 10.1126/science.aah6677.

[Biedermann *et al.* 2015] G. W. Biedermann, X. Wu, L. Deslauriers, S. Roy, C. Mahadeswaraswamy and M. A. Kasevich. *Testing gravity with cold-atom interferometers*. Phys. Rev. A, **91**, 033629 (2015). doi: 10.1103/PhysRevA.91.033629.

[Breeden & Metcalf 1981] T. Breeden and H. Metcalf. *Stark Acceleration of Rydberg Atoms in Inhomogeneous Electric Fields*. Phys. Rev. Lett., **47**, 1726 (1981). doi: 10.1103/PhysRevLett.47.1726.

[Canter *et al.* 1972] K. F. Canter, P. G. Coleman, T. C. Griffith and G. R. Heyland. *Measurement of total cross sections for low energy positron-helium colli-*

sions. (Positron backscattering from metal surface). J. Phys. B, **5**, L167 (1972). doi: 10.1088/0022-3700/5/8/007.

[Canter *et al.* 1975] K. F. Canter, A. P. Mills, Jr. and S. Berko. *Observations of Positronium Lyman-α Radiation*. Phys. Rev. Lett., **34**, 177 (1975). doi: 10.1103/PhysRevLett.34.177.

[Cassidy & Hogan 2014] D. B. Cassidy and S. D. Hogan. *Atom control and gravity measurements using Rydberg positronium*. International Journal of Modern Physics: Conference Series, **30**, 1460259 (2014). doi: 10.1142/S2010194514602592.

[Cassidy & Mills 2007] D. B. Cassidy and A. P. Mills, Jr. *A fast detector for single-shot positron annihilation lifetime spectroscopy* . Nucl. Instrum. Meth. A, **580**, 1338 (2007). doi: 10.1016/j.nima.2007.06.078.

[Cassidy & Mills 2008] D. B. Cassidy and A. P. Mills. *Interactions Between Positronium Atoms in Porous Silica*. Phys. Rev. Lett., **100**, 013401 (2008). doi: 10.1103/PhysRevLett.100.013401.

[Cassidy & Mills 2011] D. B. Cassidy and A. P. Mills, Jr. *Enhanced Ps-Ps Interactions due to Quantum Confinement*. Phys. Rev. Lett., **107**, 213401 (2011). doi: 10.1103/PhysRevLett.107.213401.

[Cassidy *et al.* 2006a] D. B. Cassidy, S. H. M. Deng, R. G. Greaves and A. P. Mills, Jr. *Accumulator for the production of intense positron pulses*. Rev. Sci. Instrum., **77**, 073106 (2006a). doi: 10.1063/1.2221509.

[Cassidy *et al.* 2006b] D. B. Cassidy, S. H. M. Deng, H. K. M. Tanaka and A. P. Mills, Jr. *Single shot positron annihilation lifetime spectroscopy*. Appl. Phys. Lett., **88**, 194105 (2006b). doi: 10.1063/1.2203336.

[Cassidy *et al.* 2010a] D. B. Cassidy, P. Crivelli, T. H. Hisakado, L. Liszkay, V. E. Meligne, P. Perez, H. W. K. Tom and A. P. Mills, Jr. *Positronium cooling in*

porous silica measured via Doppler spectroscopy. Phys. Rev. A, **81**, 012715 (2010a). doi: 10.1103/PhysRevA.81.012715.

[Cassidy *et al.* 2010b] D. B. Cassidy, V. E. Meligne and A. P. Mills, Jr. *Production of a Fully Spin-Polarized Ensemble of Positronium Atoms*. Phys. Rev. Lett., **104**, 173401 (2010b). doi: 10.1103/PhysRevLett.104.173401.

[Cassidy *et al.* 2011a] D. Cassidy, T. Hisakado, H. Tom and A. P. Mills, Jr. *Positronium formation via excitonlike states on Si and Ge surfaces*. Phys. Rev. B, **84**, 195312 (2011a). doi: 10.1103/PhysRevB.84.195312.

[Cassidy *et al.* 2011b] D. B. Cassidy, M. W. J. Bromley, L. C. Cota, T. H. Hisakado, H. W. K. Tom and A. P. Mills, Jr. *Cavity Induced Shift and Narrowing of the Positronium Lyman-α Transition*. Phys. Rev. Lett., **106**, 023401 (2011b). doi: 10.1103/PhysRevLett.106.023401.

[Cassidy *et al.* 2012a] D. B. Cassidy, T. H. Hisakado, H. W. K. Tom and A. P. Mills, Jr. *Efficient Production of Rydberg Positronium*. Phys. Rev. Lett., **108**, 043401 (2012a). doi: 10.1103/PhysRevLett.108.043401.

[Cassidy *et al.* 2012b] D. B. Cassidy, T. H. Hisakado, H. W. K. Tom and A. P. Mills, Jr. *Optical Spectroscopy of Molecular Positronium*. Phys. Rev. Lett., **108**, 133402 (2012b). doi: 10.1103/PhysRevLett.108.133402.

[Cassidy *et al.* 2012c] D. B. Cassidy, T. H. Hisakado, H. W. K. Tom and A. P. Mills, Jr. *Positronium Hyperfine Interval Measured via Saturated Absorption Spectroscopy*. Phys. Rev. Lett., **109**, 073401 (2012c). doi: 10.1103/PhysRevLett.109.073401.

[Charlton *et al.* 1994] M. Charlton, J. Eades, D. Horvth, R. Hughes and C. Zimmermann. *Antihydrogen physics*. Physics Reports, **241**, 65 (1994). doi: https://doi.org/10.1016/0370-1573(94)90081-7.

[Cheng *et al.* 2011] X. Cheng, D. Babikov and D. M. Schrader. *Binding-energy predictions of positrons and atoms*. Phys. Rev. A, **83**, 032504 (2011). doi: 10.1103/PhysRevA.83.032504.

[Cherry 1958] W. Cherry. *PhD Thesis*. Princeton University (1958).

[Chu & Mills 1982] S. Chu and A. P. Mills, Jr. *Excitation of the Positronium* $1^3S_1 \rightarrow 2^3S_1$ *Two-Photon Transition*. Phys. Rev. Lett., **48**, 1333 (1982). doi: 10.1103/PhysRevLett.48.1333.

[Chu *et al.* 1984] S. Chu, A. P. Mills and J. L. Hall. *Measurement of the Positronium* $1^3S_1 - 2^3S_1$ *Interval by Doppler-Free Two-Photon Spectroscopy*. Phys. Rev. Lett., **52**, 1689 (1984). doi: 10.1103/PhysRevLett.52.1689.

[Cooke *et al.* 2000] D. W. Cooke, K. J. McClellan, B. L. Bennett, J. M. Roper, M. T. Whittaker, R. E. Muenchausen and R. C. Sze. *Crystal growth and optical characterization of cerium-doped* $Lu_{1.8}Y_{0.2}SiO_5$. Journal of Applied Physics, **88**, 7360 (2000). doi: 10.1063/1.1328775.

[Cooper *et al.* 2015] B. S. Cooper, A. M. Alonso, A. Deller, T. E. Wall and D. B. Cassidy. *A trap-based pulsed positron beam optimised for positronium laser spectroscopy*. Rev. Sci. Instrum., **86**, 103101 (2015). doi: 10.1063/1.4931690.

[Curry 1973] S. M. Curry. *Combined Zeeman and Motional Stark Effects in the First Excited State of Positronium*. Phys.Rev. A, **7**, 447 (1973). doi: 10.1103/PhysRevA.7.447.

[Damburg & Kolosov 1983] R. J. Damburg and V. V. Kolosov. *Theoretical studies of hydrogen Rydberg atoms in electric fields*. In R. F. Stebbings and F. B. Dunning, editors, Rydberg States of Atoms and Molecules, 31. Cambridge University Press, Cambridge (1983).

[Danielson *et al.* 2015] J. R. Danielson, D. H. E. Dubin, R. G. Greaves and C. M. Surko. *Plasma and trap-based techniques for science with positrons*. Rev. Mod. Phys., **87**, 247 (2015). doi: 10.1103/RevModPhys.87.247.

[Day *et al.* 2001] D. J. Day, M. Charlton and G. Laricchia. *On the formation of excited state positronium in vacuum by positron impact on untreated surfaces*. Journal of Physics B: Atomic, Molecular and Optical Physics, **34**, 3617 (2001).

[de Beauvoir *et al.* 1997] B. de Beauvoir, F. Nez, L. Julien, B. Cagnac, F. Biraben, D. Touahri, L. Hilico, O. Acef, A. Clairon and J. J. Zondy. *Absolute Frequency Measurement of the* $2S-8S/D$ *Transitions in Hydrogen and Deuterium: New Determination of the Rydberg Constant*. Phys. Rev. Lett., **78**, 440 (1997). doi: 10.1103/PhysRevLett.78.440.

[Deller *et al.* 2014] A. Deller, T. Mortensen, C. A. Isaac, D. P. van der Werf and M. Charlton. *Radially selective inward transport of positrons in a Penning-Malmberg trap*. New Journal of Physics, **16**, 073028 (2014).

[Deller *et al.* 2015] A. Deller, B. S. Cooper, T. E. Wall and D. B. Cassidy. *Positronium emission from mesoporous silica studied by laser-enhanced time-of-flight spectroscopy*. New Journal of Physics, **17**, 043059 (2015). doi: 10.1088/1367-2630/17/4/043059.

[Deller *et al.* 2016a] A. Deller, A. M. Alonso, B. S. Cooper, S. D. Hogan and D. B. Cassidy. *Electrostatically Guided Rydberg Positronium*. Phys. Rev. Lett., **117**, 073202 (2016a). doi: 10.1103/PhysRevLett.117.073202.

[Deller *et al.* 2016b] A. Deller, A. M. Alonso, B. S. Cooper, S. D. Hogan and D. B. Cassidy. *Measurement of Rydberg positronium fluorescence lifetimes*. Phys. Rev. A, **93**, 062513 (2016b). doi: 10.1103/PhysRevA.93.062513.

[Demtröder 2003] W. Demtröder. Laser spectroscopy. Springer, New York, third édition (2003).

[Dermer & Weisheit 1989] C. D. Dermer and J. C. Weisheit. *Perturbative analysis of simultaneous Stark and Zeeman effects on $n = 1 \leftrightarrows n = 2$ radiative transitions in positronium*. Phys. Rev. A, **40**, 5526 (1989). doi: 10.1103/PhysRevA.40.5526.

[Deutsch & Brown 1952] M. Deutsch and S. C. Brown. *Zeeman Effect and Hyperfine Splitting of Positronium*. Phys. Rev., **85**, 1047 (1952). doi: 10.1103/PhysRev.85.1047.

[Deutsch 1951a] M. Deutsch. *Evidence for the Formation of Positronium in Gases*. Phys. Rev., **82**, 455 (1951a). doi: 10.1103/PhysRev.82.455.

[Deutsch 1951b] M. Deutsch. *Three-Quantum Decay of Positronium*. Phys. Rev., **83**, 866 (1951b). doi: 10.1103/PhysRev.83.866.

[DeVries 2010] J. E. DeVries, P. L. and Hasbun. A First Course in Computational Physics. Jones and Bartlett Learning (2010).

[Dirac 1927] P. A. M. Dirac. *The Quantum Theory of the Emission and Absorption of Radiation*. Proceedings of the Royal Society of London A: Mathematical, Physical and Engineering Sciences, **114**, 243 (1927). doi: 10.1098/rspa.1927.0039.

[Dirac 1928a] P. A. M. Dirac. *The Quantum Theory of the Electron*. Proceedings of the Royal Society of London A: Mathematical, Physical and Engineering Sciences, **117**, 610 (1928a). doi: 10.1098/rspa.1928.0023.

[Dirac 1928b] P. A. M. Dirac. *The Quantum Theory of the Electron. Part II*. Proceedings of the Royal Society of London A: Mathematical, Physical and Engineering Sciences, **118**, 351 (1928b). doi: 10.1098/rspa.1928.0056.

[Dirac 1930] P. A. M. Dirac. *On the Annihilation of Electrons and Protons*. Mathematical Proceedings of the Cambridge Philosophical Society, **26**, 361 (1930). doi: 10.1017/S0305004100016091.

[Dirac 1931] P. A. M. Dirac. *Quantised Singularities in the Electromagnetic Field*. Proceedings of the Royal Society of London A: Mathematical, Physical and Engineering Sciences, **133**, 60 (1931). doi: 10.1098/rspa.1931.0130.

[Fee *et al.* 1991] M. S. Fee, A. P. Mills, Jr., E. D. Shaw, R. J. Chichester, D. M. Zuckerman, S. Chu and K. Danzmann. *Sensitive detection of Doppler-free two-photon-excited 2 S positronium by spatially separated photoionization*. Phys. Rev. A, **44**, R5 (1991). doi: 10.1103/PhysRevA.44.R5.

[Fee *et al.* 1993] M. S. Fee, A. P. Mills, Jr., S. Chu, E. D. Shaw, K. Danzmann, R. J. Chichester and D. M. Zuckerman. *Measurement of the positronium* 1^3S_1-2^3S_1 *interval by continuous-wave two-photon excitation*. Phys. Rev. Lett., **70**, 1397 (1993). doi: 10.1103/PhysRevLett.70.1397.

[Ferrell 1951] R. A. Ferrell. *The Positronium Fine Structure*. Phys. Rev., **84**, 858 (1951). doi: 10.1103/PhysRev.84.858.

[Foot 2005] C. Foot. Atomic physics, Oxford master series in physics. Oxford University Press (2005).

[Fulton *et al.* 2006] R. Fulton, A. I. Bishop, M. N. Shneider and P. F. Barker. *Controlling the motion of cold molecules with deep periodic optical potentials*. Nature Physics, **2**, 465 (2006). doi: 10.1038/nphys339.

[Gallagher 1994] T. F. Gallagher. Rydberg Atoms. Cambridge University Press (1994). Cambridge Books Online.

[Goldman & Nieto 1982] T. Goldman and M. M. Nieto. *Experiments to measure the gravitational acceleration of antimatter*. Physics Letters B, **112**, 437 (1982). doi: https://doi.org/10.1016/0370-2693(82)90843-7.

[Gordon & Osterwalder 2017] S. D. S. Gordon and A. Osterwalder. *3D-Printed Beam Splitter for Polar Neutral Molecules*. Phys. Rev. Applied, **7**, 044022 (2017). doi: 10.1103/PhysRevApplied.7.044022.

[Greaves & Moxom 2003] R. G. Greaves and J. Moxom. *Design and Performance of a TrapBased Positron Beam Source*. AIP Conference Proceedings, **692**, 140 (2003). doi: 10.1063/1.1635169.

[Greaves & Moxom 2008] R. G. Greaves and J. M. Moxom. *Compression of trapped positrons in a single particle regime by a rotating electric field*. Phys. Plasmas, **15**, 072304 (2008). doi: 10.1063/1.2956335.

[Greenbank & Argent 1965] J. C. Greenbank and B. B. Argent. *Vapour pressure of magnesium, zinc and cadmium*. Trans. Faraday Soc., **61**, 655 (1965). doi: 10.1039/TF9656100655.

[Griffiths 2012] D. J. Griffiths. Introduction to Electrodynamics. Addison-Wesley (2012).

[Haas *et al.* 2006] M. Haas, U. D. Jentschura, C. H. Keitel, N. Kolachevsky, M. Herrmann, P. Fendel, M. Fischer, T. Udem, R. Holzwarth, T. W. Hänsch, M. O. Scully and G. S. Agarwal. *Two-photon excitation dynamics in bound two-body Coulomb systems including ac Stark shift and ionization*. Phys. Rev. A, **73**, 052501 (2006). doi: 10.1103/PhysRevA.73.052501.

[Hänsch *et al.* 1971] T. W. Hänsch, M. D. Levenson and A. L. Schawlow. *Complete Hyperfine Structure of a Molecular Iodine Line*. Phys. Rev. Lett., **26**, 946 (1971). doi: 10.1103/PhysRevLett.26.946.

[Harabati *et al.* 2014] C. Harabati, V. A. Dzuba and V. V. Flambaum. *Identification of atoms that can bind positrons*. Phys. Rev. A, **89**, 022517 (2014). doi: 10.1103/PhysRevA.89.022517.

[Hauri *et al.* 2010] C. P. Hauri, R. Ganter, F. Le Pimpec, A. Trisorio, C. Ruchert and H. H. Braun. *Intrinsic Emittance Reduction of an Electron Beam from Metal Photocathodes*. Phys. Rev. Lett., **104**, 234802 (2010). doi: 10.1103/PhysRevLett.104.234802.

[Hellwig *et al.* 1970] H. Hellwig, R. F. C. Vessot, M. W. Levine, P. W. Zitzewitz, D. W. Allan and D. J. Glaze. *Measurement of the Unperturbed Hydrogen Hyperfine Transition Frequency*. IEEE Transactions on Instrumentation and Measurement, **19**, 200 (1970). doi: 10.1109/TIM.1970.4313902.

[Hill 2001] R. J. Hill. *New Value of m_μ/m_e from Muonium Hyperfine Splitting*. Phys. Rev. Lett., **86**, 3280 (2001). doi: 10.1103/PhysRevLett.86.3280.

[Hogan & Merkt 2008] S. D. Hogan and F. Merkt. *Demonstration of Three-Dimensional Electrostatic Trapping of State-Selected Rydberg Atoms*. Phys. Rev. Lett., **100**, 043001 (2008). doi: 10.1103/PhysRevLett.100.043001.

[Hogan *et al.* 2009] S. D. Hogan, C. Seiler and F. Merkt. *Rydberg-State-Enabled Deceleration and Trapping of Cold Molecules*. Phys. Rev. Lett., **103**, 123001 (2009). doi: 10.1103/PhysRevLett.103.123001.

[Hogan *et al.* 2012] S. D. Hogan, P. Allmendinger, H. Saßmannshausen, H. Schmutz and F. Merkt. *Surface-Electrode Rydberg-Stark Decelerator*. Phys. Rev. Lett., **108**, 063008 (2012). doi: 10.1103/PhysRevLett.108.063008.

[Hogan *et al.* 2013] S. D. Hogan, C. Seiler and F. Merkt. *Motional, isotope and quadratic Stark effects in RydbergStark deceleration and electric trapping of H and D*. Journal of Physics B: Atomic, Molecular and Optical Physics, **46**, 045303 (2013).

[Hogan 2013] S. D. Hogan. *Calculated photoexcitation spectra of positronium Rydberg states*. Phys. Rev. A, **87**, 063423 (2013). doi: 10.1103/PhysRevA.87.063423.

[Hogan 2016] S. D. Hogan. *Rydberg-Stark deceleration of atoms and molecules*. EPJ Techniques and Instrumentation, **3**, 1 (2016). doi: 10.1140/epjti/s40485-015-0028-4.

[Hotop & Niehaus 1968] H. Hotop and A. Niehaus. *Reactions of excited atoms and molecules with atoms and molecules*. Zeitschrift für Physik, **215**, 395 (1968). doi: 10.1007/BF01380020.

[Howell *et al.* 1982] R. H. Howell, R. A. Alvarez and M. Stanek. *Production of slow positrons with a 100-MeV electron linac*. Applied Physics Letters, **40**, 751 (1982). doi: http://dx.doi.org/10.1063/1.93215.

[Howell *et al.* 1985] P. Howell, M. Fluss, I. Rosenberg and P. Meyer. *Low-energy, high-intensity positron beam experiments with a linac*. Nuclear Instruments and Methods in Physics Research Section B: Beam Interactions with Materials and Atoms, **10**, 373 (1985). doi: http://dx.doi.org/10.1016/0168-583X(85)90272-1.

[Isaac *et al.* 2011] C. A. Isaac, C. J. Baker, T. Mortensen, D. P. van der Werf and M. Charlton. *Compression of Positron Clouds in the Independent Particle Regime*. Phys. Rev. Lett., **107**, 033201 (2011). doi: 10.1103/PhysRevLett.107.033201.

[Ishida *et al.* 2014] A. Ishida, T. Namba, S. Asai, T. Kobayashi, H. Saito, M. Yoshida, K. Tanaka and A. Yamamoto. *New precision measurement of hyperfine splitting of positronium*. Physics Letters B, **734**, 338 (2014). doi: 10.1016/j.physletb.2014.05.083.

[Jones *et al.* 2014] A. C. L. Jones, T. H. Hisakado, H. J. Goldman, H. W. K. Tom, A. P. Mills, Jr. and D. B. Cassidy. *Doppler-corrected Balmer spectroscopy of Rydberg positronium*. Phys. Rev. A, **90**, 012503 (2014). doi: 10.1103/PhysRevA.90.012503.

[Jones *et al.* 2016] A. Jones, A. Piñeiro, E. Roeder, H. Rutbeck-Goldman, H. Tom and A. P. Mills, Jr. *Large-area field-ionization detector for the study of Rydberg atoms*. Review of Scientific Instruments, **87**, 113307 (2016).

[Jones *et al.* 2017] A. C. L. Jones, J. Moxom, H. J. Rutbeck-Goldman, K. A. Osorno, G. G. Cecchini, M. Fuentes-Garcia, R. G. Greaves, D. J. Adams,

H. W. K. Tom, A. P. Mills and M. Leventhal. *Focusing of a Rydberg Positronium Beam with an Ellipsoidal Electrostatic Mirror*. Phys. Rev. Lett., **119**, 053201 (2017). doi: 10.1103/PhysRevLett.119.053201.

[Kasevich & Chu 1991] M. Kasevich and S. Chu. *Atomic interferometry using stimulated Raman transitions*. Phys. Rev. Lett., **67**, 181 (1991). doi: 10.1103/PhysRevLett.67.181.

[Khatri *et al.* 1990] R. Khatri, M. Charlton, P. Sferlazzo, K. G. Lynn, A. P. M. Jr. and L. O. Roellig. *Improvement of raregas solid moderators by using conical geometry*. Applied Physics Letters, **57**, 2374 (1990). doi: 10.1063/1.103856.

[Kniehl & Penin 2000] B. A. Kniehl and A. A. Penin. *Order* $\alpha^7 \ln(1/\alpha)$ *Contribution to Positronium Hyperfine Splitting*. Phys. Rev. Lett., **85**, 5094 (2000). doi: 10.1103/PhysRevLett.85.5094.

[Lancuba & Hogan 2014] P. Lancuba and S. D. Hogan. *Transmission-line decelerators for atoms in high Rydberg states*. Phys. Rev. A, **90**, 053420 (2014). doi: 10.1103/PhysRevA.90.053420.

[Lancuba & Hogan 2016] P. Lancuba and S. D. Hogan. *Electrostatic trapping and in situ detection of Rydberg atoms above chip-based transmission lines*. Journal of Physics B: Atomic, Molecular and Optical Physics, **49**, 074006 (2016).

[Laricchia *et al.* 1985] G. Laricchia, M. Charlton, G. Clark and T. Griffith. *Excited state positronium formation in low density gases*. Physics Letters A, **109**, 97 (1985). doi: http://dx.doi.org/10.1016/0375-9601(85)90264-6.

[Liszkay *et al.* 2008] L. Liszkay, C. Corbel, P. Perez, P. Desgardin, M. F. Barthe, T. Ohdaira, R. Suzuki, P. Crivelli, U. Gendotti, A. Rubbia, M. Etienne and A. Walcarius. *Positronium reemission yield from mesostructured silica films*. Appl. Phys. Lett., **92**, 063114 (2008). doi: 10.1063/1.2844888.

[Maiman 1960] T. H. Maiman. *Stimulated Optical Radiation in Ruby*. Nature, **187**, 493 (1960). doi: 10.1038/187493a0.

[Marjanovi *et al.* 2016] S. Marjanovi, A. Bankovi, D. Cassidy, B. Cooper, A. Deller, S. Dujko and Z. L. Petrovi. *A CF 4 based positron trap*. Journal of Physics B: Atomic, Molecular and Optical Physics, **49**, 215001 (2016). doi: 10.1088/0953-4075/49/21/215001.

[Melnikov & Yelkhovsky 2001] K. Melnikov and A. Yelkhovsky. $O(\alpha^3 \ln\alpha)$. Phys. Rev. Lett., **86**, 1498 (2001). doi: 10.1103/PhysRevLett.86.1498.

[Merkt & Zare 1994] F. Merkt and R. N. Zare. *On the lifetimes of Rydberg states probed by delayed pulsed field ionization*. The Journal of Chemical Physics, **101**, 3495 (1994).

[Mills & Gullikson 1986] A. P. Mills, Jr. and E. M. Gullikson. *Solid neon moderator for producing slow positrons*. Appl. Phys. Lett., **49**, 1121 (1986). doi: 10.1063/1.97441.

[Mills & Leventhal 2002] A. P. Mills, Jr. and M. Leventhal. *Can we measure the gravitational free fall of cold Rydberg state positronium?* Nuclear Instruments and Methods in Physics Research Section B: Beam Interactions with Materials and Atoms, **192**, 102 (2002). doi: 10.1016/S0168-583X(02)00789-9.

[Mills 1979] A. P. Mills, Jr. *Thermal activation measurement of positron binding energies at surfaces*. Solid State Communications, **31**, 623 (1979). doi: http://dx.doi.org/10.1016/0038-1098(79)90310-7.

[Mills 1980a] A. P. Mills, Jr. *Brightness enhancement of slow positron beams*. Applied physics, **23**, 189 (1980a). doi: 10.1007/BF00899716.

[Mills 1980b] A. P. Mills, Jr. *Time bunching of slow positrons for annihilation lifetime and pulsed laser photon absorption experiments*. Appl. Phys., **22**, 273 (1980b). doi: 10.1007/BF00899876.

[Mitroy *et al.* 2002] J. Mitroy, M. W. J. Bromley and G. G. Ryzhikh. *Positron and positronium binding to atoms*. Journal of Physics B: Atomic, Molecular and Optical Physics, **35**, R81 (2002).

[Mohorovičić 1934] S. Mohorovičić. *Möglichkeit neuer Elemente und ihre Bedeutung für die Astrophysik*. Astronomische Nachrichten, **253**, 93 (1934). doi: 10.1002/asna.19342530402.

[Mohr *et al.* 2016] P. J. Mohr, D. B. Newell and B. N. Taylor. *CODATA recommended values of the fundamental physical constants: 2014*. Rev. Mod. Phys., **88**, 035009 (2016). doi: 10.1103/RevModPhys.88.035009.

[Motsch *et al.* 2009] M. Motsch, L. D. van Buuren, C. Sommer, M. Zeppenfeld, G. Rempe and P. W. H. Pinkse. *Cold guided beams of water isotopologs*. Phys. Rev. A, **79**, 013405 (2009). doi: 10.1103/PhysRevA.79.013405.

[Murphy & Surko 1992] T. J. Murphy and C. M. Surko. *Positron trapping in an electrostatic well by inelastic collisions with nitrogen molecules*. Phys. Rev. A, **46**, 5696 (1992). doi: 10.1103/PhysRevA.46.5696.

[Natisin *et al.* 2014] M. R. Natisin, J. R. Danielson and C. M. Surko. *Positron cooling by vibrational and rotational excitation of molecular gases*. Journal of Physics B: Atomic, Molecular and Optical Physics, **47**, 225209 (2014).

[Oberthaler 2002] M. Oberthaler. *Anti-matter wave interferometry with positronium*. Nuclear Instruments and Methods in Physics Research Section B: Beam Interactions with Materials and Atoms, **192**, 129 (2002). doi: http://dx.doi.org/10.1016/S0168-583X(02)00793-0.

[Ore & Powell 1949] A. Ore and J. L. Powell. *Three-Photon Annihilation of an Electron-Positron Pair*. Phys. Rev., **75**, 1696 (1949). doi: 10.1103/PhysRev.75.1696.

[Osterwalder 2015] A. Osterwalder. *Merged neutral beams*. EPJ Techniques and Instrumentation, **2**, 10 (2015). doi: 10.1140/epjti/s40485-015-0022-x.

[Overton & Coleman 1997] N. Overton and P. Coleman. *Measurement of the Energy Spectrum of Secondary Electrons Ejected from Solids by Positron Impact*. Phys. Rev. Lett., **79**, 305 (1997). doi: 10.1103/PhysRevLett.79.305.

[Parthey *et al.* 2011] C. G. Parthey, A. Matveev, J. Alnis, B. Bernhardt, A. Beyer, R. Holzwarth, A. Maistrou, R. Pohl, K. Predehl, T. Udem, T. Wilken, N. Kolachevsky, M. Abgrall, D. Rovera, C. Salomon, P. Laurent and T. W. Hänsch. *Improved Measurement of the Hydrogen* $1S-2S$ *Transition Frequency*. Phys. Rev. Lett., **107**, 203001 (2011). doi: 10.1103/PhysRevLett.107.203001.

[Pirenne 1944] J. Pirenne. *PhD thesis*. University of Paris (1944).

[Pohl *et al.* 2010] R. Pohl *et al.* *The size of the proton*. Nature, **466**, 213 (2010). doi: 10.1038/nature09250.

[Pohl *et al.* 2013] R. Pohl, R. Gilman, G. A. Miller and K. Pachucki. *Muonic Hydrogen and the Proton Radius Puzzle*. Annual Review of Nuclear and Particle Science, **63**, 175 (2013). doi: 10.1146/annurev-nucl-102212-170627.

[Rangwala *et al.* 2003] S. A. Rangwala, T. Junglen, T. Rieger, P. W. H. Pinkse and G. Rempe. *Continuous source of translationally cold dipolar molecules*. Phys. Rev. A, **67**, 043406 (2003). doi: 10.1103/PhysRevA.67.043406.

[Rich 1981] A. Rich. *Recent experimental advances in positronium research*. Rev. Mod. Phys., **53**, 127 (1981). doi: 10.1103/RevModPhys.53.127.

[Ruark 1945] A. E. Ruark. *Positronium*. Phys. Rev., **68**, 278 (1945). doi: 10.1103/PhysRev.68.278.

[Sala *et al.* 2015] S. Sala, F. Castelli, M. Giammarchi, S. Siccardi and S. Olivares. *Matter-wave interferometry: towards antimatter interferometers*. Journal of Physics B: Atomic, Molecular and Optical Physics, **48**, 195002 (2015).

[Schoepf *et al.* 1992] D. C. Schoepf, S. Berko, K. F. Canter and P. Sferlazzo. *Observation of Ps($n = 2$) from well-characterized metal surfaces in ultrahigh vacuum*. Phys. Rev. A, **45**, 1407 (1992). doi: 10.1103/PhysRevA.45.1407.

[Schultz & Lynn 1988] P. J. Schultz and K. G. Lynn. *Interaction of positron beams with surfaces, thin films, and interfaces*. Rev. Mod. Phys., **60**, 701 (1988). doi: 10.1103/RevModPhys.60.701.

[Schwob *et al.* 1999] C. Schwob, L. Jozefowski, B. de Beauvoir, L. Hilico, F. Nez, L. Julien, F. Biraben, O. Acef, J.-J. Zondy and A. Clairon. *Optical Frequency Measurement of the $2S-12D$ Transitions in Hydrogen and Deuterium: Rydberg Constant and Lamb Shift Determinations*. Phys. Rev. Lett., **82**, 4960 (1999). doi: 10.1103/PhysRevLett.82.4960.

[Seiler *et al.* 2011a] C. Seiler, S. D. Hogan and F. Merkt. *Trapping cold molecular hydrogen*. Phys. Chem. Chem. Phys., **13**, 19000 (2011a). doi: 10.1039/C1CP21276A.

[Seiler *et al.* 2011b] C. Seiler, S. D. Hogan, H. Schmutz, J. A. Agner and F. Merkt. *Collisional and Radiative Processes in Adiabatic Deceleration, Deflection, and Off-Axis Trapping of a Rydberg Atom Beam*. Phys. Rev. Lett., **106**, 073003 (2011b). doi: 10.1103/PhysRevLett.106.073003.

[Seiler *et al.* 2012] C. Seiler, S. D. Hogan and F. Merkt. *Dynamical Processes in Rydberg-Stark Deceleration and Trapping of Atoms and Molecules*. CHIMIA International Journal for Chemistry, **66**, 208 (2012). doi: doi:10.2533/chimia.2012.208.

[Shapiro & Breit 1959] J. Shapiro and G. Breit. *Metastability of 2s States of Hydrogenic Atoms*. Phys. Rev., **113**, 179 (1959). doi: 10.1103/PhysRev.113.179.

[Sommer *et al.* 2010] C. Sommer, M. Motsch, S. Chervenkov, L. D. van Buuren, M. Zeppenfeld, P. W. H. Pinkse and G. Rempe. *Velocity-selected molecular pulses produced by an electric guide*. Phys. Rev. A, **82**, 013410 (2010). doi: 10.1103/PhysRevA.82.013410.

[Steiger & Conti 1992] T. D. Steiger and R. S. Conti. *Formation of $n = 2$ positronium from untreated metal surfaces*. Phys. Rev. A, **45**, 2744 (1992). doi: 10.1103/PhysRevA.45.2744.

[Surko *et al.* 1989] C. M. Surko, M. Leventhal and A. Passner. *Positron Plasma in the Laboratory*. Phys. Rev. Lett., **62**, 901 (1989). doi: 10.1103/PhysRevLett.62.901.

[Swann *et al.* 2016] A. R. Swann, D. B. Cassidy, A. Deller and G. F. Gribakin. *Formation of positron-atom bound states in collisions between Rydberg Ps and neutral atoms*. Phys. Rev. A, **93**, 052712 (2016). doi: 10.1103/PhysRevA.93.052712.

[Townsend *et al.* 2001] D. Townsend, A. L. Goodgame, S. R. Procter, S. R. Mackenzie and T. P. Softley. *Deflection of krypton Rydberg atoms in the field of an electric dipole*. Journal of Physics B: Atomic, Molecular and Optical Physics, **34**, 439 (2001).

[van Buuren *et al.* 2009] L. D. van Buuren, C. Sommer, M. Motsch, S. Pohle, M. Schenk, J. Bayerl, P. W. H. Pinkse and G. Rempe. *Electrostatic Extraction of Cold Molecules from a Cryogenic Reservoir*. Phys. Rev. Lett., **102**, 033001 (2009). doi: 10.1103/PhysRevLett.102.033001.

[van de Meerakker *et al.* 2012] S. Y. T. van de Meerakker, H. L. Bethlem, N. Vanhaecke and G. Meijer. *Manipulation and Control of Molecular Beams*. Chemical Reviews, **112**, 4828 (2012). doi: 10.1021/cr200349r. PMID: 22449067.

[Vliegen *et al.* 2007] E. Vliegen, S. D. Hogan, H. Schmutz and F. Merkt. *Stark deceleration and trapping of hydrogen Rydberg atoms*. Phys. Rev. A, **76**, 023405 (2007). doi: 10.1103/PhysRevA.76.023405.

[Voigtlnder *et al.* 2008] B. Voigtlnder, V. Cherepanov, C. Elsaesser and U. Linke. *Metal bead crystals for easy heating by direct current*. Review of scientific instruments, **79**, 033911 (2008).

[Wall *et al.* 2014] T. E. Wall, D. B. Cassidy and S. D. Hogan. *Single-color two-photon spectroscopy of Rydberg states in electric fields*. Phys. Rev. A, **90**, 053430 (2014). doi: 10.1103/PhysRevA.90.053430.

[Wall *et al.* 2015] T. E. Wall, A. M. Alonso, B. S. Cooper, A. Deller, S. D. Hogan and D. B. Cassidy. *Selective Production of Rydberg-Stark States of Positronium*. Phys. Rev. Lett., **114**, 173001 (2015). doi: 10.1103/PhysRevLett.114.173001.

[Wallyn *et al.* 1996] P. Wallyn, W. A. Mahoney, P. Durouchoux and C. Chapuis. *The Positronium Radiative Combination Spectrum: Calculation in the Limit of Thermal Positrons and Low Densities*. Astrophysical Journal, **465**, 473 (1996). doi: 10.1086/177434.

[Wheeler 1946] J. A. Wheeler. *Polyelectrons*. Annals of the New York Academy of Sciences, **48**, 219 (1946). doi: 10.1111/j.1749-6632.1946.tb31764.x.

[Wing 1980] W. H. Wing. *Electrostatic Trapping of Neutral Atomic Particles*. Phys. Rev. Lett., **45**, 631 (1980). doi: 10.1103/PhysRevLett.45.631.

[Wolfenstein & Ravenhall 1952] L. Wolfenstein and D. G. Ravenhall. *Some Consequences of Invariance under Charge Conjugation*. Phys. Rev., **88**, 279 (1952). doi: 10.1103/PhysRev.88.279.

[Zhan *et al.* 2011] X. Zhan *et al.* *High-precision measurement of the proton elastic form factor ratio pGE/GM at low Q2*. Physics Letters B, **705**, 59 (2011). doi: https://doi.org/10.1016/j.physletb.2011.10.002.

[Ziock *et al.* 1990a] K. P. Ziock, C. D. Dermer, R. H. Howell, F. Magnotta and K. M. Jones. *Optical saturation of the* 1^3S-2^3P *transition in positronium*. J. Phys. B, **23**, 329 (1990a). doi: 10.1088/0953-4075/23/2/015.

[Ziock *et al.* 1990b] K. P. Ziock, R. H. Howell, F. Magnotta, R. A. Failor and K. M. Jones. *First observation of resonant excitation of high- n states*

in positronium. Phys. Rev. Lett., **64**, 2366 (1990b). doi: 10.1103/PhysRevLett.64.2366.